



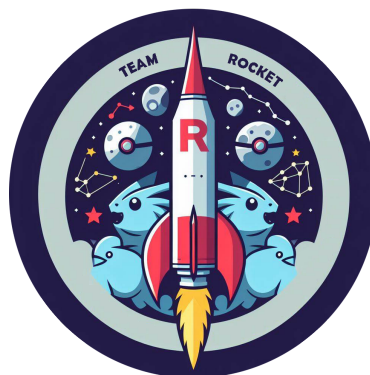
**POLITECNICO**  
**MILANO 1863**

**SCUOLA DI INGEGNERIA INDUSTRIALE  
E DELL'INFORMAZIONE**

## LAUNCH SYSTEMS

**Professors:** Filippo Maggi & Stefania Carlotti  
Academic year 2024-2025

**JEENO**  
Jet Enabled Efficient Navigational Orbiter



Authors: Team Rocket		
Person Code	Surname	Name
10726940	Bachini	Pier Francesco A.
10721571	Belletti	Stefano
10764327	Bolsi	Pietro
10743222	Coacci	Filippo
10694949	De Luca	Leo
10753159	De Marco	Elena
10699437	Sciutto	Giacomo
10770519	Tebaldi	Alessandro
10698865	Vilhelem	Jeno

**Submission date:** Wednesday 11<sup>th</sup> December, 2024

## **Abstract**

This report aims to present a conceptual study of a novel reusable airborne launch system, designed to inject a payload into a retrograde sun-synchronous orbit. The system consists of a two stage to orbit vehicle, capable of being carried by a civil aircraft and launched mid-air.

At first, the client requirements are identified and categorized. Subsequently, the House of Quality is developed to characterize the main parameters of the system and to asses the main competitors in this field. Then, the models implemented for the conceptual design of the different subsystem composing the launch vehicle are presented and validated. Lastly, the trajectory is propagated with an uncertainty analysis affecting various parameters, with a particular focus on how these uncertainties impact orbit insertion.

Finally, from the analysis of the results, critical observations are made about future iterations, cost analysis and the mission overall feasibility.

# Contents

<b>List of Figures</b>	<b>iv</b>
<b>List of Tables</b>	<b>v</b>
<b>1 Conceptual Analysis</b>	<b>1</b>
1.1 Requirements . . . . .	1
1.1.1 Mission level Requirements . . . . .	1
1.1.2 System level Requirements . . . . .	1
1.1.3 Item level Requirements . . . . .	2
1.1.4 House of Quality . . . . .	2
1.1.4.1 Relevance of quality characteristics . . . . .	2
1.1.4.2 Competitors Analysis . . . . .	3
1.1.4.3 Baseline . . . . .	3
1.1.5 Aircraft Platform . . . . .	4
1.1.6 Mission Budget Estimation . . . . .	4
1.1.7 Functional Analysis . . . . .	5
<b>2 Development</b>	<b>5</b>
2.1 Mass and Structures . . . . .	6
2.1.1 Iterative Method for Optimal Staging . . . . .	6
2.1.2 Factor of Safety . . . . .	6
2.1.3 Inert Masses Estimation . . . . .	6
2.1.4 Loads Analysis . . . . .	7
2.1.4.1 Failure Modes . . . . .	8
2.1.4.2 Definitions of Load Parameters . . . . .	8
2.1.5 Materials Selection . . . . .	9
2.1.6 Attached Configuration . . . . .	10
2.2 Propulsion system and Thermal Analysis . . . . .	11
2.2.1 Introduction . . . . .	11
2.2.2 Architecture choice . . . . .	11
2.2.3 Chemical couple choice . . . . .	11
2.2.4 Engine choice . . . . .	12
2.2.5 Nozzle modification . . . . .	13
2.2.5.1 Thermal model . . . . .	14
2.3 Aerodynamics . . . . .	15
2.3.1 Aerodynamic Model . . . . .	15
2.3.2 Panel Method Algorithm for Aerodynamic Analysis . . . . .	16
2.3.3 Stability analysis . . . . .	17
2.3.3.1 Fins Geometry . . . . .	18
2.4 Mission Analysis . . . . .	18
2.4.1 Phases of the mission . . . . .	18
2.4.2 Simulator . . . . .	19
2.4.2.1 Controlled parameters . . . . .	19
2.4.2.2 Equations of motion . . . . .	19
2.4.2.3 Dynamic properties . . . . .	20
2.4.2.4 Navigation . . . . .	20
2.4.2.5 Optimization . . . . .	20
2.4.3 Launch position . . . . .	20

2.4.4	Monte Carlo Analysis . . . . .	20
2.5	Recovery system and re-entry analysis . . . . .	21
2.5.1	Recovery system architecture . . . . .	21
2.5.1.1	Ballute design . . . . .	21
2.5.1.2	Main parachute design . . . . .	22
2.5.2	Opening Shocks model . . . . .	22
2.5.3	Heat-flux model . . . . .	23
2.5.4	Ocean Recovery and Location . . . . .	23
<b>3</b>	<b>Results and Conclusions</b>	<b>24</b>
3.1	Development results . . . . .	24
3.1.1	Trajectory results . . . . .	25
3.1.1.1	Recoverability assessment . . . . .	28
3.1.2	Analysis with 400 kg payload . . . . .	28
3.2	Feasibility of Launch Condition . . . . .	28
3.3	Cost Analysis . . . . .	29
3.4	Further Developments . . . . .	30
3.5	Conclusions . . . . .	30
<b>Appendices</b>		<b>i</b>
A.1	House of Quality . . . . .	i
B.1	Baseline Data Interpolation . . . . .	ii
B.2	Optimal Staging . . . . .	iii
B.3	Inert Mass Estimation Formulas . . . . .	iv
B.4	Yielding Resistance . . . . .	iv
B.5	Buckling Analysis . . . . .	vi
B.5.1	Pressurized vessels: $\Delta p > 0$ . . . . .	vi
B.5.2	Unpressurized vessels: $\Delta p = 0$ . . . . .	viii
B.5.3	Combined loads . . . . .	ix
B.6	Admissible Bending Moments . . . . .	x
C.1	The Pflanz Method for Calculating Parachute Opening Forces . . . . .	x
C.1.1	Ballistic Parameter and Force-Reduction Factor . . . . .	xi
D.1	Aerodynamic Models . . . . .	xii
E.1	Thermodynamical model for boiloff analysis . . . . .	xviii
E.1.1	Ellipsoidal domes and Insulation mass and thickness . . . . .	xviii
E.1.2	Thermal resistances model . . . . .	xviii
E.1.2.1	LOX-Tank Convection . . . . .	xviii
E.1.2.2	Insulation-Air Convection . . . . .	xviii
F.1	Figures of Merit for the selection of Fuel species . . . . .	xix
<b>G</b>	<b>Bibliography</b>	<b>xx</b>

# List of Figures

1.1	Functional analysis . . . . .	5
2.2	Logical chart of the design iterations <sup>[1]</sup> . . . . .	5
2.3	Load diagram for Max-Q . . . . .	7
2.4	Load diagram for worst case carrier maneuver . . . . .	10
2.5	Electron's Engine Bay <sup>[2]</sup> . . . . .	13
2.6	New engine configuration . . . . .	14
2.7	Tank thermal scheme . . . . .	14
2.8	$C_D$ and $C_L$ for the JEENO launcher . . . . .	16
2.9	Paneling Results . . . . .	17
2.10	CONOPS for MSA simulator . . . . .	18
2.11	Dynamic model of the rocket . . . . .	19
2.12	Orbit radius error mean and standard deviation . . . . .	21
2.13	Recovery architecture . . . . .	21
2.14	Ballute <sup>[3]</sup> . . . . .	22
2.15	First stage splashdown positions . . . . .	23
3.16	Final rocket shape . . . . .	24
3.17	Simulator positions and velocities . . . . .	25
3.18	Trajectory angles . . . . .	25
3.19	Simulator acceleration plots - payload point of view . . . . .	26
3.20	$Q$ -dyn and $m_{prop}$ . . . . .	27
3.21	Monte Carlo analysis . . . . .	27
3.22	Stages temperature during flight . . . . .	28
3.23	Cost per launch . . . . .	29
A.1	House of Quality . . . . .	i
B.1	Linear interpolation of GLOM and Launcher densities . . . . .	ii
B.2	Linear interpolation of payload mass and fairing densities . . . . .	ii
B.3	Linear interpolation of launcher diameter and fineness ratio . . . . .	iii
B.4	Definition of Cone Parameters . . . . .	vi
B.5	$\Delta\gamma$ Diagram . . . . .	vii
B.6	$k_x$ Diagram . . . . .	ix
B.7	Admissible Bending Moments compared to Effective during flight . . . . .	x
C.1	Linear interpolation of reduction force factor <sup>[4]</sup> . . . . .	xi
D.1	Vortex model used in determination of wing-tail interference <sup>[5]</sup> . . . . .	xiv
D.2	Crossflow drag coefficient of cylindrical section estimation . . . . .	xvi

# List of Tables

1.1	Mission level requirements . . . . .	1
1.2	System level requirements . . . . .	2
1.3	Item level requirements . . . . .	2
1.4	$\Delta V$ breakdown . . . . .	4
2.5	Properties of the Launcher Structural Materials . . . . .	10
2.6	Toxicity level for various chemical couples . . . . .	12
2.7	Emission level for various chemical couples . . . . .	12
2.8	Standard engine properties . . . . .	13
2.9	Modified engine properties . . . . .	14
2.10	Recovery System design parameters . . . . .	22
3.11	Length of launcher's components in [m] . . . . .	24
3.12	Mass distribution in [kg] for each stage . . . . .	24
3.13	Main parameters . . . . .	25
3.14	Flight events . . . . .	25
3.15	Cost Breakdown . . . . .	29

# Acronyms

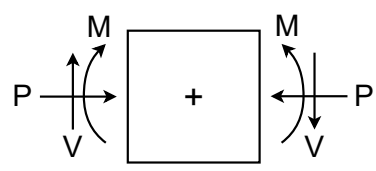
<b>AD<sup>2</sup></b>	Advancement Degree of Difficulty	<b>MECO</b>	Main Engines Cut Off
<b>AER</b>	Aerodynamics	<b>MER</b>	Mass Estimating Relations
<b>AoA</b>	Angle of Attack	<b>MMH</b>	Monomethylhydrazine
<b>CONOPS</b>	CONceptual OPerationS	<b>MSA</b>	Mission Analysis
<b>DCM</b>	Direct Cosine Matrix	<b>MTR</b>	Motor
<b>DOF</b>	Degrees Of Freedom	<b>NTO</b>	Nitrogen Tetroxide
<b>ECI</b>	Earth Central Inertial	<b>ODE</b>	Ordinary Differential Equation
<b>EOM</b>	Equations of Motion	<b>PID</b>	Proportional Integrative Derivative
<b>FoM</b>	Figure of Merit	<b>PRP</b>	Propulsion & Thermal Subsystem
<b>FoS</b>	Safety Factor	<b>RCS</b>	Recovery System
<b>GLOM</b>	Gross Lift-Off Mass	<b>ROI</b>	Return On Investment
<b>HoQ</b>	House of Quality	<b>RP1</b>	Rocket Propellant 1
<b>ISA</b>	International Standard Atmosphere	<b>SECO</b>	Second Engines Cut Off
<b>JEENO</b>	Jet Enabled Efficient Navigational Orbiter	<b>SSO</b>	Sun-Synchronous Orbit
<b>LCH<sub>4</sub></b>	Liquid Methane	<b>STR</b>	Mass and Structures
<b>LEO</b>	Low Earth Orbit	<b>TEHF</b>	Toxic and Environmental Hazard Figure
<b>LH<sub>2</sub></b>	Liquid Hydrogen	<b>TSTO</b>	Two Stage to Orbit
<b>LOX</b>	Liquid Oxygen	<b>TVC</b>	Thrust Vector Control
<b>LVA</b>	Launch Vehicle Adapter	<b>UDMH</b>	Unsymmetrical Dimethylhydrazine

# Nomenclature

$(C_{L\alpha})_t$	Tail lift-curve slope for angle of attack, per radian	$A_w$	Wing-alone aspect ratio [-]
$(C_{L\alpha})_w$	Wing lift-curve slope for angle of attack, per radian	$c^*$	Characteristic velocity [ $m/s$ ]
$\alpha$	Angle of attack [deg]	$C_D$	Drag coefficient [-]
$\beta A$	Wing alone or tail alone effective aspect ratio [-]	$C_g$	Center of Gravity [m]
$\Delta V$	Velocity variation [ $km/s$ ]	$C_L$	Lift coefficient [-]
$\delta$	Gimbal angle [°]	$c_r$	Chord at wing-body juncture or tail-body juncture [m]
$\dot{Q}$	Heat Flux [W]	$c_T$	Thrust coefficient [-]
$\epsilon_s$	Structural mass index [-]	$c_t$	Tail chord at midsection [m]
$\epsilon_{mat}$	Emissivity of Material [-]	$c_w$	Wing chord at midsection [m]
$\Gamma$	Flight path angle [rad]	$C_{D,base}$	Base drag coefficient [-]
$\gamma$	Buckling Knockdown Factor [-]	$C_{D,friction}$	Skin friction drag coefficient [-]
$\hat{x}$	Distance to center of pressure measured from intersection of wing leading edge and body for wing quantities and from intersection of tail leading edge and body for tail quantities [m]	$C_{D,n}$	Nose drag coefficient [-]
$\lambda$	Taper ratio [-]	$D_{ch}$	Combustion chamber diameter [cm]
$\lambda_{l,f}$	Latent heat of vaporization [ $kJ/kg$ ]	$D_{exit}$	Exit diameter [cm]
$\rho$	Density [ $kg/m^3$ ]	$D_{th}$	Throat diameter [cm]
$\rho_h$	Air density wrt altitude [ $kg/m^3$ ]	$E$	Young Modulus [Pa]
$\sigma^y$	Yield Strength [Pa]	$g_0$	Gravity constant [ $m/s^2$ ]
$\sigma_{SB}$	Stefan-Boltzmann Constant [ $W/m^2K^4$ ]	$Gr$	Grashof number [-]
$\theta$	Pitch Angle [rad]	$h$	Convective heat transfer coefficient [ $W/m^2K$ ]
$\varepsilon$	Expansion ratio of the nozzle [-]	$h_{opt}$	Altitude of optimal expansion [km]
$\varepsilon_c$	Contraction ratio of the nozzle [-]	$I_s$	Specific impulse [s]
$A$	Ballistic Parameter [-]	$K$	Thermal conductivity [ $W/mK$ ]
$a_h$	Speed of sound wrt altitude [m/s]	$K_{B(T)}$	Ratio of lift component of body in presence of tail [-]
$A_p$	Planform area [ $m^2$ ]	$K_{B(W)}$	Ratio of lift component of body in presence of wing [-]
$A_t$	Tail-alone aspect ratio [-]	$K_N$	Ratio of lift of body nose [-]
		$K_{T(B)}$	Ratio of lift component of tail in presence of body [-]
		$K_{W(B)}$	Ratio of lift component of wing in presence of body [-]

$L$	Total length of the engine [cm]	$Pr$	Prandtl number [-]
$l_s$	Distance from most forward point of body to shoulder of body nose [m]	$q$	Dynamic pressure [Pa]
$l_t$	Distance from most forward point of body to intersection of tail leading edge and body [m]	$q_\infty$	Free stream dynamic pressure [ $kg/m^2$ ]
$l_w$	Distance from most forward point of body to intersection of wing leading edge and body [m]	$r$	Body radius [m]
$M$	Bending Moment [Nm]	$r_N$	Body radius at shoulder of nose [m]
$m$	Mass [kg]	$r_t$	Body radius at tail [m]
$M_a$	Mach number [-]	$r_w$	Body radius at wing [m]
$m_s$	Cotangent of leading edge sweep angle [-]	$Re$	Reynolds number [-]
$M_{cr}$	Critical Bending Moment [Nm]	$S_t$	Tail alone area [ $m^2$ ]
$n_x$	Axial Load Factor [-]	$s_t$	Maximum semi-span of tail in combination with body [m]
$n_z$	Normal Load Factor [-]	$S_w$	Wing alone area [ $m^2$ ]
$Nu$	Nusselt number [-]	$s_w$	Maximum semi-span of wing in combination with body [m]
$OF$	Oxidizer to fuel ratio [-]	$T$	Temperature [K]
$P$	Axial Load [N]	$T_h$	Air temperature wrt altitude [K]
$p$	Pressure [Pa]	$t_f$	Filling Time [s]
$p_h$	Air pressure wrt altitude[Pa]	$Th$	Thrust [kN]
$P_{ch}$	Combustion chamber pressure [bar]	$Th_{vac}$	Thrust in vacuum [kN]
$P_{cr}$	Critical Axial Load [N]	$V_S$	Volume of body nose up to shoulder [ $m^3$ ]
$p_{hydro}$	Hydrostatic Pressure [Pa]	$V_\infty$	Velocity [ $m/s$ ]
		$x_{cp}$	Position of the center of pressure [m]

#### Convention for load diagram:



# Authorship declaration

Authorship declaration	
Surname	Technical tasks
Bachini	Mission analysis subsystem
Belletti	Project management & Mission analysis subsystem
Bolsi	Structure subsystem
Coacci	Aerodynamic subsystem
De Luca	Structure subsystem
De Marco	Recovery subsystem
Sciutto	Propulsion subsystem and thermal analysis
Tebaldi	Propulsion subsystem and thermal analysis
Vilhelem	Aerodynamic subsystem

# 1. Conceptual Analysis

The high-level objective of this study is to develop a LEO airborne space launcher, capable of inserting a payload into a specified orbit, while meeting a defined set of requirements and considering additional desirable features.

In this initial section, the requirements are identified and categorized for type and reference system. This is followed by a functional analysis and the development of a House of Quality to establish a clear relationship between the requirements and design choices, together with a competitors analysis to define the baseline. Finally, considerations regarding boundary conditions are discussed, including the selection of the baseline configuration and the aircraft platform chosen for the mission.

## 1.1 Requirements

Tables 1.1 to 1.3 present the requirements of the mission, divided in three levels: mission, system, and item, to ensure clarity and traceability throughout the design process. In each level, they are categorized as Functional (FUN), Operational (OPR), Performance (PER), and Verification (VER), and linked to relevant subsystems: [6,7]

- Mission (MIS): overall mission-level requirements
- Launcher platform (LCH): requirements related to the platform design and configuration
- Mass and Structures (STR): requirements about structural integrity and weight
- Motor (MTR): requirements linked to propulsion
- Recovery system (RCS): requirements addressing recovery and reusability
- Payload (PAY): requirements focused on payload specifics

### 1.1.1 Mission level Requirements

The mission-level requirements establish high-level objectives for the launcher system, covering payload delivery, timeline, economic feasibility, safety, and operational constraints. These are fundamental for guiding the overarching mission design.

Reqs.ID	Requirement
LSP-FUN-MIS-001	The mission shall be capable of inserting a payload into a LEO orbit
LSP-FUN-MIS-002	The time to market shall not exceed 4 years
LSP-FUN-MIS-003	The mission shall meet Return On Investment (ROI) targets with a small number of reuses
LSP-FUN-MIS-004	The mission shall employ a tandem configuration
LSP-FUN-MIS-005	The mission launch shall be safe for the people on ground
LSP-OPR-LCH-001	The launch platform shall be based on an existing design
LSP-OPR-LCH-002	The mission shall be launched from a civil aircraft
LSP-OPR-STR-003	The structure's thickness shall be manufacturable
LSP-OPR-STR-004	The structure should be assembled and transported horizontally

Table 1.1: Mission level requirements

### 1.1.2 System level Requirements

The system-level requirements define the performance and design expectations for key subsystems. These requirements ensure that the overall system achieves its intended functions under all conditions.

Reqs.ID	Requirement
LSP-FUN-RCS-006	The first stage shall be reusable
LSP-FUN-RCS-007	All stages should be recovered
LSP-FUN-STR-008	The structure shall maintain its shape under all operational conditions
LSP-FUN-STR-009	The structure shall sustain loads at Max-Q
LSP-FUN-STR-010	The structure shall sustain loads at attachment joints with the pylon of the carrier
LSP-PER-PAY-001	The maximum payload mass shall be 400 kg
LSP-PER-PAY-002	The accuracy of orbit insertion shall be 10 km
LSP-VER-PAY-001	Orbit insertion accuracy shall be verified using a Monte Carlo approach with model uncertainties
LSP-PER-PAY-003	The target orbit for a 250 kg payload shall be 400 km in a SSO at 98 degrees retrograde inclination
LSP-PER-RCS-004	For recovered parts, touchdown velocity shall be lower than 15 m/s for water recovery <sup>[4]</sup>
LSP-PER-STR-005	The inert masses shall be minimized

Table 1.2: System level requirements

### 1.1.3 Item level Requirements

The item-level requirements address specific components and subsystems, to asses detailed design criteria. These requirements are critical for component-level analysis and validation.

Reqs.ID	Requirement
LSP-PER-MTR-001	Propellant with low toxicity should be used
LSP-OPR-MIS-005	The carrier shall be a civil aircraft

Table 1.3: Item level requirements

### 1.1.4 House of Quality

In order to highlight the main requirements of the system and to compare it to currently operational solutions, a House of Quality was developed and the graphical representation is reported in section A.1. Analyzing the House of Quality it is possible to define the main parameters and their connections.

#### 1.1.4.1 Relevance of quality characteristics

The following key parameters are crucial as their variability highly impacts on the overall design and mission performance:

- **Payload mass:** its value influences all the design, starting from the structural mass to the trajectory optimization and thus the recoverability.
- **Number of stages:** the number of stages primarily impacts on the launcher mass. It has to be approached and fixed in first analysis since it shapes the whole mission.
- **Structural mass index:** significantly influences the inert masses of the launcher, thereby affecting the payload capacity of the mission. By minimizing inert masses, lower structural mass indices can be achieved, increasing the effective  $\Delta V$ <sup>[8]</sup>.

Other aspects to be taken care of are:

- **Height and velocity at staging:** staging conditions are critical for mission success. The first stage must provide sufficient velocity for the second stage to reach the target orbit. For recoverability, parachute deployment velocity and altitude must be carefully managed to minimize reentry heating and enable recover.

- **Safety factors:** here intended as the margins in the calculation, an adequate margin is necessary for reliability of the system and robustness in front of uncertainties. However, excessive margins can significantly increase mass.
- **Launcher diameter:** this parameter affects both logistics and performance. A significant change in diameter could hinder compatibility with the designed aircraft. Additionally, the diameter is closely linked to the structural and aerodynamic performance of the launcher. A larger diameter can sustain higher structural loads, but it also compromises aerodynamic efficiency by increasing drag.
- **Recovery location:** when choosing the launch location, attention must be paid in forecasting the impact location of the first stage, as it must be in a accessible and safe location.

#### 1.1.4.2 Competitors Analysis

This analysis wants to highlight the strengths and weaknesses of key competitors, but also to emphasize the bold innovations in our design. The main competitors and their respective launch vehicles are: Pegasus, LauncherOne, Bloostar, Ravn X, and Electron. The first four employ airborne launch strategies, while the last utilizes ground launch.

- Rocket Lab **Electron** is the biggest competitor, as it covers the our payload range of interest and it is partially reusable (first stage only)<sup>[9]</sup>. However, it is capable of delivering up to 300 kg to orbit, while our design surpasses these payload limits.
- Among airborne launchers, the Northrop Grumman, a longstanding leader in airborne launch strategies, has demonstrated the capability of its **Pegasus** rocket to deliver payloads of up to 450 kg into LEO<sup>[10]</sup>. With respect to our design, however, it lacks of reusability and it relies on solid propulsion, resulting in a higher environmental impact compared to our liquid propellant system. A similar analysis can be applied to **LauncherOne**, the vehicle developed by Virgin Orbit, which uses a two-stage liquid propulsion system, but lacks in terms of reusability<sup>[11]</sup>.
- Aevum's **Ravn X** also employs an air-launch configuration, but its key innovation lies in utilizing an unmanned carrier aircraft, significantly reducing risks to human life. However, like Pegasus, it faces similar challenges, particularly with reusability and environmental impact. Additionally, Ravn X has flown only a limited number of missions, raising questions about its operational viability<sup>[12,13]</sup>.
- Zero 2 Infinity's **Bloostar** solution consists of using a space balloon to carry the launcher up to a 20 km altitude and then igniting the first stage. This is an eco-friendly and low cost strategy, nevertheless it is limited in terms of payload, orbit reachability, and lacks stage reusability, which is a significant drawback in terms of long-term sustainability and cost efficiency<sup>[14] [15]</sup>.

From the analysis, it is evident that while each competitor introduces valuable innovations, none fully addresses the combined challenges of payload capacity, reusability, environmental impact, and cost efficiency. Our design surpasses these limitations by combining higher payload capacity, liquid propulsion for lower environmental impact, and the potential for full reusability, representing a transformative step forward in the small satellite launch industry.

#### 1.1.4.3 Baseline

In accordance with the competitors' analysis in 1.1.4.2, real rocket data, including properties and technical specifications, were used as baseline data to initiate the conceptual design phase.

These rockets share critical technologies with the proposed design. Among the available options, Pegasus, LauncherOne, and Electron were selected as baselines. The design parameters and geometries were derived from available datasheets and subsequently applied to the conceptual model. This approach provided a foundational dataset for the development of the system design presented in subsection 2.1.3. The results and the approach are further detailed in section B.1.

### 1.1.5 Aircraft Platform

The selected aircrafts for this mission are the **Boeing 747-200SF**, **Boeing 747-400** and **Boeing 767-300ER**, identified after a preliminary screening of multiple platforms. The Lockheed L-1011 TriStar was excluded due to outdated technology, the lack of available maintenance support and spare parts, which would have increased operational risks and costs. Similarly, the Scaled Composites ROC, while innovative, was deemed unsuitable because of its limited airport operability and reduced payload flexibility.

The **Boeing 747-400** benefits from a proven precedent for airborne launch operations, as demonstrated by Virgin Orbit<sup>[11]</sup>, simplifying certification and reducing risks. Its larger airframe allows for the accommodation of heavier launchers and auxiliary systems, providing flexibility for future mission expansions. However, the high acquisition and operational costs, coupled with inefficiency if used for payloads smaller than its maximum capacity, limits its economic viability for missions with moderate payloads and flight frequencies. It also benefits from an established certification process, resulting in a moderate AD<sup>2</sup> Risk Rating of 5. However, its higher operational costs challenge ROI for missions with lower flight frequencies.

The **Boeing 767-300ER** presents a strong case in terms of fuel efficiency, being nearly twice as efficient as 747 series<sup>[16]</sup>. Its payload capacity is well-matched to small and medium-scale missions, which minimizes unnecessary overhead. However, its lack of precedent in airborne launch operations introduces higher certification risks and potential delays. Furthermore, the limited payload capacity restricts its adaptability for larger or more complex future mission requirements. It carries a higher AD<sup>2</sup> Risk Rating of 7 due to the uncertainties of certifying a new platform for airborne launches, which introduces delays and increases risks.

The **Boeing 747-200SF** emerges as the most balanced choice for this mission. It combines the advantages of a cargo-configured airframe, proven reliability, and cost-effectiveness<sup>[17,18]</sup>. Its lower acquisition costs compared to the 747-400 make it an attractive option for projects with constrained budgets, while its operational flexibility allows for the integration of launch systems without extensive structural modifications. Supported by global network of maintenance facilities<sup>[17]</sup>, the 747-200SF ensures consistent availability, reducing downtime and long-term operational risks. Although slightly less fuel-efficient than the 767-300ER<sup>[16]</sup>, its overall adaptability and reduced modification costs make it a superior choice for ensuring both cost efficiency and mission success. In comparison to the other platforms, it balances proven reliability with manageable certification challenges, achieving a moderate AD<sup>2</sup> Risk Rating of 6.

In conclusion, the **Boeing 747-200SF** offers the best compromise between cost, risk, and performance. It balances proven reliability, operational flexibility, and economic feasibility, making it the ideal choice for the current mission while maintaining adaptability for future requirements.

### 1.1.6 Mission Budget Estimation

The mission budget was estimated with a semi-analytical approach, where the launch mission was modeled as a  $\Delta V$  of an Hohmann-like transfer from the launch position to the target orbit, while the losses were estimated based on the values from the literature<sup>[8]</sup>.

$\Delta V_{mission}$ [km/s]	$\Delta V_{g-loss}$ [km/s]	$\Delta V_{d-loss}$ [km/s]	$\Delta V_{s-loss}$ [km/s]	$\Delta V_{w-loss}$ [km/s]	$\Delta V$ [km/s]
7.45	1.5	0.225	0.1	0.45	9.725

Table 1.4:  $\Delta V$  breakdown

For the launch mission, the initial velocity was computed from the Mach number of the carrier and the thermodynamic variables of air at the carrier's altitude, while the target velocity was set to the orbital speed<sup>[19]</sup>. To estimate the losses, typical values from the literature were used. Moreover, steering ( $\Delta V_{s-loss}$ ) and wind ( $\Delta V_{w-loss}$ ) losses were also computed along gravity ( $\Delta V_{g-loss}$ ) and drag ( $\Delta V_{d-loss}$ ) losses. Upper-bound values were chosen based on interval specifications for medium

to large launchers.<sup>[1,6,20,21]</sup> The results of the analysis are reported in Table 1.4.

As it can be observed, the ideal  $\Delta V_{mission}$  is slightly below the minimum one to achieve LEO<sup>[19]</sup> thanks to the initial velocity given by the carrier, which amounts to 183 m/s<sup>[22]</sup>.

### 1.1.7 Functional Analysis

The goal of the functional analysis shown in Figure 1.1 is to identify the functions the system has to carry out in order to successfully accomplish the mission. By decomposing these functions, it is possible to highlight the principal operations and to order them in a logical sequence. The dashed line blocks represent functions not carried out in this analysis, while all the others are addressed.

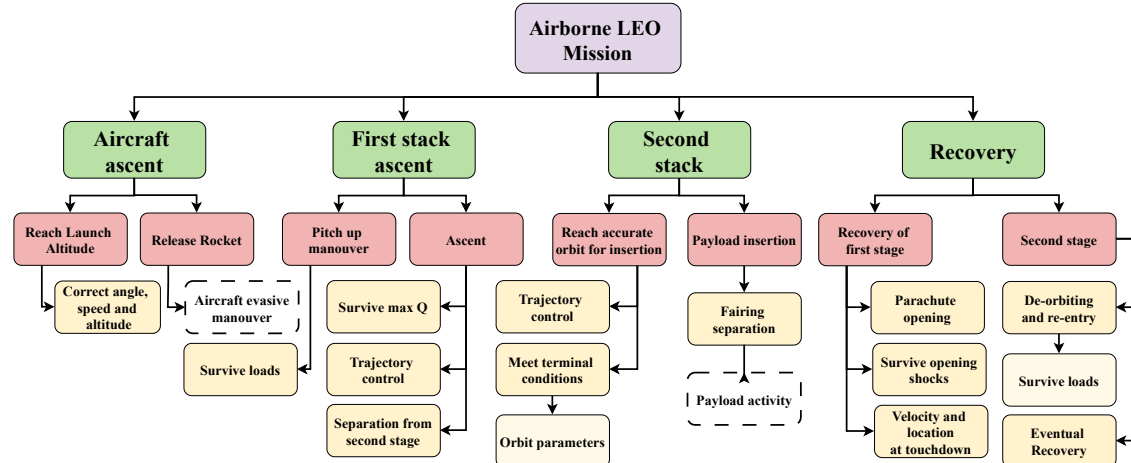


Figure 1.1: Functional analysis

## 2. Development

The workflow for the design of each subsystem is presented in the following section. Since all the subsystems are interconnected with each other, the design phase was an intrinsic iterative process in which all the subsystems were acting as inputs and outputs. A very synthetic scheme of this process is represented in Figure 2.2.

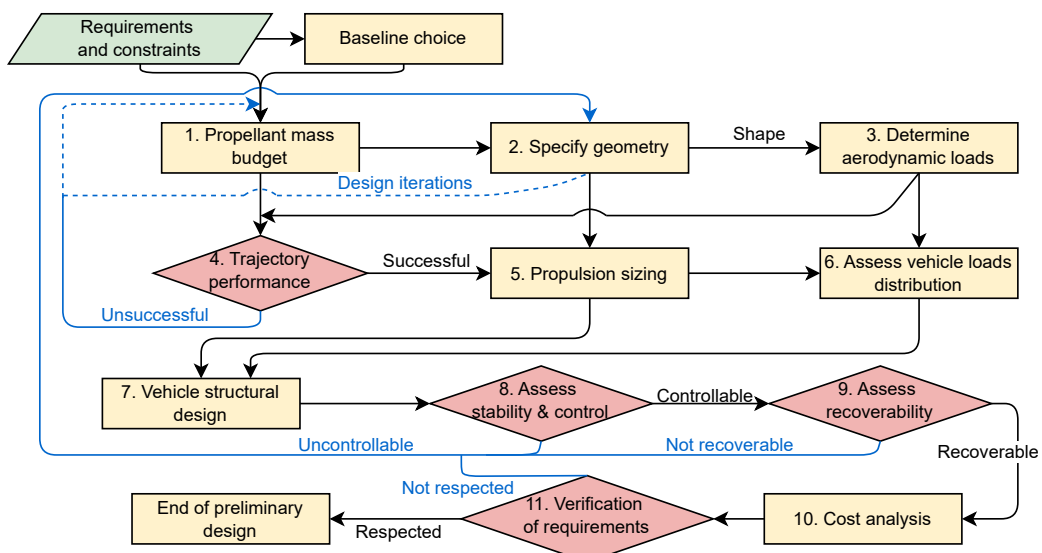


Figure 2.2: Logical chart of the design iterations<sup>[1]</sup>

## 2.1 Mass and Structures

In this section, the procedure to estimate the masses of the launcher is described. This process is related to the loads that the vehicle shall sustain throughout all the mission.

### 2.1.1 Iterative Method for Optimal Staging

The prescribed configuration for the launcher is a tandem staged rocket (Section 1.1.1), but the number of stages is free to be chosen. Starting from a competitor analysis for similar payloads and target orbits<sup>[9,10,11]</sup>, the configuration that could best suit the market sector is a TSTO, which has been widely used for the required orbits<sup>[9,11]</sup>.

In a preliminary design, the minimum liftoff mass can be found, through optimal staging, exploiting *Lagrange Multipliers* and ignoring the in-flight  $\Delta V$  losses<sup>[23]</sup>. However, this method assumes the knowledge of the *Structural Mass Index* of each stage ( $\epsilon_s$ ) *a priori*.

Generally, the computed  $\epsilon_s$  at the first iteration are different from the ones initially hypothesized, leading to incoherent results in the propellant allocation and in the  $\Delta V$  capability of the launcher. This happens because the real value of the inert mass depends on many quantities that are defined as percentages or functions of the total mass (initially unknown), as explained in subsection 2.1.3. To avoid this mismatch, an iterative loop cycle was implemented, following this workflow:

1. Optimal Staging with initial guesses ( $\epsilon_{s1}$ ,  $\epsilon_{s2}$ ,  $I_{s1}$ ,  $I_{s2}$ ) and fixed  $\Delta V$  and Payload Mass
2. Computation of inert masses from propellant masses (output of Optimal Staging)
3. Re-compute  $\epsilon_{s1}$ ,  $\epsilon_{s2}$  and correct for the following iterations

This method uses as stopping criteria the norm of the difference of the newly computed  $\epsilon_s$  with the old ones, until a prescribed tolerance is respected. The iterative approach is reported in section B.2.

The specific impulses used are fixed by the choice of the engines and by the nozzle expansion ratios (section 2.2).

The  $\Delta V$  for the first iteration comes from Section 1.1.6, while the following ones iteratively exchange information (mass  $\leftrightarrow \Delta V$ ) with MSA. Furthermore, the diameters of the two stages are not fixed by design; instead, they were initially assumed for inert mass calculations and later adjusted to ensure compatibility with standard geometrical parameters found in literature, such as the *fineness ratio*.

### 2.1.2 Factor of Safety

At the early stage of this project, a FoS of 1.5 has been adopted for the structures. There is no universally accepted standard within the space community for this value<sup>[24]</sup>, however, since the first stage is designed to be reusable, a higher FoS could help increase fatigue resistance via stress reduction<sup>[25]</sup>. In the aerospace industry this kind of FoS is generally used for ultimate strength, thus making the assumed value conservative<sup>[26]</sup>.

### 2.1.3 Inert Masses Estimation

In this section, the methodology for mass estimation utilized in the algorithm outlined in subsection 2.1.1 is described.

**Payload and Launch Vehicle Adapter:** In literature<sup>[1]</sup>, the payload mass of a launcher is not only the effective payload to be inserted in orbit, but includes also the LVA that connects the payload to the rocket. While the required payload mass  $m_P$  is known and equal to 250 kg, the LVA mass can be estimated as  $m_{LVA} = 0.0755 \times m_P + 50\text{kg} = 318\text{kg}$ <sup>[1]</sup>.

**Engines:** As explained in section 2.2, the first stage has eight 40kg engines, while the second stage has one 45kg engine. This results in a total mass of 345kg, already accounting for pumps, gimbals and batteries<sup>[27]</sup>.

**Tanks, Forward Skirts, Intertanks and After Skirts:** The tanks are designed to function as

structural support elements. Along with the forward skirts, intertanks and after skirts, their dimensions are sized based on the allocated propellant mass (Section 2.1.3), while the thickness depends on the applied loads (Section 2.1.4). The minimum required thickness to prevent structural failure is calculated using the defined surface area, material properties, and a specified Safety Factor (FoS) (subsection 2.1.2). Additionally, the intertanks feature a *common dome design*, a configuration commonly employed to minimize the inert mass associated with elliptical domes and the overall length of the launcher<sup>[1]</sup>.

**Fairing:** It protects the payload from atmospheric and radiation effects during ascent, detaching at an altitude of 100–110 km<sup>[28,29]</sup>, near the first staging point (subsection 3.1.1). Its mass is attributed to the first stage, slightly overestimating the total  $\Delta V$ . This impact is negligible, as the fairing remains briefly with the second stage and its mass is small with respect to its stack. The fairing mass is calculated as 2.95 times its external surface area raised to an exponent of 1.15<sup>[30]</sup>. The surface area is modeled as a cone, with a height twice its base diameter, which matches the second stage's final diameter determined from tank sizing<sup>[1]</sup>.

All the other inert masses, which are **Avionics**, **Wiring**, **Thrust Structure**, **Recovery System**, **LOX Insulation**, and **Fins**, are accounted via MER<sup>[1,30,31]</sup>. However, no MER was found for the **Fins Actuators**; therefore, an average value of 185.0kg<sup>[32]</sup> was added to the first stage. An in-depth analysis can be found in section B.3.

#### 2.1.4 Loads Analysis

The purpose of the loads analysis is to determine the minimum thicknesses required for the tanks and skirts to sustain the launcher throughout the mission.

The worst-case scenario for the overall structure combines the following effects:

- Longitudinal acceleration from engine thrust at the rear of the rocket, considering a value of 6g in the last iteration.
- Normal acceleration from aerodynamic forces acting on the nose and tail sections. A value of 1g was taken in the end.
- Aerodynamic force acting in the x-body direction of the rocket, provoking a compressive load that sums with the longitudinal acceleration.

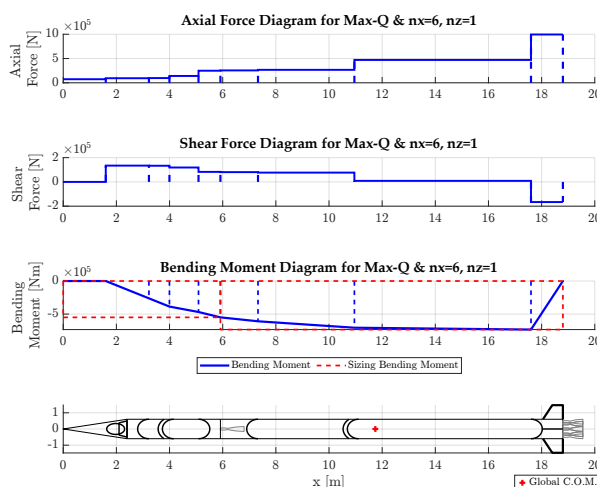


Figure 2.3: Load diagram for Max-Q

center of pressure of the fins coincides with the vehicle's base. This assumption is supported by the fact that the distance between the base and the application point of the fin lift is small relative to the overall length of the segments. All these sizing parameters were adapted with MSA results.

The plots in Figure 2.3 show acceleration and loads according to the convention defined in the Nomenclature. It was demonstrated that the loads were consistent with the values estimated

To evaluate the aerodynamic forces, a Max-Q = 50 kPa is taken with an angle of attack equal to 10°. Under these conditions, the drag and lift coefficients with the pertinent reference area were automatically adapted to each iteration geometry (section 2.3).

These values were chosen to provide a conservative safety margin for the structural design, as they correspond to the worst-case acceleration and dynamic pressure that a civil launcher might encounter; regarding the angle of attack, the choice is related to the limit of the slender body theory<sup>[1]</sup>. Under these maximum dynamic pressure condition, the load distribution depicted in Figure 2.3 was calculated by assuming a full vehicle during Max-Q and that the

in section 2.4, section 2.3, and section 2.5. Throughout the complete trajectory, the identified Max-Q and Max-Q $\alpha$  conditions remained within the hypothesized values, thereby validating our model. Notably, at the rear of the vehicle, the axial and shear loads correspond to the thrust level theoretically required under these conditions and the lift generated by the fins, respectively. All the other loads scenarios were compared to these to validate the strength of the structure (see subsection 2.1.6, subsection 2.5.2). For the design of each stage, the maximum bending moment within its section of the distribution was used as the design load, as highlighted in red in Figure 2.3. Thus, the thicknesses were assumed to be identical inside the single component, but differ from the other parts. This ensures each stage can withstand a high constant bending moment across its entire length, providing an additional safety margin for unexpected load cases<sup>[33]</sup>.

#### 2.1.4.1 Failure Modes

Two failure modes are considered:

1. Excessive longitudinal and transversal stresses leading to plastic deformation along the length or in the hoop of the components (further details in section B.4).
2. Excessive compressive and bending loads causing buckling (further details in section B.5).

These failure modes impose **six** constraints on the minimum thicknesses, ensuring the following **six** resistances that must be respected in the elastic field of the material. Each of the **six** corresponds to a minimum thickness value, thus the thickness chosen for each component will be the maximum of these values. The load parameters  $P$ ,  $M$ ,  $p$ ,  $p_{hydro}$  used to evaluate the **six** constraints are explained in 2.1.4.2.

1. **Axial** resistance of the **bottom** part of the tanks to  $P$ ,  $M$ ,  $p$ ,  $p_{hydro}$ , thus when the rocket is flying and accelerating.
2. **Axial** resistance of the **top** part of the tanks to  $P$ ,  $M$ ,  $p$ , thus when the rocket is flying and accelerating.
3. **Hoop** resistance of the tank to  $p$ ,  $p_{hydro}$ , that represents the load condition of the bottom part of the tanks when the rocket is flying and accelerating (worse case than on the top of the tank).
4. **Axial** resistance of the inert mass to  $M$  (with  $p = p_{hydro} = 0$ ), that is the bending moment acting on the rocket when it is statically horizontal before refueling the tanks.
5. **Buckling** resistance of the inert mass to  $M$  (with  $p = p_{hydro} = 0$ ), that is the bending moment acting on the rocket when it is statically horizontal before refueling the tanks.
6. **Buckling** resistance of the inert mass to  $P$ ,  $M$ ,  $p$ , that represents the worst buckling load condition when the rocket is flying and accelerating.

#### 2.1.4.2 Definitions of Load Parameters

**P**: The compressive load sustained by each part. This load is the sum of the weight of the supported components (accelerated during flight) and the aerodynamic drag at **Max-Q**.

**M**: The bending moment acting on the rocket during the worst-case scenario, which corresponds to a condition of transversal acceleration with forces applied on the nose and tail fins. To model it, the launcher was divided into its primary components, each assigned a specific mass.

**p** (Tanks): The internal pressurant gas pressure within the tank shells. During flight, a minimum pressure of  $p = 0.5$  MPa<sup>[34]</sup> is maintained to prevent cavitation in the turbopumps. Before refueling, **p** is set to zero.

**p** (Skirts): For intertanks, interstages, and after skirts, the internal pressure **p** is always set to zero in all operational conditions.

**p<sub>hydro</sub>**: The hydrostatic pressure caused by fluids pushed to the bottom of the tanks during acceleration. This pressure is always set to zero for skirts. For tanks, **p<sub>hydro</sub>** is zero only before refueling

and during flight is computed using Stevin's Law:

$$p_{hydro} = \rho g_0 n_x h$$

where:  $g_0 n_x$  is the maximum longitudinal acceleration (initially set at 10g, later refined through iterations);  $h$  is the height of the fluid within the vessel, which depends on the tank geometry;  $\rho$  is Volumetric density of the fluid stored in the tank that is  $\rho_{LOX} = 1140 \text{ kg/m}^3$ <sup>[1]</sup><sup>[35]</sup> and  $\rho_{RP-1} = 820 \text{ kg/m}^3$ <sup>[1]</sup><sup>[35]</sup>.

An additional constraint on the manufacturability of the thicknesses for the materials selected should be introduced, and the details are discussed later on in Section 2.1.5.

## Buckling

Two NASA sources were used to assess the structure capability to withstand the described loads from a buckling perspective: *NASA SP-8007*<sup>[36]</sup><sup>[37]</sup> & *NASA SP-8019*<sup>[38]</sup>. The procedure involves determining the critical compressive axial load  $P_{cr}$  and bending moment  $M_{cr}$ , which depend on internal pressure, geometry, material properties, and thickness. These critical values are then compared with the actual loads to ensure they remain within acceptable limits.

For combined stresses, where axial compression and bending act simultaneously, the following constraint must be satisfied:

$$\frac{P}{P_{cr}} + \frac{M}{M_{cr}} < 1 \text{ [37]} \quad (2.1)$$

The formulas used are purely empirical and generally considered conservative, making them suitable for early-stage design<sup>[37]</sup>. The comprehensive details of the buckling approach are thoroughly documented in section B.5.

### 2.1.5 Materials Selection

The adopted materials are different for the two stages because they have to fulfill different requirements (Section 1.1.2): the first shall be reusable, the second can sacrifice reusability to minimize weight.

In particular, the material for the first stage must withstand fatigue, corrosion, and stress-corrosion (particularly in case of splashdown), while also tolerating the high temperatures encountered during re-entry. Additionally, it must exhibit a high strength-to-weight ratio.

Given these criteria and its proven track record in the field<sup>[1]</sup>, the chosen material is Aluminum Alloy 2219. This alloy has been extensively used for tank walls and offers superior resistance to stress-corrosion cracking compared to other alloys<sup>[1]</sup>. Moreover, it is a suitable choice to store LOX as it is able to maintain its mechanical integrity at cryogenic temperatures<sup>[39]</sup>. However, due to its affinity with LOX, one potential solution involves physically separating the oxidizer from the aluminum alloy using a non-reactive material such as Stainless Steel (specifically SS304L), which is known to be chemically compatible with LOX<sup>[40]</sup>.

From Section 2.1.4, it is clear that reducing the second stage's weight is critical for overall mass savings. A lighter second stage decreases the loads on the first stage, allowing its structure to be lighter as well. Additionally, a lighter second stage requires less fuel to achieve the same  $\Delta V$ , significantly impacting on the mass savings. For this reason, graphite composites, known for their exceptional strength-to-weight ratio and successful use in previous missions<sup>[1,9]</sup>, are selected for the second stage. Furthermore, composites have been proven to be able to successfully store cryogenic propellants such as LOX, which further proves the choice as suitable for this vehicle<sup>[41]</sup>.

Lastly, the material selection was verified to be compliant with the design choice of a common bulkhead for both the first and second stage tanks. The use of aluminum for common dome configurations has a well-established track record of reliability dating back to the early days of space exploration.<sup>[42]</sup>. Similarly, composite materials for common domes have demonstrated their effectiveness in more recent space missions, further validating this selection<sup>[43,44]</sup>. In Table 2.5 the most relevant characteristics of the chosen materials are summarized.

Properties	Aluminum 2219	Carbon Fiber/Epoxy comp.
Density [kg/m <sup>3</sup> ]	2840 <sup>[45]</sup>	1420 <sup>[46]</sup>
Yield Tensile Strength [MPa]	350 <sup>[45]</sup>	1260 <sup>[46]</sup>
Young Modulus [GPa]	73.1 <sup>[45]</sup>	101 <sup>[46]</sup>
Poisson's Ratio [-]	0.33 <sup>[45]</sup>	0.286 <sup>[46]</sup>
Minimum Thickness [mm]	0.5 <sup>[47]</sup> <sup>[48]</sup>	3.0 <sup>[49]</sup>

Table 2.5: Properties of the Launcher Structural Materials

Also minimum thicknesses (Table 2.5) for the manufacturing process must be considered, thus it was verified that the thicknesses obtained from subsection 2.1.4 all observe this bound.

### 2.1.6 Attached Configuration

Once the structure's thicknesses are evaluated to ensure the vehicle can withstand flight loads, its attached configuration is analyzed to assess its mechanical capability to handle the loads at the carrier's attachment joints during flight.

To analyze this condition, the launcher is modeled as a beam with masses concentrated at the barycenter of each section. These sections are defined according to the locations of the constraints, resulting in three distinct regions: one preceding the constraints, one enclosed by the constraints, and one aft of the constraints. The loads are evaluated for the worst case maneuver scenario where the launcher is subjected to both axial and longitudinal accelerations of 2g<sup>[50]</sup>. This model is typically implemented as a preliminary approach to size the reactions on the constraints; a more refined approach, via distributed loads, leads to a higher accuracy on the estimation of the displacements and minor corrections on the reaction forces<sup>[51]</sup>.

In this scenario, the FoS is maintained as in subsection 2.1.2 due to the fact that it is a compromise between the knowledge on the system and the accuracy of the models that have been implemented<sup>[52]</sup>. Moreover, the aerodynamic forces acting on the nose and the tail fins have been considered under the flight conditions of the Boeing 747<sup>[22]</sup>.

The constraints on the launcher are modeled as a hinge and a roller, a standard approach for such configurations under the previous assumptions<sup>[33]</sup>. These constraints are placed on the first-stage body, which has the greatest thickness within the vehicle, making it capable of withstanding the high concentrated loads on the supports. Furthermore, the distance between the two attachment points is defined based on the maximum chord at the fifth pylon of the airplane and ensuring that the global center of mass is enclosed by these constraints<sup>[53]</sup>. Once this framework is established, the reaction forces and load diagrams are evaluated as reported in Figure 2.4.

As depicted in Figure 2.4, the global center of mass lies within the two constraints. A moment is present at their location, as these constraints do not divide the structure but instead support it while still restricting its rotation, owing to the absence of a common center of instantaneous rotation<sup>[51]</sup>.

Additionally, the shear force diagram closes at the rear of the launcher with a value equal to the lift contribution from the fins, while the axial forces at this location are zero: reflecting the absence of an axial load. Thus, the structural analysis, conducted as outlined in subsection 2.1.4, confirmed that this configuration does not result in higher stresses compared to the design case. Consequently, the structure can withstand the worst-case maneuver involving 2g forces exerted by the carrier<sup>[25]</sup>.

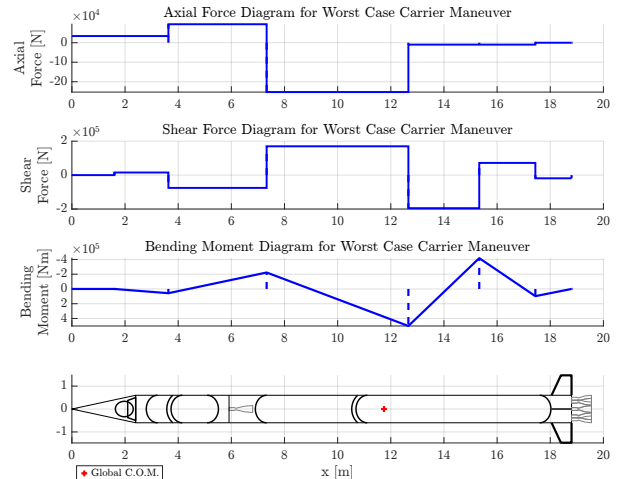


Figure 2.4: Load diagram for worst case carrier maneuver

## 2.2 Propulsion system and Thermal Analysis

### 2.2.1 Introduction

The propulsive subsystem is another crucial aspect in the design of JEENO. All decisions made by the team during development aimed to ensure the correct amount of thrust and, at the same time, the best performances in terms of specific impulse  $I_S$ , mass and volume; additionally, every effort was made to meet the short time-to-market constraint imposed by the customer.

Given this tight timeline, the team deemed the development of new engines from scratch to be way too risky, then deciding to opt for buying something off-the-shelf. However, the four-years time span allows to adjust the chosen system to better meet the system's requirements.

### 2.2.2 Architecture choice

The first analysis led to select the propulsive technology for both the first and second stage.

First, it was decided to opt for a liquid, pump-fed<sup>1</sup>, bipropellant system, rather than a solid one. Although this choice involves some complexities in the architecture (storage of eventual cryogenic species and the need of moving parts), it offers several advantages:<sup>[54]</sup>

- re-usability – with proper recovery, liquid system can reliably deliver high performance across multiple launches, as requested by the customer;
- controllability – liquid systems allows for fine regulation of the throttle levels, and consequently of the thrust provided, ensuring a better control;
- flexibility – liquid systems can be reignited, allowing the same engine to be used in different mission phases (e.g. during ascension and recovery);
- heritage – chemical liquid systems are widely used in rocketry to place payloads in orbit, as they guarantee both high levels of thrust and specific impulse.

### 2.2.3 Chemical couple choice

While the oxidizer species is immediately identified as cryogenic liquid oxygen (LOX)<sup>[1]</sup>, the selection of the fuel required careful considerations of several key figures of merit: typical specific impulse, storage temperature, density and market availability. The latter, in this context, refers to the number of existing engines that are flight proven, still in production and that, individually or in combination, can guarantee a thrust level comparable to the baseline (detailed procedure available in Appendix F.1). The results are the following:

- Rocket Propellant 1 (RP1) – has the highest market availability and density; it's the easiest to maintain at the correct temperature, but it has, by a small margin, the worst specific impulse;
- Liquid Hydrogen (LH<sub>2</sub>) – has the highest specific impulse, but it is by far the worst in all the other categories;
- Liquid Methane (LCH<sub>4</sub>) – sits halfway between the other two for specific impulse and density, while the other two FoM are closer to the bottom line.

Other chemical couples that have been taken into account, in particular for the second stage, were oxygen-monomethylhydrazine (LOX-MMH) and nitrogen tetroxide-dimethylhydrazine (NTO-UDMH), but were discarded because of the requirement of using non-toxic propellants. The toxicity is evaluated through the Toxic and Environmental Hazard Figure (TEHF), a parameter that takes into account the  $LD_{50}$  index and the mass of chemicals necessary to reach a GEO orbit. The values of this parameter are presented in table 2.6: the higher the value, the more toxic the propellants<sup>[55] [56]</sup>.

---

<sup>1</sup>Blowdown is advisable for orbital maneuvers and third stages, otherwise pump-fed is preferred<sup>[1]</sup>

COUPLE	LOX-RP1	LOX-LH2	LOX-LCH4	LOX-MMH	NTO-UDMH
TEHF	0.19	0	0	3.62	26.26

Table 2.6: Toxicity level for various chemical couples

The emission aspect is instead quantified with the equivalent mass of carbon dioxide per equivalent hydrogen mass of fuel ( $CO_2$  eq. per  $H_2EM$ , equivalent  $CO_2$  mass emitted by the mass of propellant necessary to obtain the same amount of thrust of an hydrogen-based system), that also includes the emissions due to the production of the chemical, and whose value is reported in table 2.7<sup>[57]</sup>. As can be seen, the only toxic couple reported has also the highest polluting factor; LH2 emissions are mainly due to its highly energetically demanding production, while RP1 is less environment-friendly than LCH4 because it is a longer hydrocarbon chain.

COUPLE	LOX-RP1	LOX-LH2	LOX-LCH4	NTO-UDMH
$CO_2$ eq. per $H_2EM$ [kg]	17.3	23.7	7.5	77.8

Table 2.7: Emission level for various chemical couples

Given all these evaluations, **LOX-RP1** was chosen for the propulsive subsystem of JEENO.

#### 2.2.4 Engine choice

The focus then went in identifying the commercially available RP1-LOX engines that, in single- or multi-engine configurations, could provide thrust in the predicted range of the baseline [150 – 300] kN (Section 1.1.4.3), and allow for sufficient gimbal. The resulting products have been identified in:

- Rocketlab's **Rutherford engine** – This 3D printed, electric-pump-fed engine stands out as one with the most flight heritage and the only one with a history of reuse. It is currently used on the Electron rocket, which utilizes 9 engines, each with a thrust of 24kN<sup>[9]</sup>, needing a multi-engine configuration to achieve the required total thrust. A multi-engine setup has both advantages and drawbacks. On the positive side, it grants redundancy in case of failure, greater attitude control (including roll ability), and a reduction in total engine bay length. However, it also involves a larger number of moving parts, as each engine comes with its own pump. This drawback is mitigated by the absence of a turbine, thanks to the electric-pump-fed design, and thus the replacement of turbines with electric batteries, which also have a better efficiency<sup>[58]</sup>.
- Virgin Orbit's **Newton 3 engine** – This engine has been used on the air-launched rocket LauncherOne, albeit just 6 times, and has no reuse history<sup>[59]</sup>. This would be a traditional single engine turbopump-fed configuration. Its supply would be difficult since the company went bankrupt in 2023<sup>[60]</sup>, hence a redesign contacting old suppliers and hiring ex-engineers would be necessary. Moreover, its thrust just over 300kN<sup>[11]</sup> would probably be too high.
- Firefly's **Reaver engine** – This engine is used on the Firefly Alpha rocket, and is set to fly on Astra's Rocket4 as a down-powered version named Chiron<sup>[61]</sup>. Its thrust (respectively 209<sup>[62]</sup> and 166 kN<sup>[63]</sup>) would be sufficient only for a very light rocket, while a double-engine configuration would have too much thrust.

As a conclusion, the Rutherford Engine was selected for both the first and the second stage. The advantages of this choice are even greater than previously described:

- the thrust can be tuned not only with throttling, but by varying the number of engines; this way, at startup all engines are supposed to work at full thrust, optimizing their capabilities.
- the engines are easily modifiable since they are 3D printed<sup>[27]</sup>, so the engine geometry can be tuned to adapt performance. This will actually be exploited in Section 2.2.5.

The engine physical and performance parameters are the following:

<b>D<sub>ch</sub></b> [cm]	<b>D<sub>throat</sub></b> [cm]	<b>D<sub>exit</sub></b> [cm]	$\varepsilon_c$ [-]	$\varepsilon$ [-]	<i>L</i> [cm]	$\theta_e$ [deg]
11	6	24	3.36	16	65	12
<b>T<sub>h</sub>liftoff</b> [kN]	<b>I<sub>s</sub></b> [s]	<b>OF</b> [-]	<b>P<sub>ch</sub></b> [bar]	$\delta$ [deg]	<b>h<sub>opt</sub></b> [km]	$\dot{m}_{prop}$ [kg/s]
24	312	2.6	57.357	7	9.5	8.82

Table 2.8: Standard engine properties

The physical dimensions of the engines listed in Table 2.8 were obtained from Figure 2.5: known the diameter of the rocket ( $1.2m$ )<sup>[9]</sup>, other measurements are validated and then taken. The diameters listed for chamber, throat and nozzle exit are retrieved by subtracting the wall thickness (average of 5 mm<sup>[64]</sup>) from the outer dimensions (12.5, 7 and 25 cm respectively Figure 2.5).

The chamber pressure has been retrieved by solving the Tsolkovsky equation: knowing the liftoff thrust (hence also ambient pressure) and physical dimensions, the remaining parameters  $P_e$ ,  $I_s$  and  $c^*$  are linked to the chamber pressure using NASA CEA.

The vacuum optimized engine is an unmodified version of the one installed on the Electron's second stage ( $I_s = 343$  s)<sup>[9]</sup>.

### 2.2.5 Nozzle modification

The 4 years time-to-market allows to apply some modifications to the original design, in order to adapt it to the actual operative conditions.

The Rutherford engine is designed to be mounted on a classical ground-launched vehicle, so its nozzle has an optimal expansion altitude of about 9 km (computed with CEA, starting from parameters in Table 2.8 via exhaust pressure); JEENO is released from the carrier airplane at around 11 km from the ground, which means that a standard engine would be under-expanded for the whole duration of the mission. A new design for the nozzle would increase the overall performances of the system.

Starting from the original geometrical properties of the engine, along with the chamber pressure, the team re-designed the divergent section with the goal of maximizing expansion.

The constraints for the computation of the exit diameter are:

- number of engines  $N$  – the chosen configuration presents one central engine and  $N - 1$  equally spaced engines in the outer ring (optimal configuration for  $N \geq 6$ , from basic geometry of regular polygons);
- total thrust – the chosen engines, cumulatively should be able to provide a suitable liftoff thrust (between 1.3 and 1.5 times the weight of the whole rocket at launch)<sup>[1]</sup>
- maximum gimbal angle  $\delta$  – since the gimbal of every engine is independent, the sizing is done such that when an engine is fully tilted it doesn't touch the nearby one "at rest";
- external diameter of the rocket – the whole system "at rest" ( $\delta = 0^\circ$ ) must remain entirely within the diameter of JEENO to avoid any interference with its connection to the carrier.
- nozzle shape – the nozzle should be a continuation of the standard nozzle shape, elongated according to RAO nozzle standards<sup>[65]</sup>.

Once the geometrical properties of the new nozzle are defined, it is finally possible to retrieve the performances of a single engine at full throttle from NASA CEA; in Table 2.9 the results obtained are resumed, while in Figure 2.6 is depicted the new configuration.


Figure 2.5: Electron's Engine Bay<sup>[2]</sup>

$D_{exit}$ [cm]	$\varepsilon$ [-]	$L$ [cm]
31.73	27.97	75.3
$T_{h\text{launch}}$ [kN]	$T_{h\text{vac}}$ [kN]	$I_s$ [s]
28.024	28.247	324.5
$\theta_e$ [deg]	$c^*$ [m/s]	$h_{\text{opt}}$ [km]
7.8	1838.1	15.6

Table 2.9: Modified engine properties

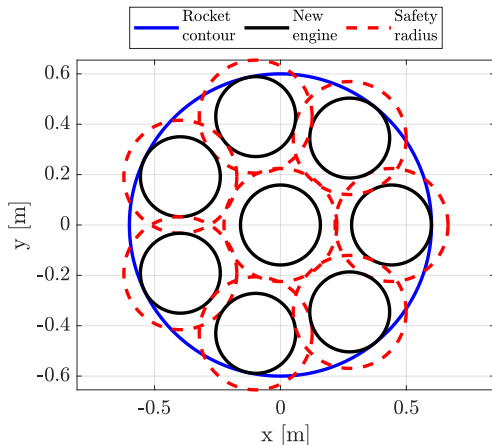


Figure 2.6: New engine configuration

As for regenerative cooling, the most critical sections (combustion chamber and throat, due to the high temperatures) are already working as intended, since the engine is flight proven. The extension is supposed to continue the cooling channels: the temperature absorbed in this latter section will be minimal since the gases are already quite expanded and relatively cold<sup>[9] [1]</sup>.

Oxygen has to be stored at extremely low temperatures ( $90.19\text{ K}$ )<sup>[66]</sup> in order to remain in liquid form and effectively being used as a propellant, so it is necessary to coat the tank containing the oxidizer with an insulating material, whose mass has been computed in Section 2.1.3. However, in the time span between the end of refueling and the ignition of the engines, a certain quantity of LOX will for sure boil off.

The material chosen for the insulation is the polyurethane-based foam NCFI 24-124, similar to the Space Shuttle External Tank's ( $\rho = 38.44\text{ kg/m}^3$ ,  $k = 0.02\text{ W/m}$ )<sup>[67]</sup>, given its wide characterization, availability and heritage.

### 2.2.5.1 Thermal model

In order to model the thermal dynamics of the system, some simplification needed to be implemented: the insulation mass has been estimated through historical regression starting from the tank external surface as  $m_{ins} = 1.123 \cdot S_{LOX} = 36.27\text{ kg}$ <sup>[30]</sup>. Then, through density, the thickness is computed as  $3.2\text{ cm}$ .

As most of thermal dissipation will occur through the external cylindrical wall, the ellipsoidal domes have been from now on neglected. The system is modeled with the technique of thermal resistances: convection between oxygen and the aluminum ( $h = 609\text{ W/m}^2\text{K}$ ), conduction through the aluminum tank wall ( $k = 237\text{ W/mK}$ ) and the foam insulation and convection with external air ( $h = 186\text{ W/m}^2\text{K}$  at cruise condition). These coefficients are better explained in Appendix E.1.2. The LOX is considered at constant temperature  $90\text{K}$  since it is in phase transition and the external air is supposed to be at  $300\text{K}$  (maximum temperature registered at Vandenberg, worst case scenario<sup>[68]</sup>). The global thermal resistance is then  $0.0629\text{ K/W}$ , and, with the given temperatures, there is a constant heat flow of  $3341\text{ W}$ . Assuming that the boiling off happens for 2 hours (for LauncherOne it was 1 hour and 5 minutes<sup>[69]</sup>) and that all the thermal energy goes towards boiling off LOX ( $\lambda_{l,f} = 213\text{ kJ/kg}$ ) the total amount of boiled off LOX is  $112.9\text{ kg}$ , equivalent to  $1.13\%$ .

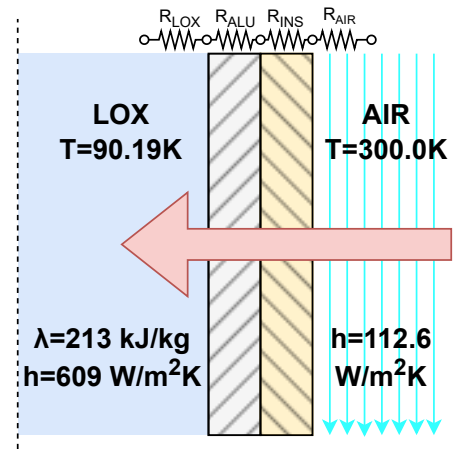


Figure 2.7: Tank thermal scheme

## 2.3 Aerodynamics

The aerodynamics of JEENO is a critical aspect of its design, requiring a balanced compromise among several objectives: maximizing the lift-to-drag ratio (L/D), ensuring controllability throughout the flight envelope, minimizing heat fluxes, and accommodating payload and systems within client imposed time constraints. To reduce development time, LauncherOne's aerodynamic shape was adopted as a baseline, leveraging lessons learned from its development and operational use to advance subsequent design phases.

### 2.3.1 Aerodynamic Model

The aerodynamic model calculates key parameters like the lift coefficient ( $C_L$ ), drag coefficient ( $C_D$ ), and position of the center of pressure ( $x_{cp}$ ), critical for control and performance optimization. Analytical and numerical methods<sup>[5] [70]</sup> were used for Mach numbers below 3, while a panel method was applied for Mach numbers above 3.

#### Lift Coefficient ( $C_L$ ) and Center of Pressure

The lift coefficient ( $C_L$ ) and the center of pressure ( $x_{cp}$ ) are fundamental to the launcher's stability, determining how aerodynamic forces are distributed along the vehicles body. The method<sup>[5]</sup> for calculating these parameters is based on slender-body theory, with adjustments made to account for the tail's aerodynamic effects<sup>[5]</sup> (for more details refer to Appendix D.1).

1. Body Lift Contribution: The lift coefficient of the body is derived using slender-body theory<sup>[71]</sup>, which is well suited for analyzing slender, axisymmetric shapes like the JEENO launcher. This theory accounts for the distribution of pressure forces along the vehicles surface, particularly for cylindrical and conical body sections<sup>[5]</sup>.
2. Tail Contribution: The tails contribution to lift is modeled as a deflection of the flow downstream of the body. This is considered an additional source of lift and is quantified using a simplified interference model that accounts for the tails impact on the flow around the body<sup>[5]</sup>. The contribution from the tail enhances the total lift coefficient, improving the vehicles aerodynamic performance.
3. Center of Pressure: It is a critical parameter for stability, as it must be positioned behind the center of gravity to ensure the launcher remains aerodynamically stable. The center of pressure is calculated by combining the contributions from the body and the tail, resulting in a precise estimate of the launchers stability margin.

#### Drag Coefficient( $C_D$ )

The drag coefficient ( $C_D$ ) is another key aerodynamic parameter that directly affects the launchers performance, particularly in terms of fuel efficiency and flight dynamics. The drag coefficient is calculated using a component build-up method<sup>[70] [72]</sup>, which divides the total drag into three main components: nose drag, skin friction, and base drag (for more details refer to Appendix D.1).

1. Nose Drag ( $C_{D,n}$ ): At subsonic and low supersonic speeds, the nose drag is calculated using empirical relationships that depend on the specific nose geometry (conical, ogival, elliptical). These formulas are based on experimental data and allow for precise drag estimations for different shapes.

At high supersonic speeds, the drag contribution from the nose is estimated using Newtonian impact Theory<sup>[73]</sup>, which approximates the pressure distribution on the vehicles nose. This model provides a good approximation for supersonic flow conditions.

2. Skin Friction Drag ( $C_{D,friction}$ ): The skin friction is determined using boundary layer theory, which calculates the frictional forces due to the interaction of the flow with the surface of the body<sup>[74]</sup>. The Van Driest method<sup>[74]</sup> is used to estimate the skin friction coefficient, since it provides accurate results for both laminar and turbulent flow conditions.

3. Base Drag ( $C_{D,base}$ ): The contribution from base pressure is calculated using well-established empirical relations for blunt bodies, particularly for cylindrical afterbodies at supersonic Mach numbers<sup>[75]</sup>. The drag from this component is important at high speeds, where flow separation plays a significant role.

### Methodology and assumptions

The following assumptions were made to simplify the calculations and ensure their applicability across different flight regimes:

1. For  $C_L$  and  $x_{cp}$ <sup>[5]</sup>:

- Small angles of attack: The method assumes that the launcher operates within a linear aerodynamic regime, where lift and moment coefficients are directly proportional to the AoA.
- Symmetry: The launcher is considered an axisymmetric structure, simplifying the calculation of the aerodynamic forces and moments.
- Linear superposition: The contributions from the body and tail to the lift are treated as additive.
- Negligible induced effects: Only primary contributions from body and tail are accounted for, neglecting secondary interactions like flow separation or wake effects.

2. For  $C_D$ <sup>[70][72]</sup>:

- Turbulent Boundary Layers: The flow over the vehicle is assumed to transition from laminar to turbulent, with fully turbulent conditions prevailing for most of the flight.
- Empirical corrections: Drag coefficients for specific geometries are refined using experimental data, ensuring the method's relevance for real-world configurations.
- Mach Number Regimes: Separate drag models are employed for subsonic, transonic, and supersonic regimes, each capturing the distinct flow characteristics at different flight speeds.

### Validation of the Model

The results for both the lift coefficient ( $C_L$ ) and the drag coefficient ( $C_D$ ) were validated using specialized aerodynamic simulation softwares, such as **RasAero**<sup>[76]</sup> and **OpenRocket**<sup>[77]</sup>. These tools provided numerical results that were compared with the analytical predictions, ensuring the accuracy of the model.

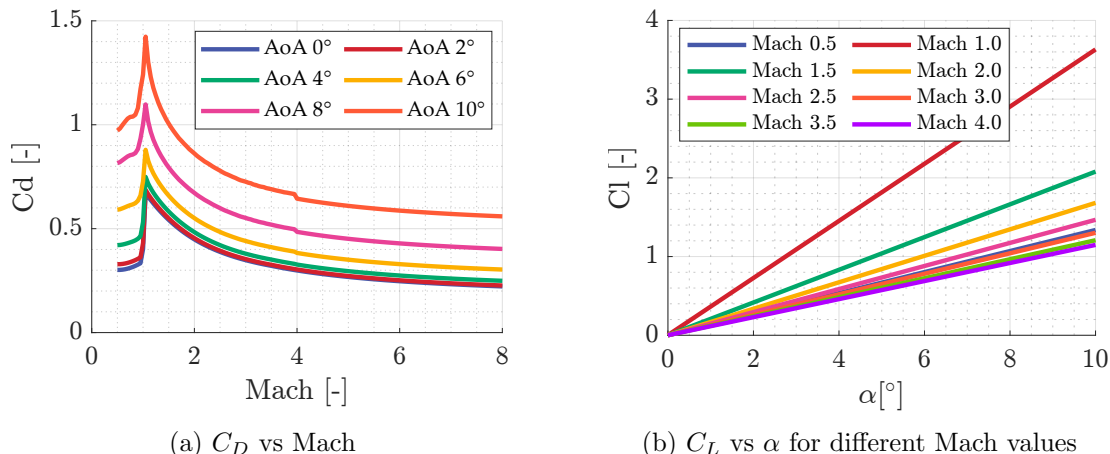


Figure 2.8:  $C_D$  and  $C_L$  for the JEENO launcher

#### 2.3.2 Panel Method Algorithm for Aerodynamic Analysis

The panel method algorithm provides a numerical approach to estimating aerodynamic coefficients ( $C_l$  and  $C_d$ ) of axisymmetric bodies. The main objective behind developing this script is to optimize

the nose geometry, excluding the effect of tail fins. The method assumes steady, inviscid, compressible flow and utilizes Newtonian and modified Newtonian theories for high-Mach regimes<sup>[78]</sup>.

### Algorithm Overview

The key steps of the algorithm are as follows:

1. **Geometry Discretization:** The axisymmetric rocket geometry is divided into longitudinal segments, each described by parametric functions for radius and axial length. These segments are discretized into panels along both the longitudinal ( $x$ ) and azimuthal ( $\theta$ ) directions. Panel coordinates and normals are computed to approximate the surface geometry.
2. **Flow Assumptions:** Free-stream properties are derived using the International Standard Atmosphere (ISA) model for a given altitude. The Mach number defines the flow regime, and dynamic pressure is calculated accordingly.
3. **Newtonian Aerodynamics:**
  - *Newtonian Method:* Assumes pressure distribution proportional to the sine-squared of the angle ( $\beta$ ) between the free-stream direction and panel normals<sup>[78]</sup>.
  - *Modified Newtonian Method:* Accounts for shock effects by scaling the pressure coefficient ( $C_p$ ) to a maximum value based on post-shock conditions<sup>[78]</sup>.

Forces on individual panels are summed to determine the total axial and normal forces.

4. **Aerodynamic Coefficients:** The total aerodynamic forces are resolved into lift and drag components using wind-axis transformations. The coefficients of lift ( $C_L$ ) and drag ( $C_D$ ) are non-dimensionalized by the reference area.

The method was validated against semi-empirical models, excluding the effects of tail fins. The final nose geometry selected was a conical ogive, chosen for its ability to accommodate varying payload volumes and reduce drag at high velocities.

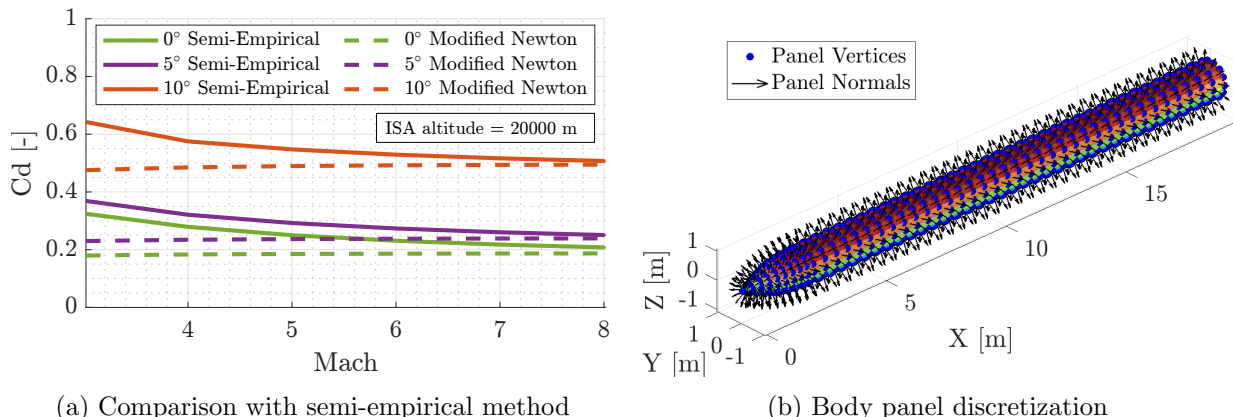


Figure 2.9: Paneling Results

### 2.3.3 Stability analysis

The stability analysis of JEENO aimed at ensuring both safe, stable flight and optimized aerodynamic performance ( $C_l/C_d$ ). This involved evaluating the lift coefficient required for the pitch-up maneuver, managing the center of pressure ( $C_p$ ) in relation to the center of gravity ( $C_G$ ), and assessing the impact of various fin configurations. Both canard and winged designs were considered, with the canard option ultimately rejected due to its higher cost, which reduced the return on investment (ROI), and added mass to the second stage. The winged configuration was discarded

early on as it was incompatible with the aircraft launch platform, blocking the use of the carriers fifth under-wing store. The final design incorporates four tail fins, providing the necessary stability during release from the aircraft and ensuring adequate separation. These fins feature movable surfaces for enhanced control during the flight.

The rocket was designed to remain stable upon release from the carrier, primarily for safety. After sufficient separation from the carrier and engine ignition, the tail fins movable surfaces are actuated to control the rockets attitude and guide it along the intended trajectory. These surfaces generate the aerodynamic moments necessary to perform the pitch-up maneuver effectively.

### 2.3.3.1 Fins Geometry

The fin geometry was finalized after several iterations in conjunction with mission analysis. The optimal total surface area was determined to be  $1\text{ m}^2$ . To ensure consistent lift coefficient contributions throughout the flight, the configuration was fixed with four fins mounted at zero inclination relative to the longitudinal axis. The design was also verified to fit within the available space beneath the carrier's wing, ensuring compatibility with the launch platform.

## 2.4 Mission Analysis

The Mission Analysis department is in charge of merging all the properties of JEENO, in order to simulate the full trajectories and validate the results.

### 2.4.1 Phases of the mission

The full flight of JEENO is divided in different phases: free-fall from the carrier, powered ascent, stage separation, powered ascent of second stage, unpowered ascent and final burn for orbit insertion. In Figure 2.10, all phases of the mission are illustrated to provide a better understanding of how the various configurations of JEENO are evaluated. The lines labeled "ENGINE STATUS & TVC" and "FIN CONFIGURATION" indicate engine activity and the rocket's stability, respectively. Green rectangles denote active engines and a stable configuration, while red rectangles represent inactive engines and an unstable configuration. Obviously, the TVC is enabled together with the engine. Note that fins and their control are not necessary on the second stage since air density is extremely low, thus they were not implemented.

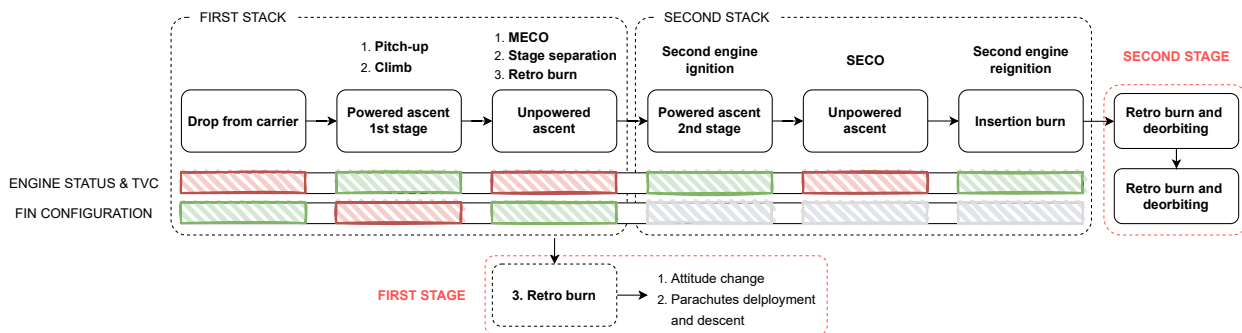


Figure 2.10: CONOPS for MSA simulator

The unstable configuration is needed in some phases, since JEENO responds more effectively to TVC; otherwise it would be very difficult to control its attitude and perform tasks such as the pitch-up maneuver. On the contrary, a stable configuration is required to maintain the rocket's unperturbed state when the TVC is not available.

The trajectory is logically divided into different phases and the flight mechanics simulate all the important steps. It begins with the un-powered drop of the launcher from the aircraft: JEENO falls for 5 seconds in a stable configuration before the main engines ignite at 100% throttle with

active TVC, starting its trajectory toward the final orbit. During this part of the flight, the Max-Q condition is surpassed without a throttle-down, as this approach showed no significant reduction on Max-Q. Then, the first stage burns its propellant and shuts down: few seconds are waited and staging is performed. The second-stage engine ignites a few seconds later, after the first stage has used its reserved propellant for a retro-burn. Now, the first stage performs a re-orientation (near its apogee) to aligns with the right attitude, ready for the parachute opening as explained in section 2.5.

The second stage, meanwhile, continues its ascent, with fairing jettison at 110 km and shutting down its engine once the apogee is predicted to approach 400 km. A small unpowered ascent starts here and stops only when, reached 400 km, the engine reignites for an attitude change to align the  $i$  body axis to the  $X$  axis of the rotating frame, described in subsubsection 2.4.2.2. The engine burns with a horizontal attitude until the desired velocity at the apogee is met.

At this point, reached both final altitude and velocity, the payload is inserted into orbit. Then, retro-burn is performed to separate from the payload and execute the de-orbiting maneuver, pointing in the negative direction of the trajectory to avoid engine wash effects on the payload.

## 2.4.2 Simulator

The simulator is a three degrees of freedom trajectory propagator that is able to compute the trajectories regarding all the phases of the flight. This 3-DOF model incorporates a rigid body bi-dimensional dynamics with two axis translations (namely "x" and "z") combined with a rigid rotation. The model relies on a fixed ECI frame and a rotating one (in order to be able to account for the spherical Earth model).

The structure of the simulator is very simple: an ODE solver propagates the controlled states using a function that incorporates EOM and all the physical models of the other subsystems.

### 2.4.2.1 Controlled parameters

The full state that is propagated in time is a vector composed by the 2 positions (horizontal and vertical), their respective derivatives, the body rotation, angular velocity and the fuel mass  $[x, z, v_x, v_z, \theta, \dot{\theta}, m_{prop}]$ . The system of ODE to be integrated in time involves a forces and moments balance, further explained in subsubsection 2.4.2.2.

### 2.4.2.2 Equations of motion

The accelerations are derived by a forces and moment equilibrium, involving vertical force, horizontal force and total moment.

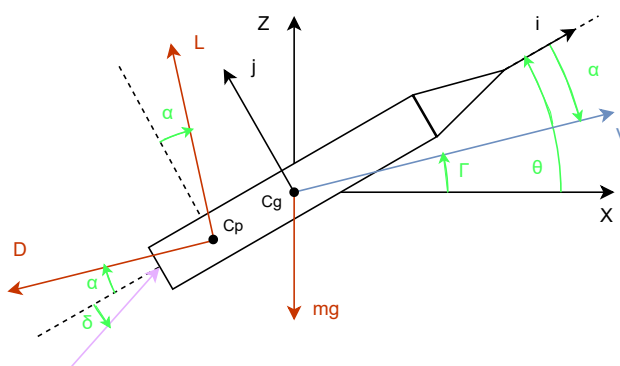


Figure 2.11: Dynamic model of the rocket

As can be seen in Figure 2.11, the forces acting on the rockets are lift ( $L$ ), drag ( $D$ ), thrust ( $T$ ) and mass forces. The angles are described as depicted in the figure:  $\alpha$  is the Angle of attack (AoA),  $\Gamma$  is the flight path angle and  $\theta$  is the pitch angle.

All these forces are described in body frame ( $i$  and  $j$  axis) and then rotated in the ECI frame ( $x$  and  $z$  axis) with the appropriate DCM. The simulator relies on the ECI reference system to propagate the states, but a "rotating ECI" is used to define the orientation of JEENO with respect to the local horizon. The  $\beta$  angle defines this rotation in the new frame and the angles are adjusted accordingly.

#### 2.4.2.3 Dynamic properties

The simulator incorporates all the departments working on JEENO: multiple parameters are variable during flight and most of them significantly impact on the physics during the simulation. The functions used to derive the physical characteristics are used to generate multiple-dimension matrices, then interpolated during the simulation in order to lower the computational time.

The functions used and the relative details are listed:

- **STR:** Center of mass and inertia moment, depending on the simulated stage and the propellant mass remaining
- **AER:** Center of pressure,  $C_d$  and  $C_l$ , varying altitude, mach number and angle of attack
- **PRP:** Thrust profile and  $\dot{m}_{prop}$ , changing throttling and altitude
- **RCS:** Altitude and  $C_d$  of parachutes
- **Other:**  $T_h$ ,  $p_h$ ,  $\rho_h$  and  $a_h$  from Matlab<sup>[79]</sup> built-in function "computeAtmosphericData"

#### 2.4.2.4 Navigation

The rocket needs to be controlled in order to perform an orbit insertion: the propulsion department enabled thrust vectoring control and throttling for both first and second stage engines.

The thrust vector angle  $\delta$  is controlled via a PID controller that drives to zero the error between the local horizon direction and the required pitch angle. This angle is interpolated from a "pitch-program" curve that starts from a chosen angle (one of the free parameters for the optimization) and goes to zero with a chosen slope grade (last free parameter, ranging from 1st order to 3rd order). These angles are then interpolated with respect to the vertical position.

The trajectory shall be able to exploit Lift and starting horizontal velocity; the pitch program is likely to have a strong angle at the beginning of the mission and a zero angle in apogee.

#### 2.4.2.5 Optimization

The optimization techniques studied so far proved to be quite ineffective since the problem is highly non linear and the computational times are not negligible. A new strategy was adopted, dividing the problem in 2 different steps in a way to optimize separately altitude and velocity of the orbit insertion. In both cases a bisection-like method was implemented.

This simple implementation is viable since the horizontal velocity can be manipulated by imposing  $\Delta V$  in the tangential direction: this way, the apogee altitude is preserved.

The parameters that can be tuned for this procedure are related to the pitch program and to the initial altitude for the last tangential burn.

#### 2.4.3 Launch position

The objective to reach a 98° SSO orbit requires us to launch above the Pacific Ocean to comply with international regulations<sup>[80]</sup>, hence two possible launch sites are selected: Mojave Air and Space Port and Vandenberg Space Force Base.

The second one is a military base, but hosts also various commercial launches, e.g. Falcon 9<sup>[81]</sup> and Pegasus XL<sup>[82]</sup>. The launcher detachment is scheduled to be along the expected orbit projection at a distance of about 450 km from the nearest shore line and about 490 km from the *Vandenberg Space Force Base* and 600 km from the *Mojave Air and Space Port*. This is clearly within the admissible aircraft carrier range and allows for holding patterns in case of holds during launch procedures.

#### 2.4.4 Monte Carlo Analysis

A Monte Carlo analysis is performed to verify the insertion accuracy of the launcher.

The following parameters are changed considering a Gaussian distribution:

- $T\%$ : Thrust percentage, centered in 100%, with a 10% deviation at  $3\sigma$ <sup>[83]</sup>
- $M_p\%$ : Propellant mass percentage, centered in 100%, with a 5% deviation at  $3\sigma$ <sup>[84]</sup>
- $[CD\%, CL\%]$ : Aerodynamic coefficients percentage, centered in 100%, with a 10% deviation at  $1\sigma$ .
- $[h_{0,off}, h_{1,off}, h_{2,off}]$ : Offset on the opening altitude of the three recovery system phases, centered in 0, with a [1000, 500, 200] m deviation at  $3\sigma$ .

The initial position and velocity are not considered as varying parameters, given the capacity of the carrier to guarantee precision in the order of less than 1%.

A sample size of 500 is chosen to reduce the computational load, while still providing satisfying results in terms of convergence: as it can be seen in Figure 2.12, both the cumulative mean and the cumulative standard deviation of the reached orbit radius stabilize after just 350 simulations for the mean and 200 for the standard deviation.

## 2.5 Recovery system and re-entry analysis

This section outlines the design of the first-stage recovery system and analyzes the main concerns in the re-entry phase of both stages.

For the first stage, after the staging an apogee of 165 km is reached. Later, a re-orientation maneuver is performed in order to orient the engines downward and to ensure an engines-first entry<sup>[85]</sup>. The second stage, performs a de-orbiting maneuver after releasing the payload, in order to autonomously re-enter.

### 2.5.1 Recovery system architecture

The role of the recovery system is to ensure a safe touchdown and to avoid any critical damage to the structure. For this mission, the primary challenges are the high velocities, which cause significant opening shocks, and thermal loads.

As shown in Table 1.2, the touchdown velocity is constrained to be less than 15 m/s, considering a splashdown recovery, but in the design it is set to 13 m/s to have a safe margin on the constraint. Starting with this target velocity and the recovered mass, the required parachute area was calculated. Dimensions of other system elements were designed to manage opening shocks and thermal loads during re-entry. The recovery system architecture is schematically represented in Figure 2.13 and the design procedure is described hereafter.

#### 2.5.1.1 Ballute design

The first deployed component is a ballute system, which decelerates and stabilizes the vehicle from speeds and altitudes that exceed the capabilities of traditional decelerators. In fact, ballutes are lightweight, compact, reliable, and resistant to high aerodynamic heating.<sup>[86]</sup>

As shown in Figure 2.14, the ballute deploys at 60 km altitude, slightly below the threshold where ram-air inflation becomes unfeasible due to low density<sup>[3]</sup>; otherwise, supplemental inflation devices should be addressed<sup>[3]</sup>. At the same time, deploying at lower altitude would increase the velocity at which the denser air is reached, and thus the heat flux, risking structural integrity.

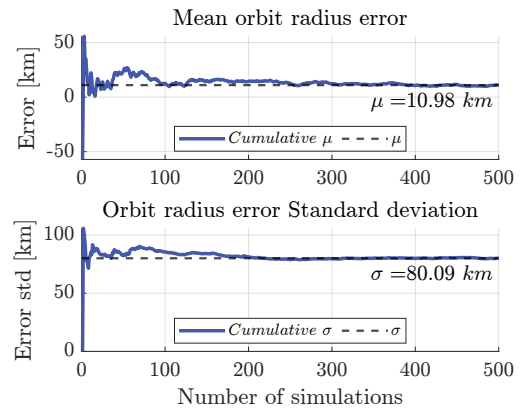


Figure 2.12: Orbit radius error mean and standard deviation

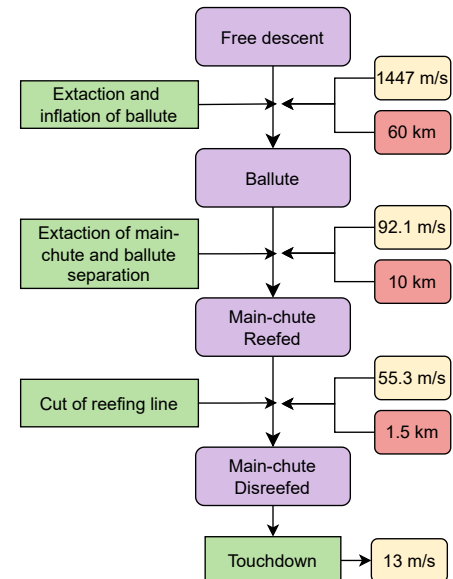


Figure 2.13: Recovery architecture

Therefore, ballute material selection is particularly critical; the choice is usually woven fabric, mainly composed of Nomex, thanks to its high heat resistance up to operational temperatures of 640 K<sup>[3,87]</sup>.

The ballute geometry is based on reference designs from literature<sup>[87]</sup>: it features 16 gores, 16 suspension lines and a burble fence measuring approximately 10% of the equatorial diameter. Inflation occurs thanks to four ports diametrically located on the envelope periphery. The ballute surface area is 20 m<sup>2</sup>, sufficient to slow down the stage and reduce thermal loads.

Once the ballute arrives at the designated altitude for the main parachute deployment, it is detached from the launcher to avoid destabilizing the main-chute descent. As a single-use component, the ballute is the only expendable element in the recovery system.

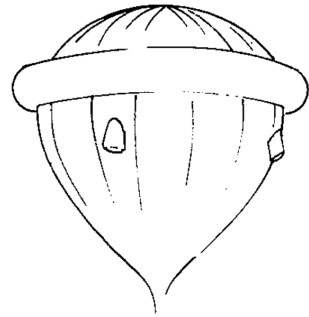


Figure 2.14: Ballute<sup>[3]</sup>

### 2.5.1.2 Main parachute design

After the detachment of the ballute, the main parachute is deployed in a reefed condition. Among all the possible designs, a ring-sail parachute was chosen, choice supported by its proven reliability in past missions, such as the Mercury, Gemini, and Apollo missions<sup>[4]</sup>. The drag coefficient  $C_{d0}$  of the fully opened canopy was assumed to 0.8<sup>[4,88]</sup>, requiring a total area of 190 m<sup>2</sup> to achieve a splashdown velocity of 13 m/s. The percentage of reefed canopy was selected in order to have feasible opening loads, computed with the procedure explained in 2.5.2. It results in a reefed surface equal to 35% of the total disreefed canopy surface and an effective  $C_{d0}$  of 0.5 during this phase<sup>[4]</sup>.

The next step involved determining the number of suspension lines to support the opening phase and the design of the reefing line. Based on similar conditions presented in<sup>[88]</sup>, the parachute was designed with 40 gores, necessitating 40 suspension lines. The recommended material for these lines is a 550 lb Nylon cord (249.5 kg)<sup>[88]</sup>, resulting in a total load capacity of 98 kN, almost twice the expected forces during reefed opening (57 kN) and disreefing (51 kN).

For the reefing line,<sup>[4]</sup> estimates that the radial force is approximately 3% of the opening shocks in the reefed stage, but a safety factor of 2.5 is anyway recommended; thus, a 4.3 kN capacity must be considered. Following recommendations in<sup>[88]</sup>, a 1000 lb (4.4 kN) braided nylon cord is selected.

In Table 2.10 the results of the design phase of the recovery system are shown.

Parachute	Design surface	Drag coefficient	N. of gores and lines
Ballute	20.0 m <sup>2</sup>	0.6 <sup>[3]</sup>	16
Main: reefed stage	66.5 m <sup>2</sup>	0.5	40
Main: disreefing stage	190.0 m <sup>2</sup>	0.8	

Table 2.10: Recovery System design parameters

### 2.5.2 Opening Shocks model

Due to the lack of analytical models in literature for ballute opening forces, no direct derivation was possible. According to<sup>[87]</sup>, the ballute's opening shock is comparable to the drag force exerted during descent, making it negligible relative to other opening shocks.

To model the opening shocks of both for the reefed main opening and the disreefing, the Pflanz method was implemented following the description in<sup>[4]</sup>. An accurate description of the method can be found in C.1, while its main passages are summarized here.

The method calculates the force reduction factor  $X$ , which depends on various parachute design parameters and deployment conditions, primarily air density and velocity. This factor is determined by interpolating experimental data using the dimensionless ballistic parameter  $A$ , defined as:

$$A = \frac{2m}{(C_{DS})_p g \rho V t_f} \quad (2.2)$$

where:  $m$  is the recovered mass,  $(C_{DS})_p$  the parachute projected drag area,  $\rho$  the air density at inflation altitude,  $V$  the velocity at line stretch or start of disreef.  $t_f$  is the filling factor or inflation time, computed as explained in C.1 and equal to 0.7 s for the reefed opening and 0.23 s for the disreefing. The opening force is then computed with 2.3, where  $(C_{DS})_p$  is the drag area and  $q_1$  the dynamic pressure at the instant before inflation.

$$F_p = (C_{DS})_p q_1 X_1 \quad (2.3)$$

This method leads to 57001.49 N for the reefed opening and 51093.86 N for the disreefing. These results align with literature values, such as the Electron recovery system, experiencing forces of around 60 kN each opening stage<sup>[85]</sup>. In general, the parachute opening shocks were designed to correspond to a maximum deceleration of 4.5 g,<sup>[89]</sup> and this criterion is respected in our case.

### 2.5.3 Heat-flux model

Since the most critical aspect in the re-entry phase is the thermal loads due to atmosphere, a preliminary heat flux estimation was performed in order to assess its recoverability of both stages. An accurate evaluation of the aerodynamic heating requires CFDs and accurate geometry model. But, being a preliminary analysis some assumptions can be made.

The evolution of temperature in time was evaluated computing the net heat flux acting on the body at re-entry, considering the incoming aerodynamic heating and the radiation between body and atmosphere, and neglecting incoming radiation from the Sun<sup>[90]</sup>. The equations used were 2.4 and 2.5, where  $S_{norm}$  is the surface perpendicular to wind,  $\epsilon_{mat}$  is the emissivity of Aluminum 2219<sup>[45]</sup> for the first stage analysis and of Carbon<sup>[46]</sup> for the second stage.

$$\dot{Q}_{Aer} = \frac{1}{2} \rho V^3 S_{norm} \quad (2.4) \quad \dot{Q}_{Space} = \sigma_{SB} \epsilon_{mat} (T^4 - T_A^4) S_{tot} \quad (2.5)$$

Then, through an energy balance, it was possible to retrieve the heat flux integrating in time Equation 2.6, where  $m$  and  $C_p$  are mass and specific heat capacity of the stage.

$$\dot{T}_{stage} = \frac{\dot{Q}_{Aer} - \dot{Q}_{Space}}{m C_p} \quad (2.6)$$

In 3.1.1.1, the results of this preliminary thermal analysis are discussed, for both stages.

### 2.5.4 Ocean Recovery and Location

For safety reasons, ocean recovery is suggested, even if it leads to additional costs. In particular, corrosion of structural part must be avoided with correct cleaning and usage of corrosion resistant materials. Also for this reason, in subsection 2.1.5, Al 2219 was selected for first stage. In literature, the case of the Electron recovery is taken as reference, as for its splashdown recoveries waterproofing features were adopted, improving sealing solutions for the interstage, powerpack and some internal components on the Rutherford engines to protect its key components from the environment of an ocean splashdown<sup>[9]</sup>. If similar precautions are followed, a minimal refurbishment is necessary<sup>[91]</sup>.

From the Monte Carlo analysis carried out in subsection 2.4.4, the resulting position of the recovery of first stage was retrieved also accounting for uncertainties and is displayed in Figure 2.15. The yellow x represents the nominal splashdown position, while the red line is possible position outcome from the Monte Carlo analysis. Anyway, all the considered cases are located in a non-populated and island-free Pacific Ocean area.

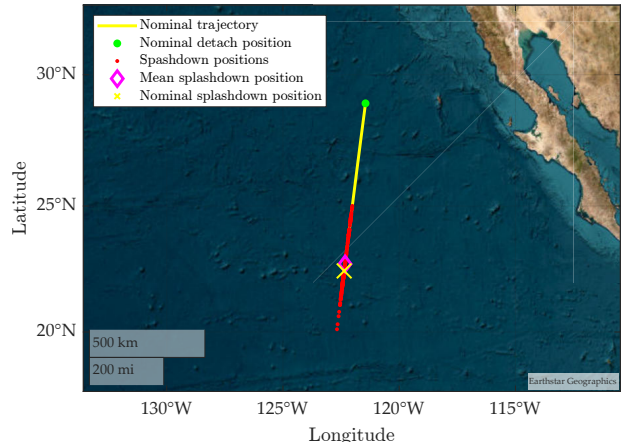


Figure 2.15: First stage splashdown positions

### 3. Results and Conclusions

#### 3.1 Development results

The end product of this conceptual design is an airborne launch vehicle with constant diameter. The first stage is realized in Aluminum Alloy 2219 and is powered by eight engines. The second stage, made from carbon fibers, is propelled by a single engine. The payload is stored in the fairing, whose length is determined by the maximum payload mass constraint of 400 kg.

A graphical representation of the launcher is shown in Figure 3.16 with the lengths of each section detailed in Table 3.11. The component allocation was based on empirical correlations from the literature and adapted for the case of common domes<sup>[1]</sup>. The configuration of the tanks was chosen to ensure stability at launch while maintaining a small stability margin for better controllability with movable fins, leading to the placement of the oxidizer tank aft of the fuel tank. Furthermore, the interstage accommodates both the nozzle of the second stage engine and the upper dome of the fuel tank. The parachutes are also housed in the interstage to an easy deployment. Lastly, a conical nose is utilized, as it is simpler to develop and more efficient at higher Mach numbers.

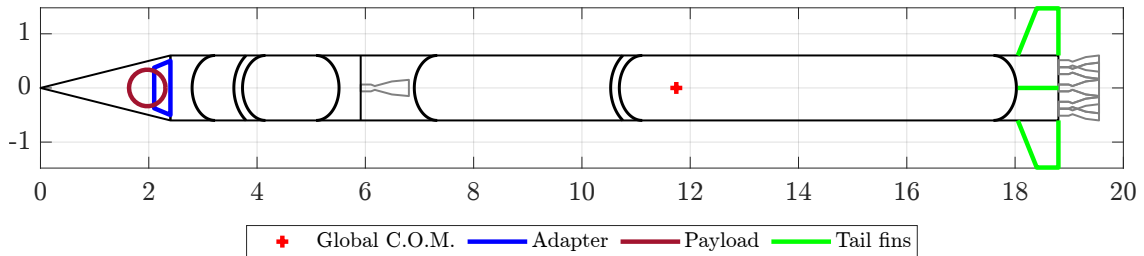


Figure 3.16: Final rocket shape

Stage	Fairing	Fwd Skirt	Fuel Tank	Common Dome	Ox. Tank	Aft Skirt
2 <sup>nd</sup>	2.40	0.82	0.77	0.16 <sup>[1]</sup>	0.93	0.82
Interstage	Fuel Tank	Common Dome		Ox. Tank	Aft Skirt	Engine
1 <sup>st</sup>	1.41	3.63	0.16 <sup>[1]</sup>	6.49	1.20	0.75

Table 3.11: Length of launcher's components in [m]

The final mass distribution, obtained as explained in subsection 2.1.3, is summarized in Table 3.12. This describes the state of the vehicle at launch with all the propellant loaded.

Stage	Skirts	Tanks	Fins	Propellant	Avionics	Payload	LVA
1 <sup>st</sup>	153.7	615.2	249.4	11468	15.0		
2 <sup>nd</sup>	30.7	64.1	-	2439.2	60.0	250.0	68.9
	Recovery	Engines	Wiring	Thrust struct.	LOX insulation	Fairing	Stack
1 <sup>st</sup>	112.3	320.0	21.1	55.9	30		1 <sup>st</sup> 16053
2 <sup>nd</sup>	-	45.0	6.8	7.9	6.3	29.1	2 <sup>nd</sup> 2981

Table 3.12: Mass distribution in [kg] for each stage

Lastly, the main characterizing parameters are reported in Table 3.13. The *structural mass indexes* are different from the values of the baseline: this is expected, as the materials of the two stages have different mechanical properties (subsection 2.1.5), and because the first stage mounts additional mass due to the fins system, and of the fairing (subsection 2.1.3), which is considered as inert mass of the first stage. A similar consideration can be done for the finesse ratio, which has slightly increased with respect to the one obtained from the interpolation of the baseline. This change reflects the requirements for recoverability and the need to ensure the structure fits within the volume constraints of the carrier.

Stage	$\epsilon_s$ [-]	$I_s$ [s]	Th [kN]	$I_{tot}$ [m]	D [m]	$I_{tot}/D$ [-]
1 <sup>st</sup>	0.123	324.5	219.2			
2 <sup>nd</sup>	0.084	343.0	31.0	19.6	1.2	16.3

Table 3.13: Main parameters

### 3.1.1 Trajectory results

JEENO has demonstrated the capability to bring a 250 kg payload to a 400 km orbit with a nominal accuracy of  $\sim 58$  m on the required altitude and  $\sim 3$  m/s on the required velocity.

	MECO	Stage separation	SECO	Ballute opening	Reefed ringsail	Horizontal burn	SECO	Disreefing of ringsail
Altitude [km]	76.6809	80.5832	323.6642	60	10	399.7520	399.9597	1.5
Time [s]	174.3345	177.2991	427.669	515.3127	643.6552	668.1856	705.8856	850.5395

Table 3.14: Flight events

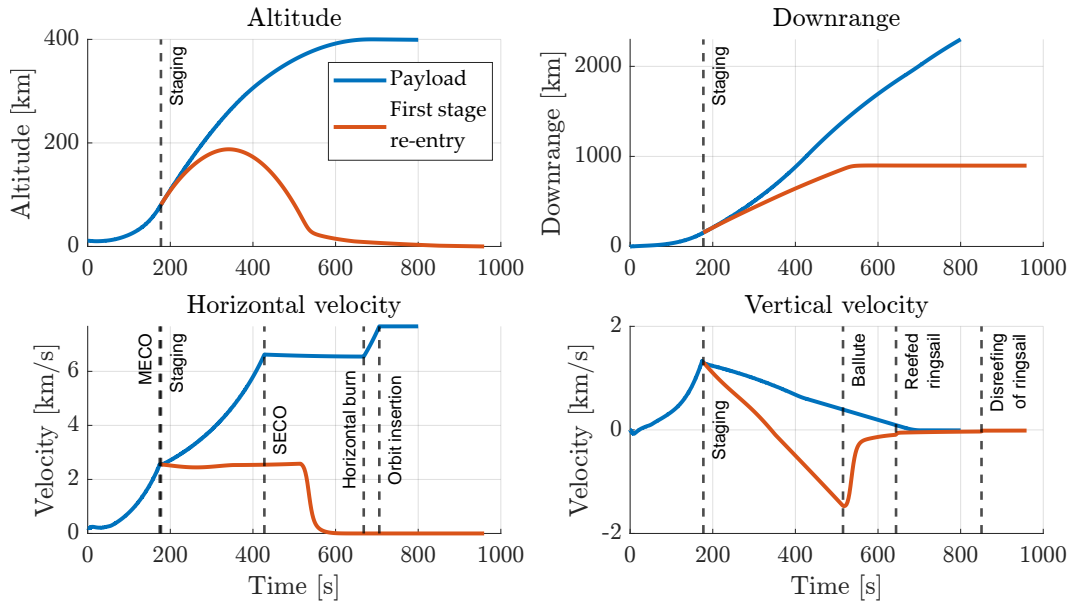


Figure 3.17: Simulator positions and velocities

In Figure 3.17 are depicted vertical and horizontal positions and velocities, in the rotating reference frame described in section 2.4. All the main phases explained in section 2.4 are visible in the graphs and are summarized in Table 3.14.

The pitch-up maneuver is visible in the first seconds both in the horizontal and vertical velocities; after the first ascent phase, MECO occurs and then staging is detectable. From now on the two stages continue separately: the first one keeps an almost constant horizontal velocity until the first parachute is opened. Then, the deployment of the ringsail-chute and the disreefing occur leading to the designed vertical velocity at touchdown. Simultaneously, the payload continues the ascent; SECO is clearly detectable, with the following unpowered ascent characterized by constant horizontal velocity. Reached 400 km altitude, horizontal burn occurs, represented by the sudden increase in horizontal velocity and zero vertical velocity.

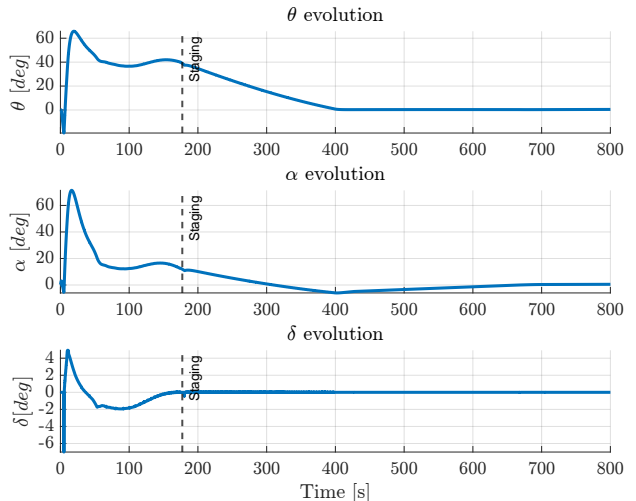


Figure 3.18: Trajectory angles

In Figure 3.18 all the angles described in section 2.4 can be seen.  $\theta$  is following the desired angle (defined with the getPitch curve), while  $\alpha$  represent the AoA. These angles are more than  $60^\circ$  for a brief amount of time, since the initial drop from the airplane is affecting the vertical velocity and a rapid increment of vertical velocity is needed.  $\delta$ , which is causing changes in  $\theta$  and  $\alpha$ , is saturated in the initial part of the flight and it corresponds to the high pitch angle. After this event, it never surpass the maximum gimbal angle of  $7^\circ$ .

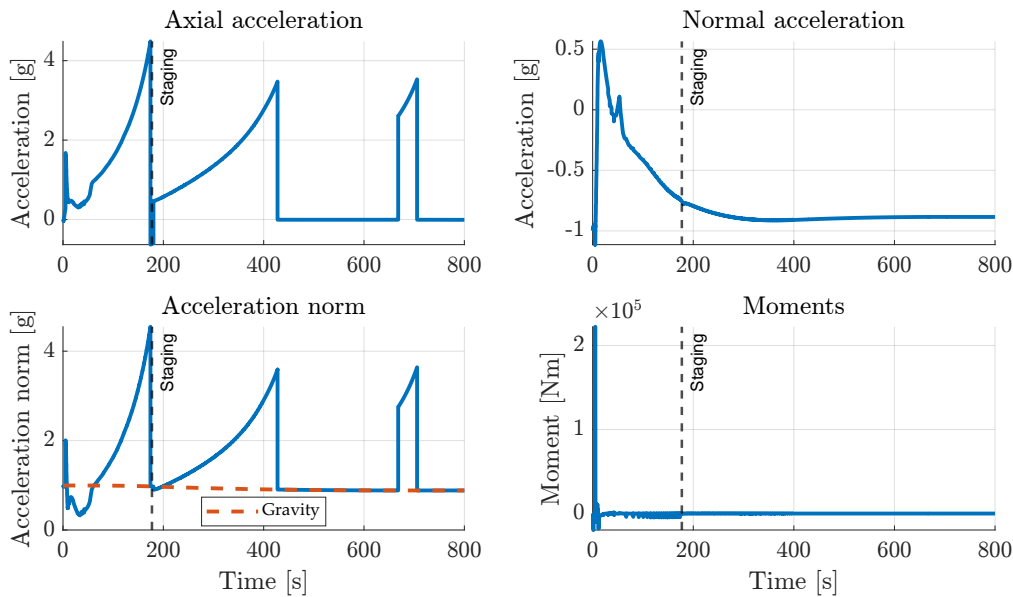


Figure 3.19: Simulator acceleration plots - payload point of view

In Figure 3.19 it can be observed the conservative nature of the assumptions made in subsection 2.1.4: the moments do not exceed the maximum sizing loads, and the axial acceleration stays below the limits, thus confirming the conservative nature of the assumptions made in subsection 2.1.4. This further validates the structural design approach both in terms of loads and FoS. Another validation of the assumptions can be found in section B.6 (Figure B.7), where it is shown the margin on the bending moments for the two stages during the flight.

The acceleration peaks align with the mission phases described in subsection 2.4.1. When the engines are inactive, the vehicle's acceleration matches gravitational one. During the second stage engine firing, the magnitude of the second acceleration is not coincident with the peak of the first one due to the difference in throttling at the re ignition.

The normal acceleration shows how the value tends to the gravity acceleration. This is right from the simulator point of view, where the acceleration is propagated to ensure a proper trajectory.

The moment plot shows a maximum corresponding to the pitch-up maneuver, which is also reflected in the peak of normal acceleration. During the first stage firing, the moment exhibits oscillations caused by the effects of the TVC, as the pitch program adjusts to follow the prescribed angle. In contrast, during the second stage firing, changes in the moment due to TVC are not discernible in Figure 3.19 because of the relatively low TVC, as described in subsection 2.4.1. Lastly, the retroburn acceleration and its associated moment are not evident in Figure 3.19 due to their relatively low amplitudes.

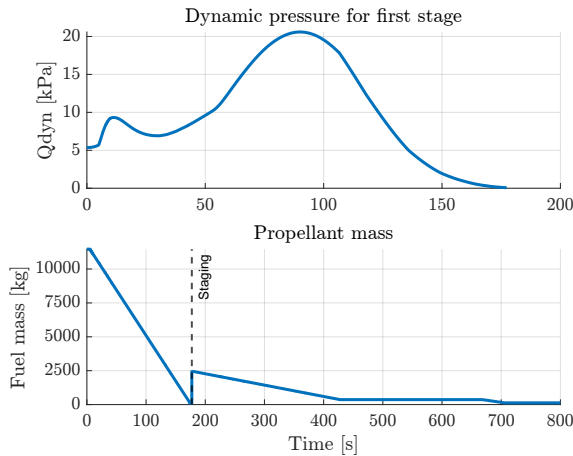


Figure 3.20:  $Q_{dyn}$  and  $m_{prop}$

clearly seen: the first is the full ascension of the first stage, while the second and the third ones happen, respectively, right after staging and at orbit insertion to circularize the orbit. For both the stages, there is a residual mass of fuel at the end of the maneuvers, useful to boost back the first stage and deorbit the second one.

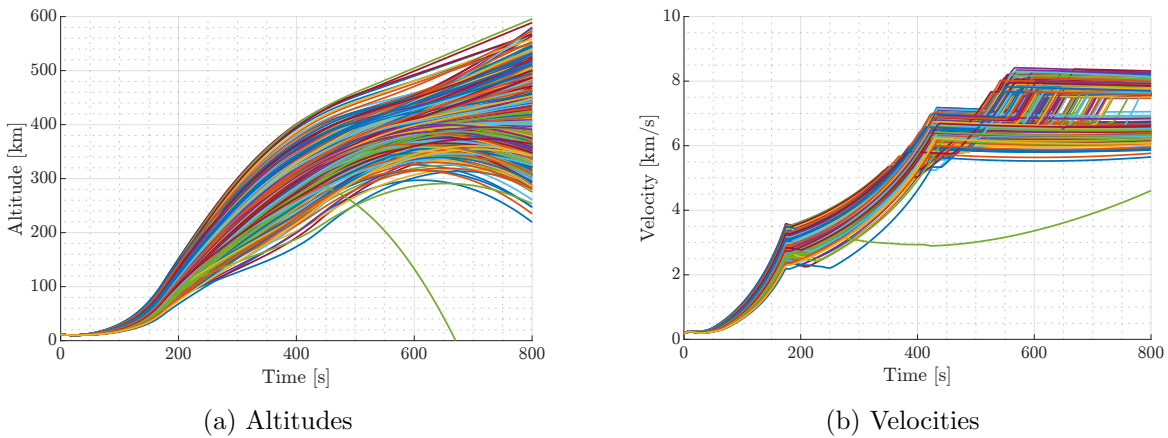


Figure 3.21: Monte Carlo analysis

The uncertainty analysis performed provided mixed results: as it can be seen in Figure 2.12, while the mean error is  $\sim 10$  [km], the standard deviation converges to  $\sim 80$  km. This can also be seen in Section 3.1.1, where the high standard deviation found is reflected in the significant spread of the final reached altitude. Moreover, an outlier can be found; this is due to the combination of a few extreme values in the varying parameters that prevents reaching orbit: lowest possible thrust, combined with higher mass and higher drag coefficient.

Regarding velocities, the cases where the propellant mass is lower than nominal result in a final velocity lower than the necessary one. This is due to the fact that the final orbit insertion maneuver cannot be fully performed. On the other hand, the cases where the final velocity is higher than necessary are a result of a poorly performed injection maneuver: a robust controller is needed to handle all the variabilities given by non-nominalities in the preceding flight phases.

### 3.1.1.1 Recoverability assessment

To assess the recoverability of the two stages, the results of the thermal analysis is shown in Figure 3.22 for both first and second stage. Despite the very simple analysis, some consideration on the recoverability can be done.

The recoverability of the first stage is achievable with appropriate precautions. The temperature peak is estimated at 754 K, while the melting point of Aluminum 2219 ranges from 816 K to 916 K<sup>[45]</sup>. This indicates that recovery is feasible, but thermal protection systems must be implemented, especially considering that this is a preliminary average peak temperature, and significantly higher temperatures may occur locally. It is worth pointing out that these results account only for structural integrity of the stage, but do not characterize the ballute components, as its reliability was assumed from literature<sup>[87]</sup>. The thermal simulation for the second stage, considering a similar recovery system of the first one, shows immediately a much higher peak than the first stage, as the velocity at reentry is higher. Even increasing the parachutes area, it was not possible to significantly decrease the temperature. For this reason, the recoverability of the second stage was excluded. Its deorbiting was anyway assured in accordance to debris mitigation laws<sup>[92]</sup>.

### 3.1.2 Analysis with 400 kg payload

Increasing the payload to 400kg while maintaining the same exact launcher configuration, in optimal conditions leads to a successful reach of the same 400km SSO orbit studied in detail previously. Unfortunately the additional propellant mass needed to do so does not allow the second stage to perform a deorbit burn, hence requiring the analysis of passive deorbiting. The first counteraction taken in order to have better control over reentry is to vent the residual propellant gases through the engine: while they are not sufficient to ignite it and perform a full deorbit burn, they still provide some thrust helping reduce the time in orbit and more accurately selecting the reentry zone. Worst case scenario, assuming no control after payload detachment, as analyzed by NASA<sup>[93]</sup> spacecraft deployed below altitudes of 500km easily deorbit within 5 years time, hence well within the 25-year post-mission time indicated by normative<sup>[93]</sup>. However, a risk assessment must be performed to verify that the probability of casualties remains below the limit imposed by the normative.

## 3.2 Feasibility of Launch Condition

The launch platform selected is the Boeing 747-200SF in accordance to subsection 1.1.5 as a compromise between risk and performance. From the results presented in section 3.1, it is possible to assess that the volume occupied by the vehicle is compliant with the available one under the wing of the chosen carrier. This condition is also satisfied in terms of maximum allowable mass that the Boeing 747-200SF can carry<sup>[53]</sup>. Furthermore, the launch success depends on maintaining nominal conditions across critical factors. Adverse weather, carrier subsystem or release failures, and delays impacting launch window alignment can compromise the mission. As noted in subsubsection 2.2.5.1, LOX boiloff increases with time, so with delays, degrading engine performance.

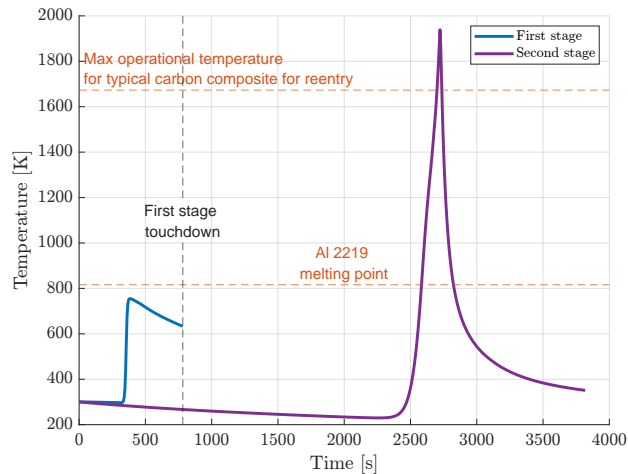


Figure 3.22: Stages temperature during flight  
It is worth pointing out that these results account only for structural integrity of the stage, but do not characterize the ballute components, as its reliability was assumed from literature<sup>[87]</sup>.

### 3.3 Cost Analysis

In order to estimate the number of reuses for ease of ROI, a cost analysis was performed.

First of all, a cost per launch has to be estimated, basing on literature knowledge, by starting with a breakdown into its constituent elements which can be divided into the following:<sup>[8]</sup>

- Design and Development: A nonrecurring cost covering the 4-year design phase, estimated at 10 k\$ per year<sup>[8]</sup>.
- Production: Includes recurring costs for expendable elements and nonrecurring costs for recovered parts, calculated at 2 k\$/kg of inert mass<sup>[8,94]</sup>, plus the cost of 8 motors for the first stage and 1 for the second, estimated 450 k\$<sup>[95]</sup> each. For the expendable parts, a learning factor was considered<sup>[8,94]</sup>.
- Flight Operations: Covers ground operations and launcher use, estimated as a percentage of total launch cost based on literature<sup>[8]</sup>.
- Recovery Operations: Involves cleaning and transporting the recovered first stage. Due to lack in literature, it was estimated at 30 k\$ per launch, including boat rental for the recovery.
- Refurbishment: Includes maintaining reusable elements, combining a refurbishment factor (0.10–0.15) and an aging factor (1.05–1.10)<sup>[8]</sup>.
- Insurance: Estimated at 15% of the launch cost, consistent with literature values of 4%–20%<sup>[8,96]</sup>.
- Boeing 747: To modify for launches as explained in subsection 1.1.5, purchasing a used Boeing 747 was deemed optimal at 6.5 Mln\$<sup>[18]</sup>, as full price, it would be impossible to have ROI in a small number of launches. In a further analysis this aspect should be considered carefully.

Regarding the selling price of a launch, it was found to be related to the payload weight and the target orbit altitude. Taking as reference the Electron, the sustained cost per launch, considering a 250kg payload, is around 5.78Mln\$,<sup>[97]</sup>, while the selling price is 7.5mln \$.<sup>[98]</sup> This values lead to profit equal to the 30% of a launch cost. If a minimum number of 5 launches is set, the price per launch must be at least 4.7Mln \$. The results of the computed costs are represented in Table 3.15

Type of cost	Category	Cost per launch [\$]		
		1 Launch	5 Launches	10 Launches
Non-recurrent costs	Development	40k	8k	4k
	1 <sup>st</sup> stage production	2800k	560k	280k
	1 <sup>st</sup> stage engines	3600k	720k	360k
	Boeing 747	6500k	1300k	650k
Recurrent costs	2 <sup>nd</sup> stage production	400k	175k	122k
	2 <sup>nd</sup> stage engine	450k	450k	450k
	Flight operations	100k	100k	100k
	Recovery operations	30k	30k	30k
	Insurance	2.45mln	544k	299k
	Refurbishment	0	118k	127k
<b>Total cost per launch</b>		16.3mln	3.64mln	2.02mln
<b>Selling price launch</b>		4.7mln	4.7mln	4.7mln
<b>Profit per launch</b>		-11.6mln	+1.06mln	+2.68mln

Table 3.15: Cost Breakdown

It can be observed that, increasing the number of launches, the weight of the initial investment of the non recurrent costs decreases, since it is spread over a higher number of reuses. Regarding the recurrent costs, the second stage production decreases thanks to a learning factor that was considered. While the refurbishment component increases due to the aging of the invested elements as the first stage.

In Figure 3.23, the cost per launch is displayed depending on the total number of launch performed. The break-even point evidently corresponds to the 4<sup>th</sup> launch.

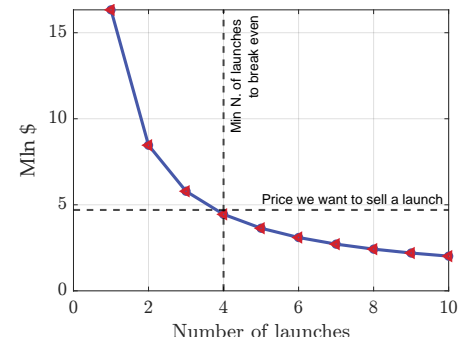


Figure 3.23: Cost per launch

### 3.4 Further Developments

The next iterations will focus on refining the conceptual design by either confirming or revising the initial choices. To achieve this, a sensitivity analysis will be conducted to evaluate the true impact of the key parameters identified in the HoQ on the overall design<sup>[8]</sup>.

Greater detail will be incorporated into the modeling of various subsystems. An initial temperature of 300 K was assumed<sup>[90]</sup>.

- **STR:** Integration of wind effects on both the trajectory and structures to optimize their design and the mass distribution, minimizing the risk of resonance effects<sup>[1]</sup>. Furthermore, to enhance the evaluation of stresses on the common domes, a finite element analysis will be performed, contributing to a more robust and reliable design.
- **PRP:** A refined thermal analysis will be performed for the external panels and the propulsive structures, to determine the thermal loads and stresses during the whole mission and eventually verify the recoverability of the second stage.
- **MSA:** A more precise estimation of the attitude and trajectory, a six DOF simulator will be implemented. This will run in parallel with the development of an advanced control system to manage dynamic aerodynamic moments during the pitch-up phase. Additionally, the controller will be enhanced to improve its robustness and stability, ensuring it can effectively address potential non-nominal conditions throughout the trajectory.
- **AER:** Refine the sizing of the tail control surfaces to enhance their efficiency and optimize the rocket's controllability across its flight envelope. Additionally, conduct an in-depth study on various nose configurations to determine if the conical design is indeed the optimal choice.
- **RCS:** A more detailed thermal analysis is needed to assess re-entry loads for both stages. For the second stage, this will refine recovery feasibility. If recovery is unfeasible, a demise assessment must ensure the stage fully disintegrates in the atmosphere or any fragments land in uninhabited areas<sup>[93]</sup>. Additionally, uncertainty analysis of opening conditions should evaluate recovery robustness.

### 3.5 Conclusions

The conceptual design for an airborne civil launcher has been successfully completed. The results obtained were compared with the imposed programmatic and performance requirements for all the subsystems.

The parameters that guided the workflow were identified with the HoQ, and the ones with the highest weight were actually more involved in the development across every subsystem: this proved the importance of this approach in a real environment.

All the design solutions adopted by the various department and the modifications on the selected launcher platform are feasible and supported by a strong heritage, ensuring robustness and reliability; hence the development of JEENO is reasonably achievable within a short time frame, ensuring the fulfillment of the customer demand in term of time to market.

Regarding the programmatic requirements, recoverability and reusability of the first stage were successfully achieved. However, recoverability of the second stage was not feasible; instead, its deorbiting was ensured for both the 250 kg and 400 kg payload scenarios<sup>[92]</sup>. Additionally, the high FoS and the strategic choice of the launch platform contribute to robust operational safety on the ground. Finally, the selection of the propellant combination ensures limited environmental impact.

Performance requirements were accomplished as well: JEENO is proven to be able to bring a 250 kg payload to a 400 km orbit with an accuracy, in the nominal case, of  $\sim 58\text{ m}$  on the required altitude and  $\sim 3\text{ m/s}$  on the required velocity (Figure 3.17); the selected launch facilities guarantees the possibility to reach an SSO, retrograde orbit as requested by the customer.

Finally, it has been proven, through the cost analysis, that the reusability of the first stage is necessary to lower the cost per launch, allowing JEENO to be competitive in the market; however, even a small number of reuses is sufficient to guarantee a fast ROI.

## A.1 House of Quality

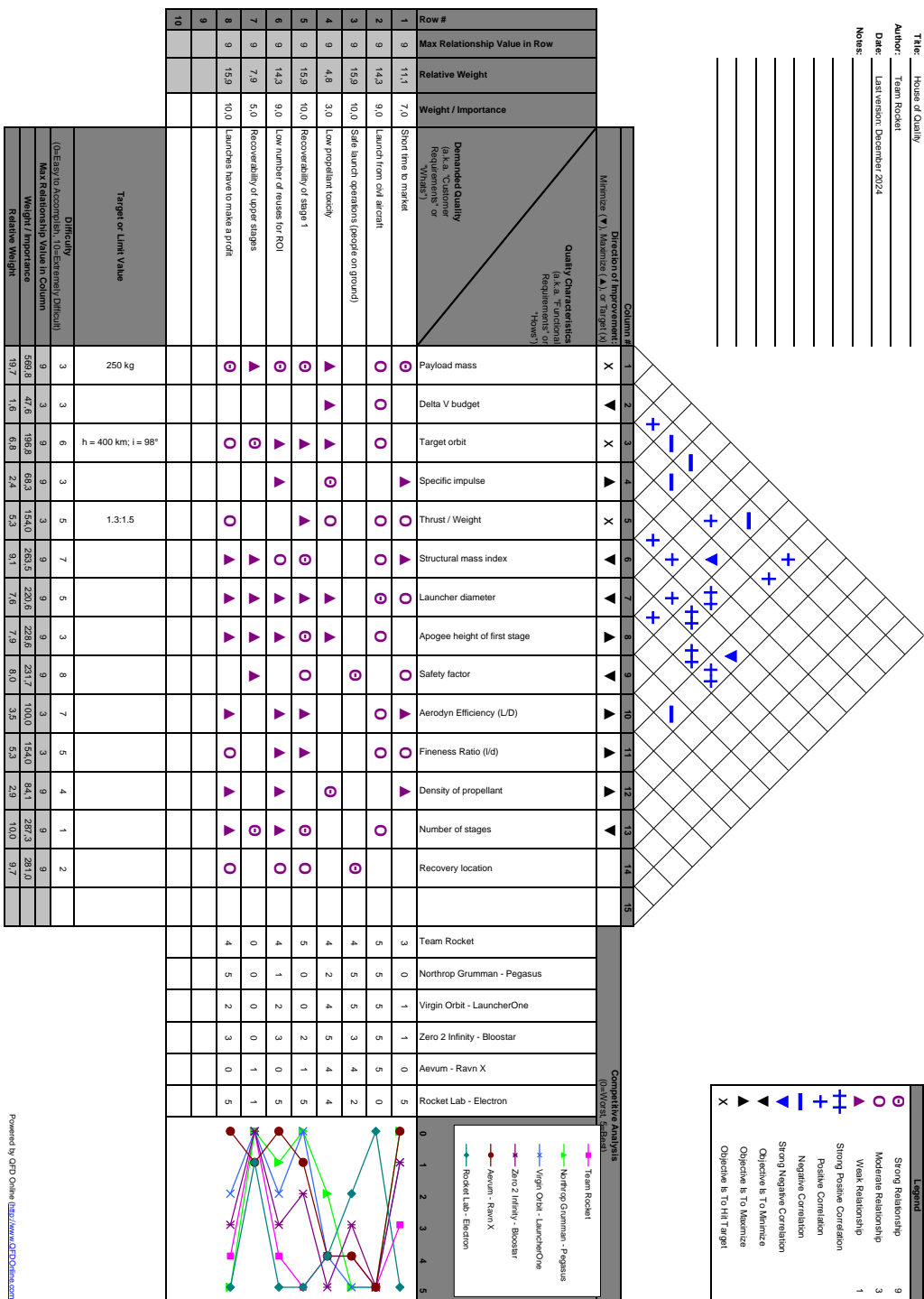


Figure A.1: House of Quality

## B.1 Baseline Data Interpolation

Data from the Electron, LauncherOne and Pegasus were linearly interpolated to generate fitting curves. These curves allowed to determine the volumes by giving as input the GLOM and the mass of the maximum payload (400 kg). Similarly, the finesse ratio was also computed from the fitting starting from the average diameters of the baselines.

For the fairing specifically, values were sourced from user guide manuals [9] [10] [11], approximating the volume as the one of a cone<sup>[1]</sup>.

Linear regression was then applied to interpolate these values, allowing for a preliminary estimation of volumes and internal voids within the launcher body<sup>[99]</sup>.

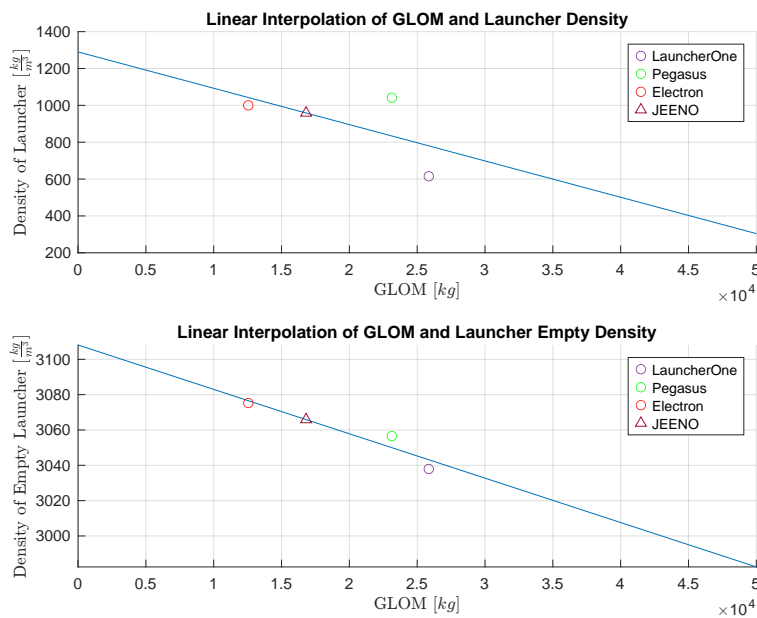


Figure B.1: Linear interpolation of GLOM and Launcher densities

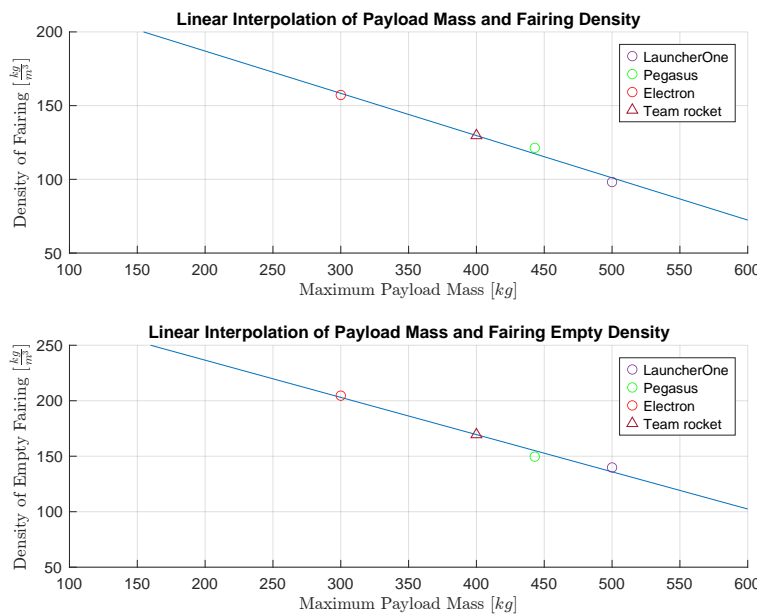


Figure B.2: Linear interpolation of payload mass and fairing densities

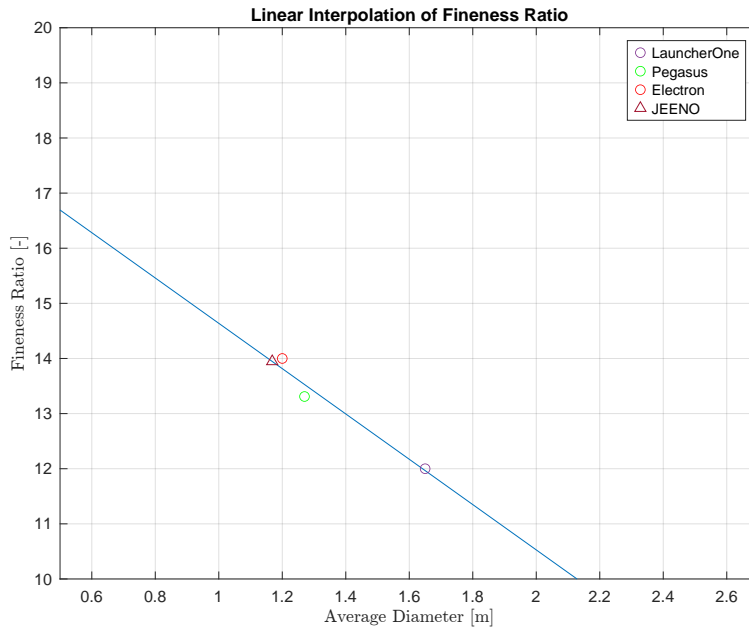


Figure B.3: Linear interpolation of launcher diameter and fineness ratio

A high degree of data scatter can be observed in Figure B.1 for vehicle density values, likely due to technological differences in the propulsion systems of the vehicles. In contrast, lower scatter is noted in Figure B.2 for fairing values which may be attributed to the similarity in payload mass and mission type. Similarly, the fineness ratio plot in Figure B.3 has a low degree of scattering due to mission similarity and the fact that both Pegasus and LauncherOne need to comply to the constraints related to the launcher carrier. For the LauncherOne, an average diameter was computed as an average fineness ratio.

The results of the interpolation served as foundational data for the initial iterations for the conceptual design<sup>[8]</sup>.

## B.2 Optimal Staging

Once the mission budget was estimated, it became possible to determine the inert and propellant masses required for the mission. This involved solving a constrained optimization problem aimed at minimizing the Gross Lift-Off Mass (GLOM) of the launcher. The constraints were imposed through the Lagrange multipliers ( $\lambda$ ) and the algorithm was selected in order to have a higher robustness when using the *fzero* function implemented in Matlab<sup>[23][100]</sup>. The algorithm is as follows:

1. Determining the upper bound of the parameter  $k$  as:

$$0 < k < \min(I_{s_i} \cdot g_0) \quad (\text{B.1})$$

Where  $I_{s_i}$  is the specific impulse of the  $i$ -th stage and  $g_0$  is the gravitational constant set to  $9.80665 \text{ m/s}^2$

2. Applying *fzero* to the equation:

$$\Delta V - \sum_{i=1}^n I_{s_i} \cdot g_0 \cdot \ln \left( \frac{I_{s_i} \cdot g_0 - k}{\epsilon_i \cdot I_{s_i} \cdot g_0} \right) = 0 \quad (\text{B.2})$$

3. Once the root is found from *fzero*,  $k$  is used to compute the optimal Lagrange multiplier for each stage  $\lambda_{opt_i}$

$$\lambda_{opt_i} = \left( \frac{k \cdot \epsilon_i}{(1 - \epsilon_i) \cdot I_{s_i} \cdot g_0 - k} \right) \quad (\text{B.3})$$

4. As the mass of the payload is known ( $m_{L,2}$ ), it is possible to compute all the other masses from top to bottom:

$$m_{s,i} = \frac{\epsilon_i}{\lambda_i} \cdot m_{L,i} \quad (\text{B.4})$$

$$m_{p,i} = \frac{1 - \epsilon_i}{\epsilon_i} \cdot m_{s,i} \quad (\text{B.5})$$

$$m_{0,i} = m_{s,i} + m_{p,i} + m_{L,i} \quad (\text{B.6})$$

The output of this algorithm allowed to find the optimal masses for a first iteration using the data from the selected baseline. This method was chosen as it allowed for a more robust solution once *fzero* was implemented<sup>[23]</sup>.

### B.3 Inert Mass Estimation Formulas

The MER reported in this section were implemented in the computation of the inert masses of the launcher related to the components whose mass cannot be directly sized. Those formulas are based on empirical relations and were taken from different sources from the literature<sup>[30][1]</sup>.

Especially for the case of the recovery system, the masses related to the sensors and deployment devices needed to be accounted for in the sizing<sup>[4]</sup>.

The formulas are here reported:

$$m_{LVA} = 0.0755 \cdot m_{pay} + 50^{[1]} \quad (\text{B.7})$$

$$m_{\text{avionics}} = \begin{cases} 75, & \text{if } m_{\text{pay}} < 10^3 \text{ [kg]}^{[1]} \\ 350, & \text{if } m_{\text{pay}} > 10^3 \text{ [kg]}^{[1]} \end{cases} \quad (\text{B.8})$$

$$m_{\text{wiring}} = 1.43 \cdot L_0^{[1]} \quad (\text{B.9})$$

$$m_{\text{thrust-struct}} = 2.55 \cdot 10^{-4} \cdot T_{\text{motors}}^{[30]} \quad (\text{B.10})$$

$$m_{\text{LOX-ins}} = 1.123 \cdot S_{\text{tank-LOX}}^{[30]} \quad (\text{B.11})$$

$$m_{\text{recovery}} = 0.07 \cdot m_{s-\text{recovered}}^{[4]} \quad (\text{B.12})$$

$$m_{\text{fins}} = 2.2679 \cdot (S_{\text{fins}} \cdot 10.7639)^{1.09}^{[31]} \quad (\text{B.13})$$

In the reported equations, the mass of the avionics ( $m_{\text{avionics}}$ ) is 20% on the first stage and 80% on the second stage, while the mass of the wiring ( $m_{\text{wiring}}$ ) were proportionally distributed along the length of the stages, where  $L_0$  is the total length of the launcher. Moreover, the mass of the thrust structure ( $m_{\text{thrust-struct}}$ ) was determined based on the varying thrust levels ( $T_{\text{motors}}$ ) specific to the first and second stages. Furthermore, regarding the tanks for the LOX, the mass of the insulation ( $m_{\text{LOX-ins}}$ ) was taken in to account and it was proportional to the lateral surface of the tank( $S_{\text{tank-LOX}}$ ). The mass of the parachute ( $m_{\text{recovery}}$ ) is evaluated as 7% of the inert mass of the stage to be recovered ( $m_{s-\text{recovered}}$ ). Finally, the mass of the movable fins attached to the first stage ( $m_{\text{fins}}$ ) depends on the value of the surface ( $S_{\text{fins}}$ , subsection 2.3.3).

### B.4 Yielding Resistance

The thicknesses that guarantee resistance in the elastic field (subsection 2.1.4) of the materials were found in the following way:

#### Axial resistance to $P$ , $M$ , $p$ , $p_{\text{hydro}}$ :

This is the condition experienced by the bottom part of the tanks (with radius  $R$  and thickness  $t$ ) in the longitudinal direction, during the rocket flight. It is the most general case between the presented, however not necessarily it represents the more demanding:

$$\sigma^y = \frac{M}{\pi R^2 t} + \frac{P}{2\pi R t} - \frac{(p + p_{hydro})R}{2t} [1] \quad (\text{B.14})$$

With  $\sigma^y$  being the maximum yielding stress that the material can sustain (subsection 2.1.5).  $p_{hydro}$  is the hydrostatic pressure due to the fluid (propellant) pushed to the bottom of the tank. Its value derives from the Stevin's Law:

$$p_{hydro} = \rho g_0 n_x h \quad (\text{B.15})$$

With  $g_0=9.81 \text{ m/s}^2$ ,  $n_x=6$  (subsection 2.1.4) and  $h$  being the total height of the tank. Inverting the relation, one can compute the minimum thickness, including the FoS:

$$t_{min1} = FoS \times \left( \frac{M}{\pi R^2 \sigma^y} + \frac{P}{2\pi R \sigma^y} - \frac{(p + p_{hydro})R}{2\sigma^y} \right) \quad (\text{B.16})$$

### Axial resistance to $P$ , $M$ , $p$ :

This is the condition experienced by the top part of the tanks in the longitudinal direction, while the rocket is flying and accelerating:

$$\sigma^y = \frac{M}{\pi R^2 t} + \frac{P}{2\pi R t} - \frac{pR}{2t} [1] \quad (\text{B.17})$$

Where the values have the same meaning explained before. Inverting the relation:

$$t_{min2} = FoS \times \left( \frac{M}{\pi R^2 \sigma^y} + \frac{P}{2\pi R \sigma^y} - \frac{pR}{2\sigma^y} \right) \quad (\text{B.18})$$

It is highlighted how this condition represents also the *forward skirt* and *after skirt* condition simply by imposing  $p$  equal to zero.

### Hoop resistance to $p$ , $p_{hydro}$ :

This is the condition experienced by the bottom part of the tanks in the transversal direction, due to the internal pressure of the vessels:

$$\sigma^y = \frac{(p + p_{hydro})R}{2t} [1] \quad (\text{B.19})$$

In this case, the minimum thickness is:

$$t_{min3} = FoS \times \left( \frac{(p + p_{hydro})R}{2\sigma^y} \right) \quad (\text{B.20})$$

### Axial resistance to $M$ :

This is the condition that all the components experience when the launcher is empty of propellant, before the refueling and pressurization, with  $p = p_{hydro} = 0$ . The equation is:

$$\sigma^y = \frac{M}{\pi R^2 t} [1] \quad (\text{B.21})$$

Yielding to a minimum thickness of:

$$t_{min4} = FoS \times \left( \frac{M}{\pi R^2 \sigma^y} \right) \quad (\text{B.22})$$

These minimum thicknesses are computed for each component. Then, to determine the thickness (**just** for yielding resistance) of the single component the maximum between Equation B.16, Equation B.18, Equation B.20, and Equation B.22 is picked.

## B.5 Buckling Analysis

The buckling analysis for this project was carried out starting from the buckling studies conducted by NASA in the 1960s<sup>[36]</sup><sup>[38]</sup><sup>[37]</sup>. Using some of the purely empirical formulas suggested for isotropic materials, a general methodology can be used for truncated-cone shaped components, of which cylinders are merely a special case.

In fact, adopting the following convention:

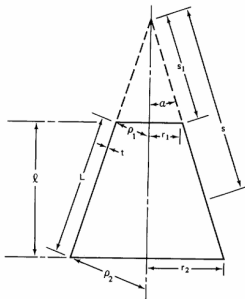


Figure B.4: Definition of Cone Parameters

It is clear how cylinders can be seen as cones with  $\alpha = 0$  and  $r_1 = r_2 = r$ .

Therefore, to simplify the discussion we treat the buckling for thin-walled truncated cones, and then we introduce the special cases for cylinders (keeping in mind the previous assumption).

In the current document the focus is only on buckling caused by compressive load and bending moment acting on the structure, therefore the other cases will be omitted.

It is highlighted how the formulas presented in this section are valid only if the following condition is respected:

$$\frac{r_2}{t} < 1500^{[37]} \quad (\text{B.23})$$

With  $r_2$  being equal to the radius of the cylinder in the case  $\alpha = 0$ . This theory should be used with caution for  $\frac{r_2}{t} > 1500$  as experimental data are not available<sup>[37]</sup>. This validity range was accounted imposing a lower bound on the thickness of the walls of:

$$t_{min} = \frac{r_2}{1500} \quad (\text{B.24})$$

There are two main cases in which assess the critical loads for bending and axial compression: with and without internal pressure of the vessel. In this section the pressure will be indicated by  $\Delta p$ , defined as the difference between the internal and the external pressure,  $\Delta p = p_{int} - p_{ext}$ . The next two paragraphs will further explain the methodology adopted.

### B.5.1 Pressurized vessels: $\Delta p > 0$

The internal pressure,  $\Delta p$ , is useful to retard the buckling effect, mainly because of three phenomena:

1. The total axial compressive load must overtake the internal tensile load due to  $\Delta p$ <sup>[37]</sup>.
2. The magnitude of the imperfections that usually start the buckling is reduced<sup>[37]</sup>.
3. The circumferential tensile stress induced by  $\Delta p$  inhibits the formation of the buckling patterns<sup>[37]</sup>.

Hence, the critical loads ( $P_{cr}$  for axial compressive load,  $M_{cr}$  for bending moment) are increased when  $\Delta p > 0$ .

Their value is:

$$P_{cr} = 2\pi E(t \cos \alpha)^2 \left( \frac{\gamma_P}{\sqrt{3(1 - \nu^2)}} + \Delta\gamma \right) + \Delta p \pi r_1^2 [38] [37] \quad (\text{B.25})$$

$$M_{cr} = \pi E(t \cos \alpha)^2 r_1 \left( \frac{\gamma_M}{\sqrt{3(1 - \nu^2)}} + \Delta\gamma \right) + K \Delta p \pi r_1^3 [38] [37] \quad (\text{B.26})$$

Where  $\mathbf{E}$  is the Young modulus of the material,  $t$  is the thickness of the shell and  $\nu$  is the Poisson's ratio of the material.

The remaining parameters depend on the geometry of the shell:

$$\gamma_P = \begin{cases} 0.33 & \text{if } 10^\circ < \alpha < 75^\circ [38] \\ 1 - 0.901(1 - e^{-\phi}) & \text{if } \alpha = 0 [37] \end{cases} \quad (\text{B.27})$$

$$\gamma_M = \begin{cases} 0.41 & \text{if } 10^\circ < \alpha < 60^\circ [38] \\ 1 - 0.731(1 - e^{-\phi}) & \text{if } \alpha = 0 [37] \end{cases} \quad (\text{B.28})$$

These two are called *buckling knockdown factors*. Their value for conical shapes was taken even for  $0^\circ < \alpha < 10^\circ$ , since this leads to overestimate the minimum thickness with respect to the  $\alpha = 0$  case. And since small values of  $\alpha$  mean shape similar to cylinders, this overestimation is taken as a safety margin on the structure.

$\phi$  is a nondimensional parameter, defined as:

$$\phi = \frac{1}{16} \sqrt{\frac{r}{t}} [37] \quad (\text{B.29})$$

The following parameter is not defined by the sources: it was defined by the writer only to generalize the discussion.

$$K = \begin{cases} 0.5 & \text{if } \alpha > 0 [38] \\ 0.8 & \text{if } \alpha = 0 [37] \end{cases} \quad (\text{B.30})$$

The last parameter,  $\Delta\gamma$ , is a function of  $\Delta p$ ,  $\mathbf{E}$ ,  $r_1$ ,  $t$ ,  $\alpha$ , and its value is obtained from a diagram interpolation. The following figure shows the original and the derived diagrams:

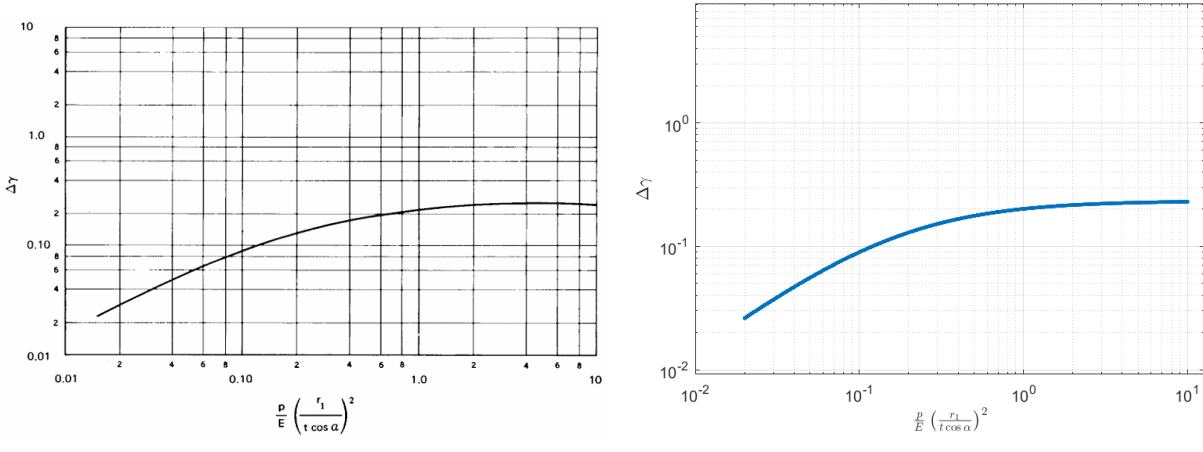


Figure B.5:  $\Delta\gamma$  Diagram

Where the term  $p$  in the graphs is our  $\Delta p$ . The interpolation was made using four points:

$$\Delta\gamma = \begin{cases} 0.026 & \text{for } \left[ \frac{\Delta p}{E} \left( \frac{r_1}{t \cos \alpha} \right)^2 \right] = 0.02 \\ 0.090 & \text{for } \left[ \frac{\Delta p}{E} \left( \frac{r_1}{t \cos \alpha} \right)^2 \right] = 0.10 \\ 0.200 & \text{for } \left[ \frac{\Delta p}{E} \left( \frac{r_1}{t \cos \alpha} \right)^2 \right] = 1.00 \\ 0.230 & \text{for } \left[ \frac{\Delta p}{E} \left( \frac{r_1}{t \cos \alpha} \right)^2 \right] = 10.0 \end{cases} \quad (\text{B.31})$$

And the following parametrized equation:

$$\Delta\gamma = f \left( \left[ \frac{\Delta p}{E} \left( \frac{r_1}{t \cos \alpha} \right)^2 \right] \right) = \frac{a \times \left[ \frac{\Delta p}{E} \left( \frac{r_1}{t \cos \alpha} \right)^2 \right] + b}{c \times \left[ \frac{\Delta p}{E} \left( \frac{r_1}{t \cos \alpha} \right)^2 \right] + d} \quad (\text{B.32})$$

Using the *MatLab curveFitter* tool to obtain the four parameters ( $a$ ,  $b$ ,  $c$  and  $d$ ), the result is:

$$\begin{bmatrix} a \\ b \\ c \\ d \end{bmatrix} = \begin{bmatrix} 0.3045 \\ 0.0001 \\ 1.3064 \\ 0.2104 \end{bmatrix} \quad (\text{B.33})$$

This result is quite adherent to the four initial points: R-square = 0.99995, SSE = 1.241e-6. Thus, the parametrized equation Equation B.32 can be used to obtain  $\Delta\gamma$ , given  $\Delta p$ ,  $E$ ,  $r_1$ ,  $t$ ,  $\alpha$ .

It is clear that four points to assess  $\Delta\gamma$  are a poor set of data, but care was taken when picking the values of the four points, to stay under the original curve Figure B.5. Furthermore, this empirical approach is said to be quite conservative<sup>[37]</sup>, hence its usage is recommended for preliminary designs.

### B.5.2 Unpressurized vessels: $\Delta p = 0$

From the sources<sup>[38]</sup> it is trivial to demonstrate that, in the special case of  $\alpha > 0$  (only truncated-cones), the critical loads for the unpressurized case are obtained simply by imposing  $\Delta p=0$ ,  $\Delta\gamma=0$  in Equation B.25 and Equation B.26. Thus, for  $\alpha > 0$ :

$$P_{cr} = 2\pi E(t \cos \alpha)^2 \left( \frac{\gamma_P}{\sqrt{3(1 - \nu^2)}} \right) \quad [38] \quad (\text{B.34})$$

$$M_{cr} = \pi E(t \cos \alpha)^2 r_1 \left( \frac{\gamma_M}{\sqrt{3(1 - \nu^2)}} \right) \quad [38] \quad (\text{B.35})$$

Using, from Equation B.27 and Equation B.28:  $\gamma_P = 0.33$ ,  $\gamma_M = 0.41$ <sup>[38]</sup>.

In case of  $\alpha = 0$  (pure cylinders), different formulas can be adopted<sup>[37]</sup>:

$$P_{cr} = 2k_x \frac{\pi^3 Dr}{l^2} \quad [37] \quad (\text{B.36})$$

$$M_{cr} = k_x \frac{\pi^3 Dr^2}{l^2} \quad [37] \quad (\text{B.37})$$

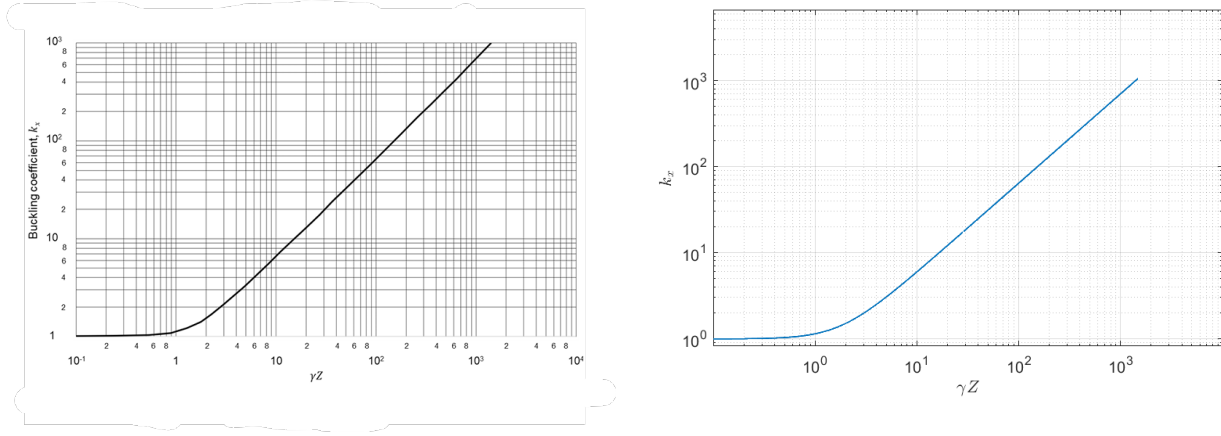
Where  $l$  is the length of the shell, as defined in Figure B.4.

The other parameters are defined as:

$$D = \frac{Et^3}{12(1 - \nu^2)} \quad (\text{B.38})$$

That is the *Wall Flexural Stiffness per unit width*. The *Buckling Coefficient*,  $k_x$ , depends on the geometrical properties of the vessel and on the Poisson's ratio. Since the source<sup>[37]</sup> reports a

diagram, but not an explicit formula to obtain this value, it was estimated similarly to the parameter  $\Delta\gamma$  in subsection B.5.1:



(a) Original  $k_x$  Diagram<sup>[37]</sup>

(b) Interpolated  $k_x$  Diagram

Figure B.6:  $k_x$  Diagram

In particular, five points were taken to start the interpolation:

$$k_x = \begin{cases} 1.0 & \text{for } \gamma Z = 0.1 \\ 1.1 & \text{for } \gamma Z = 1.0 \\ 2.0 & \text{for } \gamma Z = 3.0 \\ 64.0 & \text{for } \gamma Z = 100.0 \\ 700.0 & \text{for } \gamma Z = 1000.0 \end{cases} \quad (\text{B.39})$$

Using the parametrized equation:

$$k_x = f(\gamma Z) = c \times (a + (\gamma Z)^2)^b \quad (\text{B.40})$$

The *curveFitter* tool is used to get the parameters:

$$\begin{bmatrix} a \\ b \\ c \end{bmatrix} = \begin{bmatrix} 3.2513 \\ 0.5195 \\ 0.5348 \end{bmatrix} \quad (\text{B.41})$$

This result comes with R-square=1.0000, SSE=0.0025. Hence, the function that bonds  $k_x$  and  $\gamma Z$  is obtained.

In this equation,  $\gamma$  is the *buckling knockdown factor* already seen in subsection B.5.1, and to compute it can be used the previous Equation B.27, Equation B.28 for the case  $\alpha = 0$  (for  $P_{cr}$ ,  $M_{cr}$  respectively).

The remaining parameter,  $Z$ , is called the *curvature parameter*<sup>[37]</sup>, and it is defined as:

$$Z = \frac{l^2}{rt} \sqrt{1 - \nu^2} \quad (\text{B.42})$$

### B.5.3 Combined loads

Once the critical loads  $P_{cr}$ ,  $M_{cr}$  are defined, the condition to be satisfied to preserve the structure from failure is:

$$\frac{P_{real}}{P_{cr}} + \frac{M_{real}}{M_{cr}} < 1^{[38][37]} \quad (\text{B.43})$$

Since the purpose of the structural sizing is to define the thicknesses given the estimated loads, the problem was stated in the following way:

$$FoS \times \left[ \frac{P_{estimate}}{P_{cr}(t)} + \frac{M_{estimate}}{M_{cr}(t)} \right] = 1 \quad (\text{B.44})$$

Where FoS is the same used in subsection 2.1.2. It is necessary to account for it: the presence of the *buckling knockdown factors* (Equation B.27, Equation B.27) does not exclude the need of margins<sup>[37]</sup>.

The problem, stated in this way, is implicit. Therefore, the *MatLab* function *fzero* was used, when the Equation B.43 wasn't already satisfied by the minimum thicknesses found for assessing the resistance in the elastic field of the materials (subsection 2.1.4), the limit for manufacturability (subsection 2.1.5), or to satisfy the validity ranges of the equations (Equation B.24).

## B.6 Admissible Bending Moments

In this section are exposed the admissible bending moments during the flight, computed using Equation B.18, Equation B.36, Equation B.37, Equation B.25, Equation B.26, and Equation B.44, starting from the compressive axial load coming from section 2.4. In fact, adopting the final configuration of the rocket (section 3.1) and the planned trajectory, one can compute the effective loads acting during the flight, and compare them with the maximum that the structure could sustain. The result is shown in the following images:

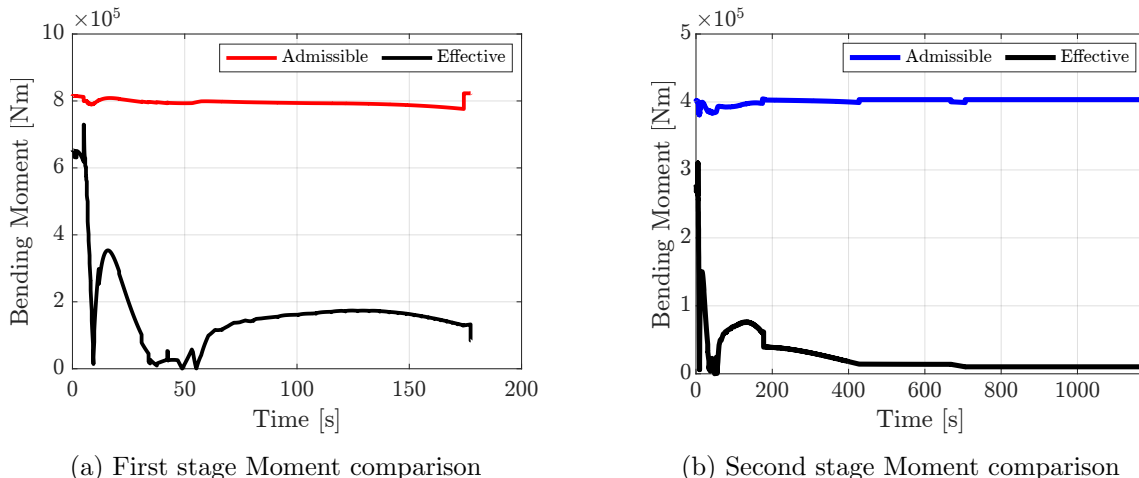


Figure B.7: Admissible Bending Moments compared to Effective during flight

## C.1 The Pflanz Method for Calculating Parachute Opening Forces

The Pflanz method, developed in Germany during World War II by E. Pflanz, provides a mathematically exact approach to calculate parachute opening forces. This method assumes that a body of known fixed weight and velocity is decelerated along a horizontal flight path by an aerodynamic drag device whose drag area increases from a small value to 100% in a mathematically definable form. Notably, this method does not account for any overshoot of the drag area,  $(CDS)_p$ , at the start of reefed or disreefed inflation cycles.

### C.1.1 Ballistic Parameter and Force-Reduction Factor

The Pflanz method introduces a dimensionless ballistic parameter,  $A$ , defined as:

$$A = \frac{2W_t}{(CDS)_p p g V_{tf}}$$

where:

- $W_t$ : System weight, in pounds (lb).
- $(CDS)_p$ : Parachute projected drag area (reefed or fully open), in square feet ( $\text{ft}^2$ ).
- $p$ : Air density at the altitude of parachute inflation, in slugs per cubic foot (slugs/ $\text{ft}^3$ ).
- $g$ : Acceleration due to gravity, in feet per second squared ( $\text{ft}/\text{s}^2$ ).
- $V$ : Velocity at line stretch or start of disreef, in feet per second ( $\text{ft}/\text{s}$ ).
- $t_f$  is the canopy inflation time time, also known as filling time. It is computed as a multiple of the nominal diameter  $D_0$ :

$$t_f = \frac{n D_0}{v} \quad (\text{C.1})$$

The parameter  $n$  depends on the parachute type and on the reefing stage. It is equal to 7 for the reefed ringsail opening and 2 for the disreefing opening<sup>[4]</sup>; it results in 0.7 s and 0.23 s respectively.

Once the ballistic parameter  $A$  is calculated, the force-reduction factor,  $X_1$ , can be determined from interpolation of experimental curves, which provide  $X_1$  as a function of  $A$  and the drag-area-versus-time rise characteristic,  $n$ . In our case,  $n = 2$ <sup>[4]</sup>. In Figure C.1 the interpolated points for the reefed opening and the disreefing are shown.

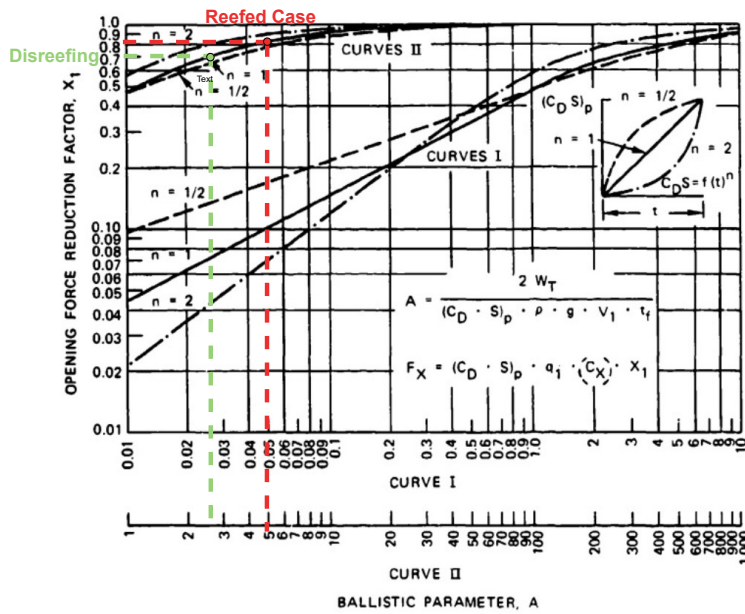


FIGURE C.1. Opening-Force Reduction Factor,  $X_1$ , Versus Ballistic Parameter,  $A$ .

Figure C.1: Linear interpolation of reduction force factor<sup>[4]</sup>

After determining the force-reduction factor,  $X_1$ , from the appropriate curve, the opening force,  $F_p$ , is calculated using the equation:

$$F_p = (CDS)_p q_1 C_x X_1$$

where:

- $(CDS)_p$ : Drag area of the fully open or reefed parachute.
- $q_1$ : Dynamic pressure at the start of inflation or disreef.
- $C_x$ : Opening-force coefficient for the reefed or unreefed parachute (to be used only for low canopy loading conditions). Since it is not our case,  $C_x$  is equal to 1<sup>[4]</sup>.
- $X_1$ : Force-reduction factor from Figure C.1.

## D.1 Aerodynamic Models

This section describes the procedure for calculating the total lift coefficient ( $C_L$ ), the total drag coefficient ( $C_D$ ), and the position of the center of pressure ( $x_{cp}$ ) for a configuration consisting of a central body, wing, and tail. However, for the JEENO launcher, only the contributions from body and tail have been considered, as there is no wing.

### Calculation of the Lift Coefficient ( $C_L$ )

The total lift coefficient is obtained by summing the contributions of each component<sup>[5]</sup>: the body, wing, and tail. The lift of each component depends on the interference between the surfaces and the geometric characteristics of the system. Each contribution is described below.

#### 1. Contribution of the Body Nose ( $C_L^N$ ):

The contribution of the body nose is calculated using slenderbody theory<sup>[71]</sup>, which considers the lift generated by the shape of the body. The lift from the nose is proportional to the angle of attack and the front surface area of the body. The term is given by:

$$C_L^N = \frac{2\pi r_N^2}{S_W} \alpha \quad (\text{D.1})$$

#### 2. Wing Lift in presence of the Body ( $C_L^{W(B)}$ ):

The interference between the body and the wing modifies the aerodynamic load on the wing itself.

The lift of the wing in presence of the body is calculated as:

$$C_L^{W(B)} = K_{W(B)} \cdot (C_{L\alpha})_W \cdot \alpha \quad (\text{D.2})$$

Where  $K_{W(B)}$  is an interference factor that accounts for the geometry of the body and the wing. It is given by:

$$K_{W(B)} = \frac{2}{\pi} \frac{\left\{ \left(1 + \frac{r^4}{s^4}\right) \left[ \frac{1}{2} \tan^{-1} \left( \frac{s}{r} - \frac{r}{s} \right) + \frac{\pi}{4} \right] - \frac{r^2}{s^2} \left[ \frac{s}{r} - \frac{r}{s} \right] + 2 \tan^{-1} \left( \frac{r}{s} \right) \right\}}{\left(1 - \frac{r}{s}\right)^2} \quad (\text{D.3})$$

In the limiting case of  $r/s = 0$  the combination is all wing and  $K_{W(B)} = 1$ <sup>[5]</sup>. As  $r/s$  approaches unity, there is a very small exposed wing, the body is effectively a vertical reflection plane and the angle of attack is  $2\alpha$  due to upwash, this makes  $K_{W(B)} = 2$ <sup>[5]</sup>.

#### 3. Body Lift induced by the Wing ( $C_L^{B(W)}$ ):

The wing also induces lift on the body, which is calculated as:

$$C_L^{B(W)} = K_{B(W)} \cdot (C_{L\alpha})_W \cdot \alpha \quad (\text{D.4})$$

Where  $K_{B(W)}$  is another interference factor given by:

$$K_{B(W)} = \frac{\left(1 - \frac{r^2}{s^2}\right)^2 - \frac{2}{\pi} \left\{ \left(1 + \frac{r^4}{s^4}\right) \left[ \frac{1}{2} \tan^{-1} \frac{1}{2} \left(\frac{s}{r} - \frac{r}{s}\right) + \frac{\pi}{4} \right] - \frac{r^2}{s^2} \left[ \left(\frac{s}{r} - \frac{r}{s}\right) + 2 \tan^{-1} \frac{r}{s} \right] \right\}}{\left(1 - \frac{r}{s}\right)^2} \quad (\text{D.5})$$

In the limiting case of  $r/s = 0$  the combination is all wing and  $K_{B(W)} = 0^{[5]}$ . As  $r/s$  approaches unity, there is a very small exposed wing. For this small wing the lift on the body due to the wing is the same as the lift on the wing itself, this makes  $K_{B(W)} = 2^{[5]}$ .

4. Tail lift in presence of the Body ( $C_L^{T(B)}$ ):

It can be computed using (D.2) and (D.3) by changing the terms referring to the wing with the tail ones.

5. Body Lift induced by the Tail ( $C_L^{B/T}$ ):

It can be computed using (D.4) and (D.5) by changing the terms referring to the wing with the tail ones.

6. Lift induced by Wing Vortices on the Tail ( $C_L^{T(V)}$ ):

The wing generates vortices that affect the lift on the tail (see Figure D.1). The effect of the vortices is modeled by considering the induced angle of attack on the tail:

$$C_L^{T(V)} = \frac{(C_{L\alpha})_W (C_{L\alpha})_T (K_{W(B)} \cdot \alpha) \cdot i \cdot (s_T - r_T)}{2\pi A_T (f_W - r_W)} \quad (\text{D.6})$$

Where  $f_w$  is the lateral position of the wing vortex, and  $i$  is a tail interference factor:

$$f_W = \frac{(C_L)_W S_W}{2(c_l c)} \quad (\text{D.7})$$

$$i = \frac{L_{T(V)}/(L_T)_\alpha}{\Gamma_m/2\pi\alpha V_\infty (s_T - r_T)} \quad (\text{D.8})$$

$\Gamma_m$  is the circulation at the wing-body juncture, defined as:

$$\Gamma_m = \frac{V_\infty K_{W(B)} \cdot \alpha}{4(f_W - r_W)} (C_{L\alpha})_W S_W \quad (\text{D.9})$$

Another way to compute the tail interference factor can be seen in Appendix B of NACA Report 1307<sup>[5]</sup>.

7. Lift on Wing afterbody due to Wing vortices ( $C_L^{B(V)}$ ):

The vortices generated by the Wing act on the afterbody influencing the lift:

$$C_L^{B(V)} = -\frac{4\Gamma_m}{S_W V_\infty} \left[ \frac{(f_W^2 - r_W^2)}{f_W} - f_T + \frac{r_T^2}{\sqrt{f_T^2 + r_T^2}} \right] \quad (\text{D.10})$$

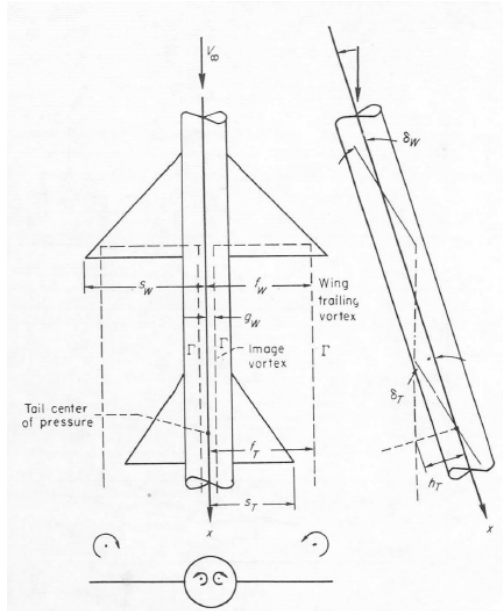


Figure D.1: Vortex model used in determination of wing-tail interference<sup>[5]</sup>

### Calculation of the Center of Pressure Position ( $x_{cp}$ )

The position of the center of pressure  $x_{cp}$  is determined by considering the total moment generated by the aerodynamic forces of each component (body, wing, and tail) with respect to the tip of the nose of the Launcher. This position is calculated as the weighted average of the positions of each component, weighted by the respective lift contributions<sup>[5]</sup>.

The position of the center of pressure is:

$$x_{cp} = \frac{\sum_i x_i L_i}{\sum_i L_i} \quad (\text{D.11})$$

#### 1. Center of pressure of Body Nose:

The position of the Body Nose contribution is estimated with sufficient accuracy by slender-body theory<sup>[71]</sup>:

$$\bar{x}_N = l_S \left( 1 - \frac{V_S}{\pi r_N^2 l_S} \right) \quad (\text{D.12})$$

#### 2. Center of pressure of Wing in presence of Body:

The center of pressure of a wing in presence of an infinite cylindrical body can be computed by slender-body theory<sup>[71]</sup>:

$$\bar{l}_{W(B)} = l_W + (c_r)_W (x/c_r)_{W(B)} \quad (\text{D.13})$$

Where  $(x/c_r)_{W(B)}$  is:

$$\left( \frac{\bar{x}}{c_r} \right)_{W(B)\alpha} = \frac{1}{\left( 1 - \frac{r}{s} \right)} \times \frac{2 \left( \frac{1}{3} + \frac{r^4}{s^4} \right) \tan^{-1} \left( \frac{s}{r} \right) + \frac{2}{3} \frac{r^3}{s^3} \ln \left[ \left( \frac{s^2+r^2}{2s^2} \right)^2 \frac{s}{r} \right] - \frac{1}{3} \frac{r^3}{s^3} \left( 2\pi - 1 + \frac{s^2}{r^2} \right)}{\left( 1 + \frac{r^2}{s^2} \right)^2 \tan^{-1} \left( \frac{s}{r} \right) - \frac{r^2}{s^2} [\pi + \left( \frac{s}{r} - \frac{r}{s} \right)]} - \frac{\frac{r}{s}}{\left( 1 - \frac{r}{s} \right)} \quad (\text{D.14})$$

#### 3. Center of pressure on Body due to Wing:

The center of pressure acting on the body due to the wing is determined by different methods,

depending on whether subsonic or supersonic flow is considered. The assumption is made that the center of pressure of the lift transferred from the wing to the body is not sensitive whether the lift is developed by angle of attack or by wing deflection<sup>[5]</sup>.

$$\bar{l}_{B(W)} = l_W + (c_r)_W (x/c_r)_{B(W)} \quad (\text{D.15})$$

with:

$$\left( \frac{\bar{x}}{c_r} \right)_{B(W)} = \frac{M_{B(W)}}{L_{B(W)} c_r} = \frac{M_{B(W)}}{K_{B(W)} L_W c_r} \quad (\text{D.16})$$

Where  $M_{B(W)}$  is the moment of the lift carried onto the body, and has to be computed for two different cases:

- Supersonic case:

$$M_{B(W)} = \frac{4q_\infty \alpha_W m_s}{3\pi\beta} c_r^3 \left\{ \sqrt{1 + \frac{2\beta d}{c_r}} \left[ \frac{2m_s\beta + 5}{3(m_s\beta + 1)^2} + \frac{\beta d/c_r}{3(m_s\beta + 1)} - \frac{(\beta d/c_r)^2}{\beta m_s} \right] \right. \\ \left. + \frac{1}{\sqrt{m_s^2\beta^2 - 1}} \left[ \left( 1 + \frac{\beta d}{c_r} \right)^3 - \frac{(\beta d/c_r)^3}{m_s^2\beta^2} - \frac{1}{(1 + m_s\beta)^2} \right] \cos^{-1} \left[ \frac{1 + \frac{\beta d}{c_r}(m_s\beta + 1)}{m_s\beta + \frac{\beta d}{c_r}(m_s\beta + 1)} \right] \right. \\ \left. + \left( \frac{\beta d}{c_r} \right)^3 \frac{1}{m_s^2\beta^2} \cosh^{-1} \left( 1 + \frac{c_r}{\beta d} \right) - \left[ \frac{2m_s\beta + 5}{3(m_s\beta + 1)^2} \right] - \frac{\left[ 1 - \left( \frac{1}{m_s\beta + 1} \right)^2 \right]}{\sqrt{m_s^2\beta^2 - 1}} \cos^{-1} \left( \frac{1}{m_s\beta} \right) \right\} \quad (\text{D.17})$$

- Subsonic case:

$$M_{B(W)} = \frac{4q_\infty \alpha_W}{\pi\beta^2} c_r^3 \left\{ \frac{\sqrt{m_s^2\beta^2 + m_s\beta(m_s\beta + 1)\frac{\beta d}{c_r}}}{9m_s\beta(m_s\beta + 1)^3} \left[ (8m_s\beta + 24)m_s^2\beta^2 + (14m_s\beta + 6)(m_s\beta + 1) \right. \right. \\ \left. \left. m_s\beta \frac{\beta d}{c_r} + 3(m_s\beta - 3)(m_s\beta + 1)^2 \left( \frac{\beta d}{c_r} \right)^2 \right] - \frac{(8m_s\beta + 24)m_s^3\beta^3}{9m_s\beta(m_s\beta + 1)^3} - \frac{(m_s\beta - 3)}{3m_s\beta} \left( \frac{\beta d}{c_r} \right)^3 \right. \\ \left. \times \cosh^{-1} \left( \sqrt{\frac{m_s\beta + (m_s\beta + 1)\frac{\beta d}{c_r}}{(m_s\beta + 1)\frac{\beta d}{c_r}}} \right) \right\} \quad (\text{D.18})$$

#### 4. Center of pressure of Tail in presence of Body:

The center of pressure of the tail in presence of the body (wing-tail interference being neglected) is given by the same procedure as that for the wing<sup>[5]</sup>.

#### 5. Center of pressure on Body due to Tail:

The center of pressure on the body due to the tail, wing-tail interference being neglected, is determined by the same procedure as that due to the wing<sup>[5]</sup>.

#### 6. Center of pressure of tail section due to wing vortices:

The flow over the tail due to the wing vortices varies greatly as the position of the vortex varies with respect to the tail. It follows that the center of pressure of the lift due to the effect of the vortices on the tail section is also dependent on the position of the vortices with respect to the tail. It is possible on the basis of strip theory to take account of this effect. However, the refinement is hardly warranted in view of the fact that the distance from the center of moments to the tail is usually large so that great precision in the location of the center of pressure of the load on the tail section due to the wing vortices is unnecessary. A

good approximation is to take the center of pressure as that for the tail panels in combination with the body<sup>[5]</sup>.

$$\bar{l}_{T(V)} = \bar{l}_{T(B)} \quad (\text{D.19})$$

The center of pressure of the entire combination is thus:

$$\bar{l}_C = \frac{\bar{l}_N (C_L)_N + \bar{l}_{W(B)} (C_L)_{W(B)} + \bar{l}_{B(W)} (C_L)_{B(W)} + \bar{l}_{B(T)} (C_L)_{B(T)} + \bar{l}_{T(B)} (C_L)_{T(B)} + \bar{l}_{T(V)} (C_L)_{T(V)}}{(C_L)_N + (C_L)_{W(B)} + (C_L)_{B(W)} + (C_L)_{B(T)} + (C_L)_{T(B)} + (C_L)_{T(V)}} \quad (\text{D.20})$$

### Calculation of the Drag Coefficient ( $C_D$ )

To compute the drag coefficient ( $C_D$ ), it is necessary to determine the normal force coefficient ( $c_N$ ) and the axial force coefficient ( $C_A$ ), and then transform these coefficients into their projection along the direction of motion.

#### 1. Calculation of the Normal Force coefficient ( $C_N$ )

The normal force coefficient represents the component perpendicular to the incoming flow direction. It is calculated using a combination of slender-body theory and empirical contributions<sup>[70] [72]</sup>.

$$(C_N)_{\text{Total}} = (C_N)_{\text{Wing-Body-Tail}} \approx (C_N)_{\text{Body}} + (C_N)_{\text{Wing}} + (C_N)_{\text{Tail}} \quad (\text{D.21})$$

- Body contribution:

$$C_N = \frac{A_b}{A_r} \sin 2\alpha \cos \frac{\alpha}{2} \left( \frac{C_N}{C_{N_0}} \right)_{SB} + \eta \cdot C_{d_n} \frac{A_p}{A_r} \sin^2 \alpha \left( \frac{C_N}{C_{N_0}} \right)_{\text{Newt}} \quad (\text{D.22})$$

Where  $(\frac{C_N}{C_{N_0}})$  are experimental ratios,  $C_{d_n}$  is the crossflow drag coefficient of circular cylinder section (Figure D.2), and  $\eta$  is the crossflow drag proportionality factor.

$$\left( \frac{C_N}{C_{N_0}} \right)_{SB} = \frac{a}{b} \cos^2 \phi + \frac{b}{a} \sin^2 \phi \quad (\text{D.23})$$

$$\left( \frac{C_N}{C_{N_0}} \right)_{\text{Newt}} = \frac{3}{2} \sqrt{\frac{a}{b}} \left\{ \frac{-b^2/a^2}{(1 - (b^2/a^2)^{3/2})} \log \left[ \frac{a}{b} \left( 1 + \sqrt{1 - \frac{b^2}{a^2}} \right) \right] + \frac{1}{1 - (b^2/a^2)} \right\} \quad (\text{D.24})$$

$$\begin{cases} \eta = 0,05 \left( \frac{l}{d} \right) + 0,52 & \text{if } M_a \leq 1 \\ \eta = 1 & \text{if } M_a > 1 \end{cases} \quad (\text{D.25})$$

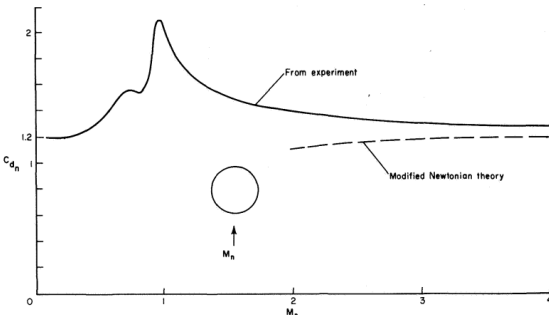


Figure D.2: Crossflow drag coefficient of cylindrical section estimation

- Wing and Tail contribution:

$$\begin{cases} |(C_N)_{\text{Surface}}| = \left[ 4 |\sin \alpha' \cos \alpha'| / (M_a^2 - 1)^{1/2} + 2 \sin^2 \alpha' \right] (S_{\text{Surface}} / S_{\text{Ref}}) & \text{if } M_a^2 > 1 + [\frac{8}{\pi A}]^2 \\ |(C_N)_{\text{Surface}}| = [(\pi A/2) |\sin \alpha' \cos \alpha'| + 2 \sin^2 \alpha'] (S_{\text{Surface}} / S_{\text{Ref}}) & \text{if } M_a^2 \leq 1 + [\frac{8}{\pi A}]^2 \end{cases} \quad (\text{D.26})$$

## 2. Calculation of the Axial Force Coefficient ( $C_A$ )

The axial force coefficient represents the component parallel to the incoming flow direction. It is obtained by summing the contributions of Wave Drag, Skin Friction, and Base Drag:

$$C_A = C_{A_W} + C_{A_{SF}} + C_{A_B} \quad (\text{D.27})$$

- Body Wave contribution(tangent ogive nose):

$$\begin{cases} C_{A_W} = 0, 8 \sin^2(\beta) & \text{if } M \leq 1 \\ C_{aw} = P \left\{ 1 - \frac{[196 f_n^2 - 16]}{14(M+18)f_n^2} \right\} & \text{if } M > 1 \end{cases} \quad (\text{D.28})$$

Where:

$$\begin{aligned} P &= \left( 0.083 + \frac{0.096}{M_a^2} \right) \left( \frac{\sigma}{10} \right)^{1.69} \\ \sigma &= 2 \tan^{-1} \left[ \frac{d/2}{l} \right] \left( \frac{180}{\pi} \right) \end{aligned} \quad (\text{D.29})$$

- Skin Friction contribution:

The skin friction contribution is computed the Van Driest method<sup>[74]</sup>, by solving:

$$\frac{0, 242 (\sin^{-1} C_1 + \sin^{-1} C_2)}{A (C_{f_\infty})^{1/2} \left( \frac{T_w}{T_\infty} \right)^{1/2}} = \log_{10} (\text{Re}_\infty C_{f_\infty}) - \left( \frac{1+2n}{2} \right) \log_{10} \left( \frac{T_w}{T_\infty} \right) \quad (\text{D.30})$$

Where:

$$C_1 = \frac{2A^2 - B}{(B^2 + 4A^2)^{1/2}} \quad C_2 = \frac{B}{(B^2 + 4A^2)^{1/2}} \quad (\text{D.31})$$

$$A = \left[ \frac{(\gamma - 1)M_a^2}{2 \frac{T_w}{T_\infty}} \right]^{1/2} \quad B = \frac{1 + (\gamma - 1)/2M_a^2}{\frac{T_w}{T_\infty}} - 1 \quad (\text{D.32})$$

- Base pressure contribution:

$$\begin{cases} C_{A_B} = -\frac{2}{\gamma M_a^2} \left\{ \left( \frac{2}{\gamma+1} \right)^{1.4} \left( \frac{1}{M_a} \right)^{2.8} \left[ \frac{2\gamma M_a^2 - (\gamma-1)}{\gamma+1} \right] - 1 \right\} & \text{if } M_a \geq 1 \\ C_{A_B} = 0.12 + 0.13M_a^2 & \text{if } M_a < 1 \end{cases} \quad (\text{D.33})$$

The total aerodynamic drag coefficient ( $C_D$ ) is obtained as the projection of  $C_N$  and  $C_A$  along the flow direction:

$$C_D = C_A \cos(\alpha) + C_N \sin(\alpha) \quad (\text{D.33})$$

## E.1 Thermodynamical model for boiloff analysis

### E.1.1 Ellipsoidal domes and Insulation mass and thickness

In order to estimate the external surface area of the oxidizer tank, the tanks have been modeled as a central cylindrical core, with ellipsoidal domes. The domes' main shape parameter is the Aspect ratio  $AR = r/h$ , the ratio between the radius of the tank and the height of the domed section; this value has been set to  $\sqrt{2}$  since it is the typical one assumed<sup>[1]</sup>.

The equations governing the shape of the domes are:

$$V_{domes} = \frac{4}{3}\pi r^3 \frac{1}{AR}$$

$$e_{domes} = \sqrt{1 - 1/AR^2}$$

$$S_{domes} = \pi r^2 \left(1 + \frac{\operatorname{atanh}(e_{domes})}{AR^2 e_{domes}}\right)$$

Starting from the total oxidizer mass, through density, the volume is computed. Then, for a fixed  $AR$  and  $r$ , the volume of the domes is computed, and the volume of the central cylinder is the remaining.

As now the characterization of the volumes (and dimensions) is done, external surface is easily computed, and mass follows through the relation  $m_{ins} = 1.123S_{LOX} = 36.3 \text{ kg}$ <sup>[30]</sup>.

Volume computations are repeated for a new radius  $R = r + th$ , where  $th$  is the thickness of the insulation, until  $th$  is determined as the value outputting the correct insulation volume.

### E.1.2 Thermal resistances model

#### E.1.2.1 LOX-Tank Convection

In order to size the convection coefficient  $h$  between the LOX and the tank, assumption of natural convection is made. Thus, the steps in determining  $h$  are:

$$Gr = \frac{g\beta\Delta TL^3}{\nu^2} = \frac{9.81 \cdot 9.53 \times 10^{-3} \cdot 0.2 \cdot 0.6^3}{(1.72 \times 10^{-7})^2} = 1.365 \cdot 10^{11}$$

$$Pr = \frac{\mu c_p}{k} = \frac{19.644 \times 10^{-6} \cdot 1696.8}{0.15142} = 2.2$$

$$Ra = Gr \cdot Pr = 3 \times 10^{11}$$

$$Nu = 0.36 Ra^{1/3} = 2411$$

$$h = \frac{Nu \cdot k}{L} = \frac{2411 \cdot 0.15142}{0.6} = 608.5 \frac{W}{m^2 K}$$

All thermophysical data are taken from the NIST database, characteristic length is the tank radius, the  $\Delta T$  is hypothesized and validated afterwards. Formulas are from literature<sup>[101]</sup>.

#### E.1.2.2 Insulation-Air Convection

In order to size the convection coefficient  $h$  between the external side of the insulation and the surrounding air, assumption of forced convection is made. Thus, the steps in determining  $h$  are:

$$Re = \frac{\rho MaL}{\mu} = \frac{0.38 \cdot 299 \cdot 0.85 \cdot 19}{14.69 \times 10^{-6}} = 1.25 \times 10^8$$

$$Pr = \frac{\mu c_p}{k} = \frac{14.69 \times 10^{-6} \cdot 1005}{0.022} = 0.67$$

$$Nu = 0.037 Re^{4/5} Pr^{1/3} = 27217$$

$$h = \frac{Nu \cdot k}{L} = \frac{27217 \cdot 0.022}{19} = 112.6 W/m^2 K$$

The aircraft is assumed at 11km, at  $M = 0.85$ , air data are taken from the *U.S. Standard Atmosphere 1976*<sup>[102]</sup>. Formulas are from literature<sup>[101]</sup>.

## F.1 Figures of Merit for the selection of Fuel species

In order to select the best fuel species, an analysis on the three main types of fuel was performed: RP-1, Hydrogen and Methane. The Figures of Merit (FoM) were chosen as Specific impulse, Storability, Availability and Occupance. These values are then normalized with respect to the biggest value.

In order to size the specific impulse, average values between vacuum and sea level were taken from literature<sup>[1]</sup>.

FUEL	RP1	LH2	LCH4
$I_s$ [s]	326.5	421	348
FoM [%]	77.6	100	82.66

Storability was evaluated as the normalized difference between storage and ambient temperature. Data are taken from NIST<sup>[103]</sup>, as the boiling temperature of cryogenic species and ambient temperature for RP1.

FUEL	RP1	LH2	LCH4
$T_{stored}$ [K]	293	20	112
FoM [%]	100	6.8	38.2

Availability was evaluated as a figure of merit representing how easy an engine can be bought or built: a working and available engine gets 2.5 points, an available engine to be necessarily modified gets 1 point, a non-already available engine gets 0.5 points. RP1 got 10 points (Newton 3, Rutherford, Reaver, Chiron engines), LH2 got 1 point(RL-10 engine), LCH4 got 2.5 points (Aeon1 engine)

FUEL	RP1	LH2	LCH4
Availability	10	1	2.5
FoM [%]	100	10	25

Occupance was evaluated by directly analyzing fuel densities, with data taken from NIST<sup>[103]</sup>.

FUEL	RP1	LH2	LCH4
$\rho$ [kg/m <sup>3</sup> ]	806	71	424
FoM [%]	100	8.8	52.6

Cumulatively, FoMs are combined using a weighted average (values chosen according to priorities of the team).

FUEL	$I_s$	Storability	Availability	Occupance	Total
Weight	0.3	0.2	0.4	0.1	1
RP1	77.6	100	100	100	93.3
LH2	100	6.8	10	8.8	36.2
LCH4	82.66	38.2	25	52.6	47.7

# Appendix G

## Bibliography

- [1] Don Edberg and Willie Costa, *Design of Rockets and Space Launch Vehicles*. AIAA, 2022.
- [2] EoPortal, “Rocket lab satellite missions.” [Online]. Available: <https://www.eoportal.org/other-space-activities/rocket-lab#stp-27rd>
- [3] W. C. . Alexander and R. A. Lau, *STATE-OF-THE-ART STUDY FOR HIGH-SPEED DECELERATION AND STABILIZATION DEVICES*. Goodyear Aerospace Corporation, 1966. [Online]. Available: <https://ntrs.nasa.gov/api/citations/19660027566/downloads/19660027566.pdf>
- [4] T. W. Knacke, “Parachute recovery systems design manual,” 1991.
- [5] W. C. P. Jack N. Nielsen, George E. Kaattarti, “Lift and centre of pressure of wing-body-tail combinations at subsonic, transonic and supersonic speeds,” NASA, Tech. Rep. NASA-SP-8007, 1959. [Online]. Available: <https://ntrs.nasa.gov/api/citations/19930091008>
- [6] Wiley J. Larson and James R. Wertz, *Space mission Analysis and Design*. Springer Dordrecht, 1992.
- [7] V. L. Pisacane, *Fundamentals of Space Systems*, 2nd ed. Oxford University Press, 2005.
- [8] Pasquale M. Sforza, *Manned Spacecraft Design Principle*. Elsevier, 2015.
- [9] RocketLab, “Electron payload user guide.” [Online]. Available: <https://www.rocketlabusa.com/assets/Uploads/Rocket-Lab-Launch-Payload-Users-Guide-7.0.pdf>
- [10] Northrop Grumman, “Pegasus user guide.” [Online]. Available: <https://www.northropgrumman.com/space/pegasus-rocket>
- [11] VirginOrbit, “Launcherone service guide.” [Online]. Available: <https://newspaceconomy.ca/wp-content/uploads/2022/06/launcherone-service-guide-august-2020.pdf>
- [12] Aevum Space, “Aevum rolls out ravn x the world’s first autonomous launch vehicle and the largest unmanned aircraft system (uas).” [Online]. Available: <https://www.aevumspace.com/newsroom/aevum-rolls-out-ravnx>
- [13] C. G. Niederstrasser, “The small launch vehicle survey a 2021 update (the rockets are flying),” Elsevier, 2021.
- [14] EO Portal, “Zero 2 infinity.” [Online]. Available: <https://www.eoportal.org/satellite-missions/zero-2-infinity>
- [15] Josè M. Lopez-Urdiales, Guillaume Girard, and Izan Peris-Marti, “Bloostar, the enabler for more efficient satellites in low earth orbit,” AIAA, 2018.
- [16] D.Henry, “Boeing 767 vs 747 — key variances in size, capacity, range,” *skycomparison*, 2024. [Online]. Available: <https://skycomparison.com/boeing-767-vs-747/>
- [17] A. Commerce, “Aircraft owner’s & operator’s guide: 747-200/-300.” [Online]. Available: [https://www.aircraft-commerce.com/sample\\_article\\_folder/owners\\_guide.pdf](https://www.aircraft-commerce.com/sample_article_folder/owners_guide.pdf)

- [18] “1979 boeing 747-200sf for sale.” [Online]. Available: <https://www.globalplanesearch.com/aircraft/3964805-1979-boeing-747-200sf-for-sale-for-sale-in>
- [19] Curtis, Howard D., *Orbital Mechanics for Engineering Students*, 3rd ed. Oxford: Butterworth-Heinemann, 2014.
- [20] N. Sarigul-Klijn and M. Sarigul-Klijn, “A comparative analysis of methods for air-launching vehicles from earth to sub-orbit or orbit,” *Proceedings of the Institution of Mechanical Engineers, Part G: Journal of Aerospace Engineering*, vol. 220, no. 5, pp. 439–452, 2006. [Online]. Available: <https://doi.org/10.1243/09544100JAERO46>
- [21] M. Sarigul-Klijn and N. Sarigul-Klijn, “A study of air launch methods for rlvs.” [Online]. Available: <https://arc.aiaa.org/doi/abs/10.2514/6.2001-4619>
- [22] Ahmed Adel Mohamed Abdel-Raheem, Poula Awad Suleiman Hanna, Islam Atef Mohamed Abdel-Hameed, “Aerodynamic study of boeing 747-400 airfoil.” [Online]. Available: [https://www.researchgate.net/publication/334826189\\_Aerodynamic\\_Study\\_of\\_Boeing\\_747-400\\_Airfoil](https://www.researchgate.net/publication/334826189_Aerodynamic_Study_of_Boeing_747-400_Airfoil)
- [23] A. D. Koch, “Optimal staging of serially staged rockets with velocity losses and fairing separation,” *Aerospace Science and Technology*, 2019.
- [24] ESA-ESTEC, “Ecss-e-st-32-10c rev.1,” ESA, Tech. Rep., 2009.
- [25] A. De Paulis, P. Forte, F. Frendo, E. Manfredi, *Costruzione di Macchine - Criteri di base e applicazioni principali*. Pearson, 2019.
- [26] J. J. Z. C. T. Modlin, “The 1.5 & 1.4 ultimate factors of safety for aircraft & spacecraft - history, definition and applications,” NASA, Tech. Rep., 2014.
- [27] RocketLab, “Rocket lab reaches 500 rutherford engine test fires.” [Online]. Available: <https://www.rocketlabusa.com/updates/rocket-lab-reaches-500-rutherford-engine-test-fires/>
- [28] ARIANE-V fairing separation altitude. [Online]. Available: [https://www.esa.int/Enabling\\_Support/Space\\_Transportation/Launch\\_vehicles/Ariane\\_5\\_fairing](https://www.esa.int/Enabling_Support/Space_Transportation/Launch_vehicles/Ariane_5_fairing)
- [29] Rocket Payload Fairings – What They Are And How They Work. [Online]. Available: <https://headedforspace.com/rocket-payload-fairings/>
- [30] D. Akin, “Mass estimating relations.” [Online]. Available: <https://spacecraft.ssl.umd.edu/academics/791S16/791S16L08.MERsx.pdf>
- [31] J. R.R.Rohrschneider, “A comparison of modern and historic mass estimation relationships on a two-stage to orbit launch vehicle,” AIAA, Tech. Rep., 2001.
- [32] “Mitsubishi electric, geared motors,” <https://www.mitsubishielectric.com/fa/download/search.page?mode=catalog&kisyu=/gear> and <https://www.mitsubishielectric.com/app/fa/download/search.do?mode=catalog&kisyu=/servo>.
- [33] Keith Nisbet, Richard G. Budynas, *Shigley's Mechanical Engineering Design*. McGraw-Hill, 2015.
- [34] Y. Liu, “Concept and key technology analysis of electric pump-fed liquid propellant rocket engine,” *IOP Conference Series: Earth and Environmental Science*, 2021.
- [35] O. B. George P. Sutton, *Rocket Propulsion Elements*. Wiley, 2016.
- [36] J. V.I.Weingarten, P.Seide, “Buckling of thin-walled circular cylinders,” NASA, Tech. Rep. NASA-SP-8007, 1968. [Online]. Available: <https://ntrs.nasa.gov/citations/19690013955>

- [37] M. W. Hilburger, "Buckling of thin-walled circular cylinders," NASA, Tech. Rep. NASA-SP-8007-2020-REV2, 2020. [Online]. Available: <https://ntrs.nasa.gov/citations/20205011530>
- [38] V. P. Seide, "Buckling of thin-walled truncated cones," NASA, Tech. Rep. NASA-SP-8019, 1968. [Online]. Available: <https://ntrs.nasa.gov/citations/19690014753>
- [39] NASA, "Materials data handbook, aluminum alloy 2219." [Online]. Available: <https://ntrs.nasa.gov/api/citations/19720022811/downloads/19720022811.pdf>
- [40] J.D. Jackson, W.K. Boyd, P.D. Miller, "Reactivity of metals with liquid and gaseous oxygen," DTIC, 1963.
- [41] Hongfei Zheng, Xuesen Zeng, Jinbao Zhang, Hongjie Sun, "The application of carbon fiber composites in cryotank." [Online]. Available: [https://www.researchgate.net/publication/323777311\\_The\\_Application\\_of\\_Carbon\\_Fiber\\_Composites\\_in\\_Cryotank/download?tp=eyJjb250ZXh0Ijp7ImZpcnN0UGFnZSI6InB1YmxpY2F0aW9uIiwicGFnZSI6Il9kaXJIY3QifX0](https://www.researchgate.net/publication/323777311_The_Application_of_Carbon_Fiber_Composites_in_Cryotank/download?tp=eyJjb250ZXh0Ijp7ImZpcnN0UGFnZSI6InB1YmxpY2F0aW9uIiwicGFnZSI6Il9kaXJIY3QifX0)
- [42] W. A. Wagner, R. B. Keller, "Liquid rocket metal tanks and tank components," 1974.
- [43] B. Szelinski, H. Lange, C. Röttger, H. Sacher, S. Weiland, D. Zell, "Development of an innovative sandwich common bulkhead for cryogenic upper stage propellant tank." [Online]. Available: <https://www.sciencedirect.com/science/article/abs/pii/S0094576512002639>
- [44] NASA, "Materials, process and manufacturing in ares i - upper stage: Integration with system design and development." [Online]. Available: <https://ntrs.nasa.gov/api/citations/20080037300/downloads/20080037300.pdf>
- [45] MatWeb: Aluminum 2219 mechanical properties. [Online]. Available: <https://www.matweb.com/search/DataSheet.aspx?MatGUID=86215ca4233a49fdb6b556235fc726b7>
- [46] MatWeb: Carbon Fiber/Epoxy composites mechanical properties. [Online]. Available: [https://www.matweb.com/search/datasheet\\_print.aspx?matguid=39e40851fc164b6c9bda29d798bf3726](https://www.matweb.com/search/datasheet_print.aspx?matguid=39e40851fc164b6c9bda29d798bf3726)
- [47] Miandi Group: Aluminum 2219 data sheet. [Online]. Available: <https://www.aviaetaluminum.com/it/2219-aviation-grade-aluminium-high-temperature-resistance-various-temp.html>
- [48] Aircraft Materials: Aluminum 2219 data sheet. [Online]. Available: <https://www.aircraftmaterials.com/data/aluminium/2219.html>
- [49] Performance Composites: Carbon Fiber/Epoxy minimum thickness. [Online]. Available: <https://www.performancecomposites.com/about-composites-technical-info/124-designing-with-carbon-fiber.html>
- [50] A. D., "747 flight test certification." [Online]. Available: <https://www.sae.org/publications/technical-papers/content/700828/>
- [51] Adolfo Zavelani Rossi, Giuseppe Cocchetti, *Meccanica delle Strutture*. Progetto Leonardo, 2009.
- [52] ESA, "European cooperation for space standardization, structural design." [Online]. Available: [https://ecss.nl/item/?glossary\\_id=384](https://ecss.nl/item/?glossary_id=384)
- [53] Boeing, "747-400 airplane characteristics for airport planning." [Online]. Available: [https://www.boeing.com/content/dam/boeing/boeingdotcom/commercial/airports/acaps/747-400\\_REV\\_E.pdf](https://www.boeing.com/content/dam/boeing/boeingdotcom/commercial/airports/acaps/747-400_REV_E.pdf)

- [54] J. Barnes, “The pros and cons of liquid rocket engines.” [Online]. Available: <https://skysift.com/the-pros-and-cons-of-liquid-rocket-engines/>
- [55] V. Pakalapati, “Overall analysis of hydrogen, kerosene and methane in lre technology,” Master’s thesis, Politecnico di Milano, 2021.
- [56] D. H. et al., “Green propellant propulsion concepts for space transportation and technology development needs,” *ESA special publications*, 2004.
- [57] P. E. Schabedoth, “Life cycle assessment of rocket launches and the effects of the propellant choice on their environmental performance,” Master’s thesis, Norwegian University of Science and Technology, 2020.
- [58] D. L. Pablo Rachov, Hernán Tacca, “Electric feed systems for liquid propellant rocket engines,” 2010.
- [59] T. Dodd, “Everyday astronaut: Previous launches.” [Online]. Available: <https://everydayastronaut.com/previous-launches/>
- [60] M. Sheetz, “Virgin orbit shuts down after bankruptcy sales.” [Online]. Available: <https://www.cnbc.com/2023/05/23/virgin-orbit-bankruptcy-sale-rocket-lab-stratolaunch-vasts-launcher.html>
- [61] S. Clark, “Chris kemp unplugged—astra’s ceo dishes on the space company’s struggles.” [Online]. Available: <https://fireflyspace.com/wp-content/uploads/2024/10/Alpha-PUG-5.0.pdf>
- [62] F. Aerospace, “Firefly alpha: Payload users’s guide.” [Online]. Available: <https://fireflyspace.com/wp-content/uploads/2024/10/Alpha-PUG-5.0.pdf>
- [63] ASTRA, “Rocket 4 payload user’s guide.” [Online]. Available: <https://astra.com/wp-content/uploads/2022/11/Rocket-4-Payload-Users-Guide-v1.1-November-22.pdf>
- [64] A. V. Krivonogov, “Method of calculating the thickness of the combustion chamber of a liquid rocket engine made with the use of innovative technologies and materials,” Master’s thesis, VESTNIK of Samara University Aerospace and Mechanical Engineering, 2017.
- [65] R. R. Society, “Making correct parabolic nozzles.” [Online]. Available: <https://www.rrs.org/2023/01/28/making-correct-parabolic-nozzles/>
- [66] N. I. of Standards and Technology, “Oxygen.” [Online]. Available: <https://webbook.nist.gov/cgi/cbook.cgi?ID=C7782447>
- [67] NASA, “External tank thermal protection system.” [Online]. Available: [https://www.nasa.gov/wp-content/uploads/2016/08/114022main\\_tps\\_fs.pdf](https://www.nasa.gov/wp-content/uploads/2016/08/114022main_tps_fs.pdf)
- [68] N. W. Service, “Vandenberg space force base.” [Online]. Available: <https://www.weather.gov/wrh/timeseries?site=KVBG>
- [69] T. L. Pad, “Virgin orbit launcherone launch.” [Online]. Available: <https://www.youtube.com/watch?v=JV1pCKvd-Bg>
- [70] L. H. Jorgensen, “A method for estimating static aerodynamic characteristics for slender bodies of circular and noncircular cross section alone and with lifting surfaces at angles of attack from 0 to 90”, NASA, Tech. Rep. NASA TN 0-7228, 1973. [Online]. Available: <https://ntrs.nasa.gov/citations/19730012271>

- [71] A. Y. A. John R. Spreiter, "Slender-body theory based on approximate solution of the transonic flow equation," NASA, Tech. Rep. NASA-TR-R-2, 1959. [Online]. Available: <https://ntrs.nasa.gov/citations/19980227201>
- [72] L. H. Jorgensen, "Prediction of static aerodynamic characteristics for space-shuttle-like and other bodies at angles of attack from 0 ° to 180 °," NASA, Tech. Rep. NASA TN D-6996, 1973. [Online]. Available: <https://ntrs.nasa.gov/citations/19730006261>
- [73] B. J. Short, "Newtonian aerodynamics for circular cones modified to produce lift at zero angle of attack," NASA, Tech. Rep. NASA-TN-D-5193, 1969.
- [74] E. J. Hopkins, "Charts for predicting turbulent skin friction from the van dries method (11)," NASA, Tech. Rep. NASA TN D-6945, 1972. [Online]. Available: <https://ntrs.nasa.gov/citations/19730001588>
- [75] E. S. Love, "The base pressure at supersonic speeds on two-dimensional airfoils and bodies of revolution (with and without fins) having turbulent boundary layers," NACA, Tech. Rep. NACA-RM-L53C02, 1953. [Online]. Available: <https://ntrs.nasa.gov/citations/20030064135>
- [76] B. C. E. Rogers and D. Cooper, "Rogers aeroscience rasaero aerodynamic analysis and flight simulation software." [Online]. Available: <https://www.rasaero.com/>
- [77] "Openrocket simulator." [Online]. Available: <https://openrocket.info/>
- [78] S. L. Filippo Maggi, "Lecture notes of launch systems," 2024.
- [79] "Matlab." [Online]. Available: <https://it.mathworks.com/products/matlab.html>
- [80] Frans Von Der Dunk, Frans Tronchetti, "Handbook of Space Law," 2015.
- [81] S. X, "Falcon 9." [Online]. Available: <https://www.spacex.com/vehicles/falcon-9/>
- [82] V. S. F. Base, "Vandenberg supports successful pegasus launch." [Online]. Available: <https://www.vandenberg.spaceforce.mil/News/Article-Display/Article/2656558/vandenberg-supports-successful-pegasus-launch/>
- [83] F. Biertümpfel, S. Bennani, and H. Pfifer, "Time-varying robustness analysis of launch vehicles under thrust perturbations," *Advanced Control for Applications*, vol. 3, no. 4, 2021. [Online]. Available: <https://onlinelibrary.wiley.com/doi/abs/10.1002/adc2.93>
- [84] A. Karabeyoglu, "Advanced rocket propulsion: Rocket testing," *Department of Aeronautics and Astronautics at Stanford University and Mechanical Engineering at KOC University*, 2019. [Online]. Available: [https://web.stanford.edu/~cantwell/AA284A\\_Course\\_Material/Karabeyoglu%20AA%20284A%20Lectures/AA284a\\_Lecture16.pdf](https://web.stanford.edu/~cantwell/AA284A_Course_Material/Karabeyoglu%20AA%20284A%20Lectures/AA284a_Lecture16.pdf)
- [85] M. Darley and P. Beck, "Return to sender: Lessons learned from rocket lab's first recovery mission." [Online]. Available: <https://digitalcommons.usu.edu/cgi/viewcontent.cgi?article=5031&context=smallsat>
- [86] F. Nebiker, *Development of a BALLUTE Recovery System for Mach 10 Flight and Its Practical Applications*. Goodyear Aerospace Corporation, 1964. [Online]. Available: <https://books.google.it/books?id=kZAdHQAAQAAJ>
- [87] J. W. Usry, *PERFORMANCE OF A TOWED, 48-INCH-DIAMETER*. NASA, 1969. [Online]. Available: <https://ntrs.nasa.gov/api/citations/19690008066/downloads/19690008066.pdf>
- [88] E. G. Ewing, *Ringsail Parachute Design*. Air Force Flight Dynamics Laboratory, Ohio, 1972.

- [89] C. Dek and Others, "A recovery system for the key components of the first stage of a heavy launch vehicle." [Online]. Available: <https://www.sciencedirect.com/science/article/pii/S1270963819326458>
- [90] D. J. Dalle and S. C. Spangelo, "Preliminary design of small satellites for atmospheric reentry." [Online]. Available: [https://icubesat.org/wp-content/uploads/2012/06/icubesat-org-2012-b-1-4-paper\\_dalle\\_201205251148.pdf](https://icubesat.org/wp-content/uploads/2012/06/icubesat-org-2012-b-1-4-paper_dalle_201205251148.pdf)
- [91] "Rocket lab to take next major step toward electron reusability by launching pre-flown engine." [Online]. Available: <https://www.rocketlabusa.com/updates/rocket-lab-to-take-next-major-step-toward-electron-reusability-by-launching-pre-flown-engine/>
- [92] ESA, "Mitigating space debris generation." [Online]. Available: [https://www.esa.int/Space\\_Safety/Space\\_Debris/Mitigating\\_space\\_debris\\_generation](https://www.esa.int/Space_Safety/Space_Debris/Mitigating_space_debris_generation)
- [93] NASA, "State-of-the-art of small spacecraft technology: Deorbit systems." [Online]. Available: <https://www.nasa.gov/smallsat-institute/sst-soa/deorbit-systems/>
- [94] P. J. A. Nodir Adilov and B. Cunningham, "An analysis of launch cost reductions for low earth orbit satellites." [Online]. Available: [https://www.researchgate.net/publication/379335390\\_An\\_Analysis\\_of\\_Launch\\_Cost\\_Reductions\\_for\\_Low\\_Earth\\_Orbit\\_Satellites\\_accepted\\_for\\_publication\\_Economics\\_Bulletin\\_2022](https://www.researchgate.net/publication/379335390_An_Analysis_of_Launch_Cost_Reductions_for_Low_Earth_Orbit_Satellites_accepted_for_publication_Economics_Bulletin_2022)
- [95] T. Erbas, "Money pits in rocket production." [Online]. Available: <https://timucin1erbas.medium.com/money-pits-in-rocket-production-patent-article-i-9e7317d009a>
- [96] C. S. Transportation, "Update of the space and launch insurance industry." [Online]. Available: [https://www.faa.gov/about/office\\_org/headquarters\\_offices/ast/media/sr\\_98\\_4q.pdf](https://www.faa.gov/about/office_org/headquarters_offices/ast/media/sr_98_4q.pdf)
- [97] O. W. in Data, "Cost of space launches to low earth orbit." [Online]. Available: <https://ourworldindata.org/grapher/cost-space-launches-low-earth-orbit>
- [98] RocketLab, "Electron." [Online]. Available: <https://www.rocketlabusa.com/launch/electron/>
- [99] Ross, Sheldon M., *Probabilità e Statistica per l'Ingegneria e le Scienze*. Apogeo, 2018.
- [100] The MathWorks, Inc., *MATLAB fzero Function Documentation*. [Online]. Available: <https://www.mathworks.com/help/matlab/ref/fzero.html>
- [101] Incropera, F.P., DeWitt, D.P., Bergman, T.L., Lavine, A.S., *Fundamentals of Heat and Mass Transfer*. Wiley, 2007.
- [102] T. E. toolbox, "U.S. standard atmosphere vs. altitude." [Online]. Available: [https://www.engineeringtoolbox.com/standard-atmosphere-d\\_604.html](https://www.engineeringtoolbox.com/standard-atmosphere-d_604.html)
- [103] N. I. of Standards and Technology, "Nist website." [Online]. Available: <https://www.nist.gov>